Thermally Sprayed Coatings as Resistive Heating Systems for Wind Turbine Blades and Airfoils

by

Shahed Taghian Dehaghani

A thesis submitted in partial fulfillment of the requirements for the degree of

Doctor of Philosophy

Department of Mechanical Engineering

University of Alberta

Abstract

Accumulation of ice on the surface of wind turbine blades and aircraft wings in cold environments causes serious issues such as decrease in performance and efficiency. Ice accretion alters the geometrical profile and aerodynamic performance of the surface and increases the weight of the original structure. Furthermore, in some cases, icing may cause casualties and produce other significant safety issues. These undesired and detrimental effects, necessitates further development of novel de-icing systems.

In this doctoral research program, the main objective is to develop thermally sprayed coatings to serve as de-icing elements for wind turbine blades and aircraft wings. Thus far, this research has focused on studying the effect of reinforcing ceramic particles on the heating performance of Ni-based resistive heating coatings and their erosion resistance. Nickel-chromium-aluminum-yttrium (NiCrAlY) powder was chosen as the matrix and was mechanically blended with three different ceramic powders namely, alumina, titania, and tungsten carbide, to produce feedstock powders for fabrication of metal matrix composite (MMC) coatings. A number of Joule heating tests were conducted by creating voltage differences across the coatings to enable electron flow and measuring the surface temperature of the heating elements. The effect of electrical resistance and dielectric behavior of the ceramic particles on the performance of the heating elements was investigated. These tests were conducted in an air duct under free and forced convection. It was observed that the ramp-up rate and the steady-state temperature were considerably affected by the electrical properties of the MMC coatings. A two-dimensional transient heat conduction model is being developed in order to predict the temperature distribution during the heating process.

The surface of these coating-based heating systems were exposed to surface degradation involving solid particle and water droplet impact erosion. For this reason, two types of erosion tests were conducted in order to study the effect of ceramic reinforcement on the wear resistance of the de-icing elements. For the water droplet impact experiments, samples were placed inside a high-speed wind tunnel with an approximate droplet impact speed of 60 m/s. Solid particle impact tests were performed using a low-pressure cold spraying unit for impingement of erodent particles. The data demonstrated considerably lower wear rate in NiCrAlY-WC-12Co and NiCrAlY-titania compared to other coatings. The results suggest that MMC coatings could be effectively used to increase the erosion resistance of coating-based heating systems.

Real-time variation of the coatings electrical resistance and temperature during the material removal stage of the dry erosion experiments demonstrated the effect of ceramic reinforcement phase on overall functionality of the coatings. The heating elements were also subjected to a series of icing/de-icing tests in a closed-loop icing wind tunnel. MMC elements with higher electrical resistivity exhibited considerably better performance in terms of the required de-icing time and the total consumed energy.

Preface

A few of the sections presented in this thesis document have been or will be published in peer reviewed journal revues or conference proceedings as follows:

- Sections 1.1, 1.2, 1.3 and the entire Chapter 2 of this thesis document with the exception of Sections 2.1.2, 2.1.3, 2.3.1, 2.3.2 has been published in a peer reviewed journal as shown below:

  Shahed Taghian Dehaghani, Ali Dolatabadi, André McDonald, "**Thermally sprayed metal matrix composite coatings as heating systems**", Applied Thermal Engineering, Vol. 196, pp. 117321, 2021

- The entire Chapter three with the exception of Sections 3.1.5 and 3.2.4 has been published in the proceedings of the ITSC conference as shown below:

  Shahed Taghian Dehaghani, Ali Dolatabadi, André McDonald, "**Effect of Ceramic Particle Reinforcement on the Erosion Resistance of Thermally Sprayed De-icing Systems**", ITSC 2021—Proceedings of the International Thermal Spray Conference, Quebec City, Canada, May 24–27, 2021.

- Sections 2.1.2, 2.1.3, 2.3.1, and 2.3.2 of this thesis documents has been published in the proceedings of the ITSC conference as shown below:

Shahed Taghian Dehaghani, Ali Dolatabadi, André McDonald, "**An experimental study of the performance of flame-sprayed Ni-based metal matrix composite coatings as resistive heating elements**", ITSC 2019—Proceedings of the International Thermal Spray Conference, Yokohama, Japan, May 26–29, 2019.

All the authors contributed to the preparation of the listed papers. I conducted the research work under the guidance of Dr. André McDonald and Dr. Ali Dolatabadi in their roles as research supervisors.

Acknowledgments

First and foremost, I wish to express my sincerest gratitude to my supervisors, Prof. A. McDonald and Prof. A. Dolatabadi for their guidance, continuous support and excellent supervision throughout the course of my doctoral program. Completion of this research program would have been impossible without their support, hard work, and encouragement. I would like to thank the member of my doctoral supervisory committee, Prof. M. Sadrzadeh for his time, valuable advice, and suggestions. I am also thankful to the members of the examining committee, Prof. M. Flynn and Prof. S. Joshi for their valuable time.

I would like to thank technical support from the machine shop technicians. I am also very thankful to Mr. R. Conrad for his invaluable advice and guidance regarding electrical assembly of the heating system. I am also very grateful to Mr. M. Malik, Mr. A. Amer, and Mr. E. Farahani for assisting me with my experiments.

Last, but certainly not the least, I would like to thank my parents, Mr. A. Taghian Dehaghani and Ms. Z. Mahdavi, and my dear sister, Ms. S. Taghian Dehaghani, for their encouragement and support for my studies towards graduate degree and all accomplishments that I have made.

Table of Contents

Table of Contents

List of Tables

List of Figures

Chapter 1

Introduction

1.1 Background

1.1.1 Ice Accumulation on Airfoils and its Detrimental Effects

Icing is one of the most important issues concerning aerospace and energy generation industries. Ice accretion on the surface of certain machines, devices, and tools, may cause several significant problems that undermine functionality, efficiency, and safety. In particular, accumulation of ice on the surface of wind turbine blades and aircraft wings compromises aerodynamic efficiency and alter surface profile of airfoils. Moreover, ice accretion could result in casualties and major safety risks. As a result, devising a novel and effective de-icing or anti-icing system is undoubtedly needed to tackle the undesirable consequences of icing. Higher air density in colder environments significantly increases the potential power output of wind turbines. However, wind turbines operating in low-temperature climates should be sufficiently equipped in order to mitigate the detrimental effects that are typical of cold environment operations [1].

Over the last three decades, a number of studies have been conducted to mitigate ice accretion on the surface of wind turbine blades and airfoils [2-5]. Jasinski *et al*. [6] studied the decline in performance of wind turbines due to icing. The experiments were performed on a S809 wind turbine airfoil under various icing conditions, and demonstrated significant decrease in power generation caused by icing. Cao *et al*. [7] investigated the effects of icing on the aviation safety of aircrafts by analyzing the effect of ice accumulation on stability,

controllability, and aerodynamic performance. Lamraoui *et al*. [8] studied a wide range of issues caused by ice accretion on wind turbine blades, focusing on degradation of generated power. A number of similar experimental and numerical studies have been conducted on the effect of icing on the degradation of aerodynamic performance of airfoils [9-11]. Relatively higher air density in colder regions results in increased amount of generated power by wind turbines. As a result, despite the detrimental consequences of icing, many wind farms are installed in low-temperature areas [1]. Various methods and approaches have been implemented in recent decades to combat ice accretion. Parent and Ilinca [1] described a number of active and passive anti-icing techniques for wind turbines such as use of ice-phobic coatings, paints, air layer, microwave and resistive heaters. In their study, the advantages and disadvantages of the methods were compared in terms of reliability, efficacy, and durability.

Passive de-icing systems are based on altering certain properties of the surface, while active de-icing systems mainly utilize external devices and equipment such as a power source [1, 12]. Use of hydrophobic materials as a method for icing mitigation is one of the most significant approaches in passive de-icing systems [13, 14]. Farhadi *et al*. [15] studied the ice-repellency of various nano-structured superhydrophobic coatings. The results of their study showed that variation in surface asperities during icing/de-icing cycles had an adverse impact on the de-icing performance of the superhydrophobic coatings. Similar observations were made in another study conducted by Lazauskas *et al*. [16] on anti-icing performance of superhydrophobic SiO_2 nanocomposites. A study conducted by De Pauw and Dolatabadi [17] evaluated the de-icing performance of a superhydrophobic coating deposited on an aluminum NACA 0012 airfoil. The results of this study showed a 50% decrease in power consumption for de-icing. Gomaa *et al*. [18] performed various water droplet impact experiments on superhydrophobic surfaces for a

wide range of droplet sizes by implementing a drop on-demand micro-dispensing technique. It was observed that the droplet size had a noticeable effect on different aspects of droplet impact dynamics.

There are three major categories of active de-icing techniques, namely, thermal, mechanical, and chemical [19]. Using warm air circulation inside the airfoil structure is one of the most common techniques to mitigate ice growth [20, 21]. This method functions well in relatively milder climates and for temperatures close to 0 °C. However, for lower temperatures, the efficacy of this type of de-icing system is considerably reduced [22]. Thermal de-icing techniques using electrical heating elements are more effective compared to other methods [19, 22]. These heating elements are either laminated into the blade surface, or embedded inside the airfoil structure [19]. An investigation into embedded heating elements in polymer composite airfoils was conducted by Mohseni and Amirfazli [13]. In their study, a numerical heat transfer model and thermal analysis was conducted in order to predict the power threshold which results in thermal degradation of the airfoils. Figure 1-1 shows the severity of ice accumulation on wind turbine blades.

Aircraft and wind turbine icing has been vastly studied over the last few decades. Lynch and Khodadoust [3] conducted a comprehensive review and investigation on various in-flight icing categories and the consequent decline in operational control. Melody *et al.* [4] developed an ice detection algorithm in order to enhance the icing simulations for in-flight conditions. Battisti [5] investigated three different aspects of wind turbine icing, namely, cost effectiveness, design parameters and safety-related issues. Various de-icing techniques were studied in order to expand the operational temperature range and minimize the long shutdown periods. Supercooled

large droplet (SLD) icing is among the most common categories of ice accretion. A study conducted by Cao *et al*. [7] addressed SLD icing caused by freezing rain and its relative safety risk increase compared to regular water droplet icing.

De Pauw and Dolatabadi [17] investigated the de-icing capability of a superhydrophobic coating deposited on a 2-d small-scale NACA 0012 airfoil. Their experiments showed that the hydrophobic coating had a promising de-icing performance for temperatures above -10 ℃. A superhydrophobic duplex coating system, developed by Brown *et al.* [23], consisted of a thick TiO_2 layer deposited by suspension plasma spraying and a thin layer fabricated by plasma enhanced chemical vapor deposition. The proposed system demonstrated a promising performance during after exposure to 170 icing/de-icing cycles.

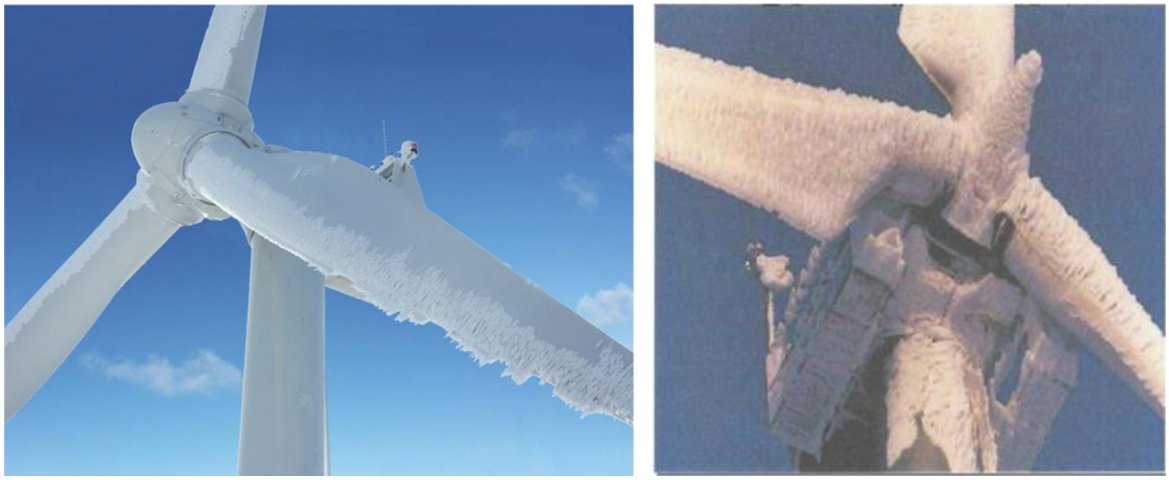

Figure 1-1 Ice accretion on the surface of wind turbine blades [22]

1.2 Coating-based Resistive Heating Systems

As reported by Petrenko *et al*. [19], the de-icing methods functioning based on electrical resistive heating demonstrated considerably higher efficacy. Indirect heating of the blade surface

could lead to significant heat loss due to thermal resistance between the surface and the electrical heating element. Coating-based heating systems are designed and developed to increase efficacy by heating the surface directly without any intermediary layer. Based on Joule heating (also referred to as resistive or Ohmic heating), heat is generated in an electrical resistor when electrical current is passed through it [24, 25]. Several studies have been conducted on coating heating elements outlining different aspects of this type of heating [26-28]. Lamarre *et al*. [27] investigated various thermal and mechanical properties of iron-based flame-sprayed heating elements. A number of experiments in addition to a finite element analysis were conducted in order to assess and predict crack formation in the resistive heaters.

Lopera-Valle and McDonald [29] used flame spraying technique to fabricate a coating-based heating element on the surface of fiber-reinforced polymer composite (FRPC) plates. Their experiments showed that the applied heating system had high efficacy under harsh conditions such as sub-zero temperatures with forced convection. by using flame-sprayed nickel-chromium-aluminum-yttrium (hereafter referred to as NiCrAlY) coatings as heating elements. NiCrAlY coatings are selected as the metal matrix for their high durability, and corrosion resistance. Several tests were conducted under forced convection conditions for different sub-zero ambient temperatures. It was found that a coating thickness of approximately 100 μm was effective for de-icing purposes. The results of this study clearly showed that the proposed heating system is capable of effective icing mitigation in temperatures as low as -25 °C. A phase change finite length-scale mathematical model was also developed which predicted the solid-liquid interface velocity during melting with high accuracy.

1.3 Thermally Sprayed Metal Matrix Composite Heating Elements

A group of materials, namely, metal matrix composites (here after referred to as MMCs) has been widely utilized in many industrial applications due to their promising properties. A number of studies have primarily focused on the application of MMCs in thermal management [30, 31]. In the electronics industry, the excessive generated heat in different components of a device necessitates the application of materials with thermo-mechanical properties within a specific range. For this reason, metal matrix composites could be effectively implemented in order to fabricate materials serving as heat sinks with certain values of thermal conductivity and coefficient of thermal expansion [32]. In recent years, thermally sprayed MMC coatings have been increasingly used owing to their desirable mechanical properties such as wear resistance and hardness [33, 34]. Several investigators have shown that the integration of particulate reinforcement into metal matrix coatings results in higher coating hardness [34, 35], improved toughness and strength [35, 37], and reduced wear rates [36-38]. Missing from this body of research, however, are studies that explore the novelty of MMC coatings as next-generation heating elements.

Multi-layered MMC coatings that are developed for heating applications in conductive substrates are composite media. Transient heat transfer analysis in a composite medium has many applications in engineering [39]. One-dimensional heat conduction modelling of multi-layered slabs has been studied extensively [39-41]. A study on one-dimensional modelling of single splat thermal-sprayed layers on substrate surface has even been conducted [42]. Antonopoulos and Tzivanidis [41] presented a method of solution based on separation of variables and orthogonal expansion technique which solved transient one-dimensional non-homogeneous heat conduction problems for multi-layered slabs. A similar study was conducted

by Monte [40] which predicted the transient response of one-dimensional composites to sudden temperature variation of the surrounding fluid.

The Green's function approach for solution of one-dimensional composites with time-dependent non-homogeneities has been extensively explained by Hahn and Özişik [39]. Salt [43] introduced a two-dimensional composite model, with perfect thermal contact between the layers without internal energy generation. Aviles-Ramos *et al*. [44] proposed an inverse heat conduction technique for a composite body consisted of one orthotropic and one isotropic layer. In their study, the Dirac delta function was multiplied by the heat flux at the boundary and the product was considered as an internal heat source. However, the analytical approach in solution of transient two-dimensional heat conduction within a composite slab with energy generation has not been investigated in detail.

Thermal spraying is one of the most significant methods of coating fabrication which has been widely used in different sectors of industry. Through this process, melted or half melted particles of metals or ceramics are propelled towards a surface with high-velocity. Upon cooling down, these particles adhere to the surface and form a coating. Depending on the specific industrial need, various thermal spraying techniques could be implemented [45]. The most prominent thermal spraying methods are Flame spraying, Atmospheric Plasma Spraying (APS), High-Velocity Oxy Fuel (HVOF), and Suspension Plasma Spray (SPS). Figure 1-2 shows a schematic of the thermal spraying process.

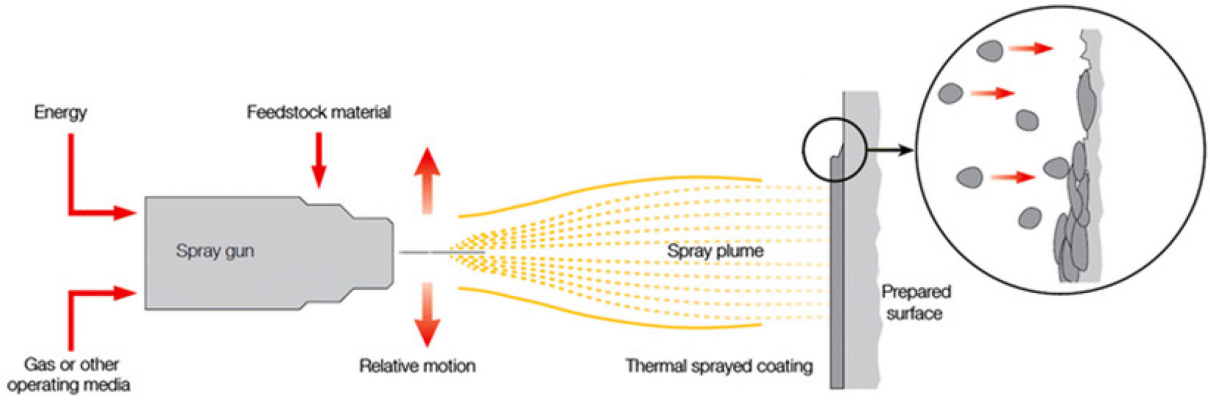

Figure 1-2 Schematic of the thermal spraying process [45]

Deposition of electrically conductive coatings onto metal substrates can lead to short-circuiting in resistive heating applications. This has been resolved by positioning a dielectric layer between the substrate and the coating-based heating element. The efficacy of alumina as a dielectric material has been well established in many studies [27, 46-48]. Rezvani Rad *et al*. [48] compared the dielectric capability of alumina layers deposited using different thermal spraying techniques. It was shown that the required thickness of the alumina layer deposited with flame spraying was higher than that of suspension plasma spraying. Pawlowski [49] conducted several experiments on plasma sprayed alumina powders with varying particle size distributions in order to examine their dielectric properties. The results clearly showed that the dependency of dielectric properties on coating thickness decreased when coarser powders were used.

Utilizing resistive heating metal coatings deposited directly onto electrically conductive substrates may lead to short-circuiting of the heating element. In these cases, placing a dielectric layer between the resistive heating coatings and the conductive substrates has been shown to be an effective solution to the problem of short-circuiting [26, 27, 46]. Extensive research studies

have been conducted on the dielectric properties of alumina [46, 47]. Rezvani-Rad and McDonald [50] successfully used a layer of flame-sprayed alumina as electrical insulation of nickel-chromium (Ni-50Cr) coating heating elements on carbon steel pipes. This multi-layered coating system also included two layers of ring-shaped cold-sprayed copper at the opposite ends of the pipe to function as electrical terminals for Joule heating. Figure 1-3 shows the schematic of a metallic FeCrAlY heating element being insulated by a layer of alumina deposited by APS [27].

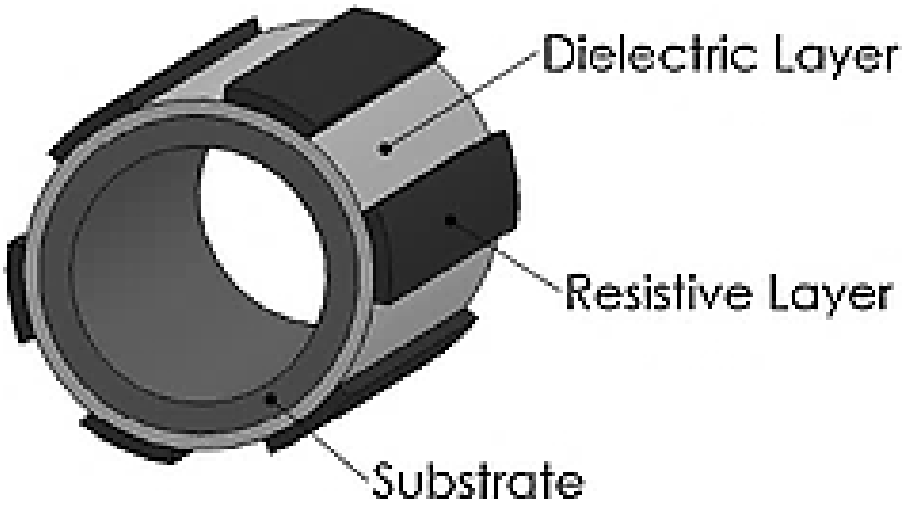

Figure 1-3 Schematic of the ceramic insulating layer on a metal substrate [27]

1.4 Erosion of The Coating-based Heating elements

The leading edge of aircraft wings and wind turbine blades is susceptible to different types of erosive wear among which water droplet and solid particle impact are the most important. The erosion at the leading edge of wind turbine blades caused by impingement of water droplets results in decreased power output and compromises aerodynamic efficiency [51, 52]. Keegan *et al*. [53] conducted a review addressing different mechanisms of airfoil leading

edge erosion focusing on water droplet and hailstone impact. Zhang *et al*. [54] tested two specific types of protective coatings for wind turbine blades for use against water droplet erosion. It was shown that the droplet impact frequency and water jet velocity are the two key parameters affecting erosion rate.

Wind can carry sand particles detached from the ground and move them towards the surface of airfoils. The impingement of these solid particles upon the surface causes surface deterioration and acts as if the surface is being sand blasted [55]. Shipway and Hutchins [56] conducted a comprehensive review on utilizing solid particle impact in assessing the durability of coatings. Kulu *et al*. [57] studied the erosive wear behavior of various thermally sprayed coatings. It was found that the erosion rate was considerably higher for elevated temperatures. A dry erosion testing apparatus was developed by Ashrafizadeh *et al*. [58] based on the ASTM G76 [59] standard on solid particle impingement experiments. Using a cold gas dynamic spray system, garnet sand particles were blasted upon polyurethane elastomer substrates and their wear rate was compared at different temperatures. Various studies have addressed the undesirable consequences of ice accretion, water droplet and solid particle impact erosion. However, no practical solutions have been presented in order to solve or mitigate the corresponding problems simultaneously.

1.4.1. Water Droplet Impact Erosion

Impingement of high-speed water droplet on solid surfaces could lead to surface degradation and is referred to as Water Droplet Erosion (WDE). In WDE, the targeted surface is affected by hydrodynamic forces resulting from the momentum of micron-sized water droplets [60]. In order to reduce the detrimental effects of WDE, a number of methods have been

introduced such as use of thermally sprayed coatings or specific surface treatment methodologies [61, 62]. It has been established that coatings with a ductile metallic phase and a hard ceramic phase (such as MMCs) have a promising performance in combatting WDE [62, 63]. Especially, use of tungsten carbide cermets such as WC-Co is very much effective in this application [62, 64]. The cobalt phase would serve as a ductile binder and contributes to the coating toughness, while the tungsten carbide enhances the hardness.

WDE erosion consists of four significant damage modes namely, plastic deformation and formation of cracks and asperities, stress wave propagation, lateral outflow jetting and hydraulic penetration [60, 65]. Upon the impact of water droplets on the surface, the applied pressure and consequent stress would lead to formation of shock waves propagating through the material. As a result of this sudden shock, pre-existing asperities would grow and new micro-cracks may be initiated [60, 65]. While there is observable material removal at the two first phases as a result of cracks merging together, the crack development mainly occurs within the last two modes of WDE [60, 66]. Mahdipoor *et al*. [67] used a rotating rig developed for WDE experiments which could provide high-speed droplet impingement to simulate harsh conditions. A schematic of this rotating test rig is shown in Fig. 1-4. Water droplets are propelled through a nozzle and the testing specimen are placed on a rotating disk. As the rotating rig could reach the angular speed of 20,000 rpm and droplet impact speed up to 500 m/s. In these tests, total mass removal curves were plotted against the total erosion exposure. Finally, The effect of mechanical properties and microstructure of WC-Co coatings on the WDE performance of the coatings was investigated.

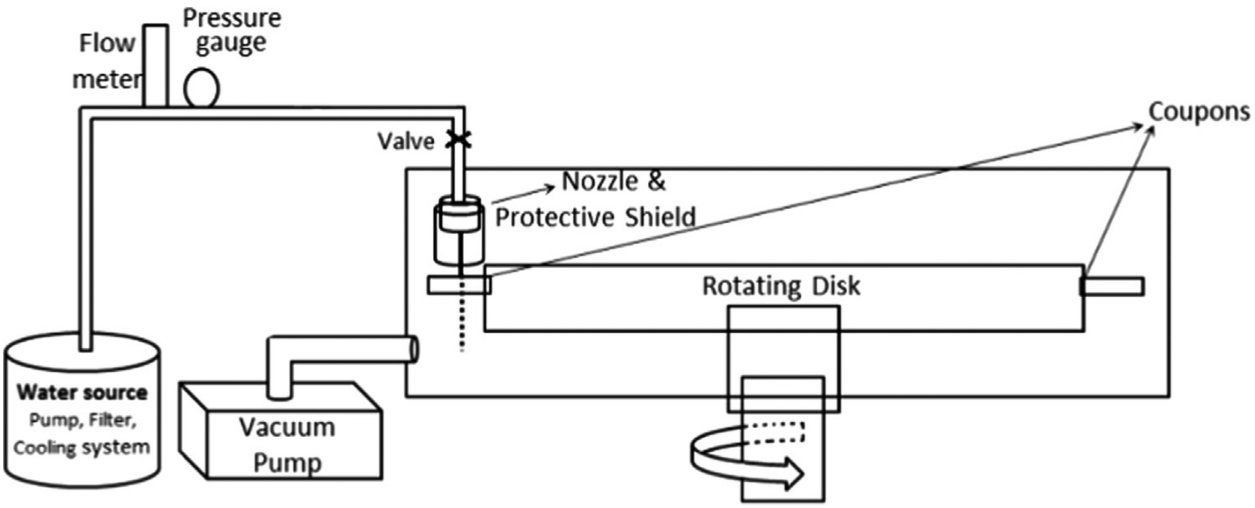

Figure 1-4 Schematic of the rotating WDE test rig [67]

1.4.2 Solid Particle Impact Erosion

Surface degradation and material removal resulted by impingement of hard high-speed particles is referred to as solid particle erosion. Hardness of the erodent particles, impact velocity, cyclic impact load, and pre-existing asperities are among the determining factors affecting the extent of erosion [57]. Figure 1-5 gives a general comparison of erosive wear resistance of different materials and their dependency on hardness, toughness, and the percentage of the hard ceramic phase. The standard ASTM G76 [59] standard provides guidelines for performing solid particle impact erosion testing. Ashrafizadeh et al. [58] proposed a modified version of the ASTM G76 by using a low-pressure cold spray system for propelling and accelerating the particles towards the surface. The samples (polyurethane elastomers) were mounted on a test rig and a heater along with a temperature controller was also installed in order to examine the variation of the erosive wear rate with temperature. Figure 1-6 shows both the schematic and the actual image of the testing apparatus [58].

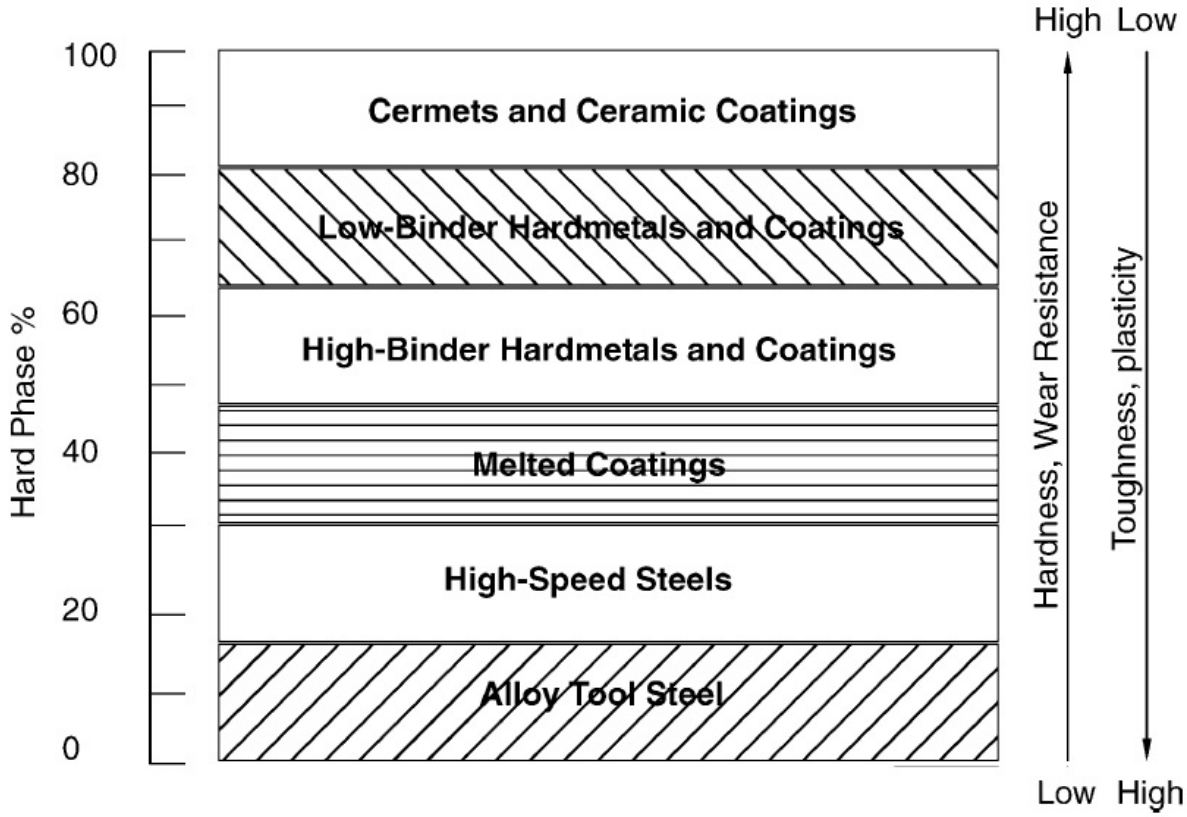

Figure 1-5 Wear resistance of various material groups [57]

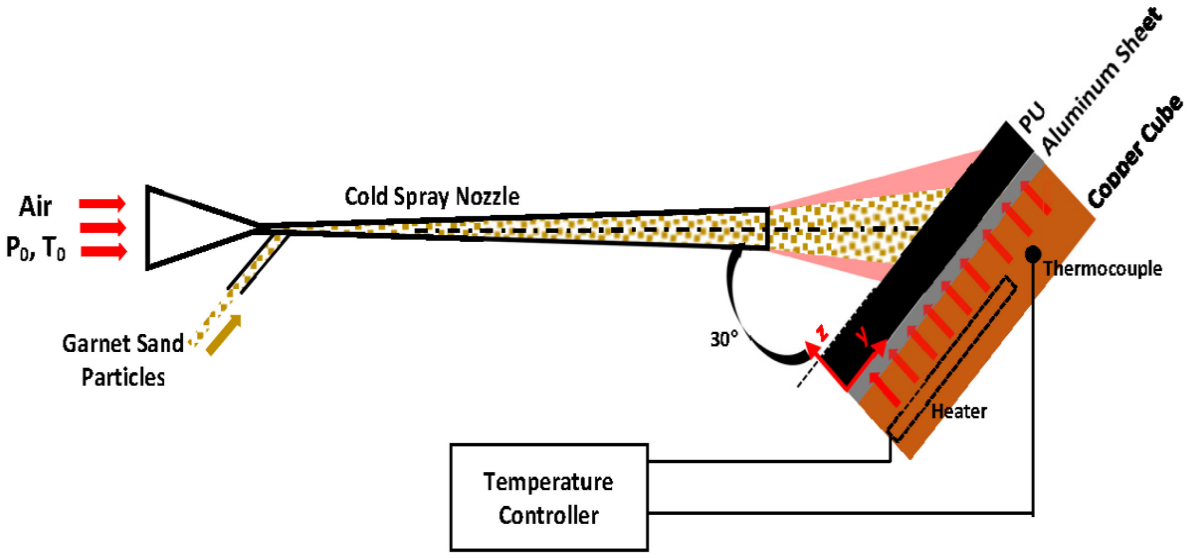

(a)

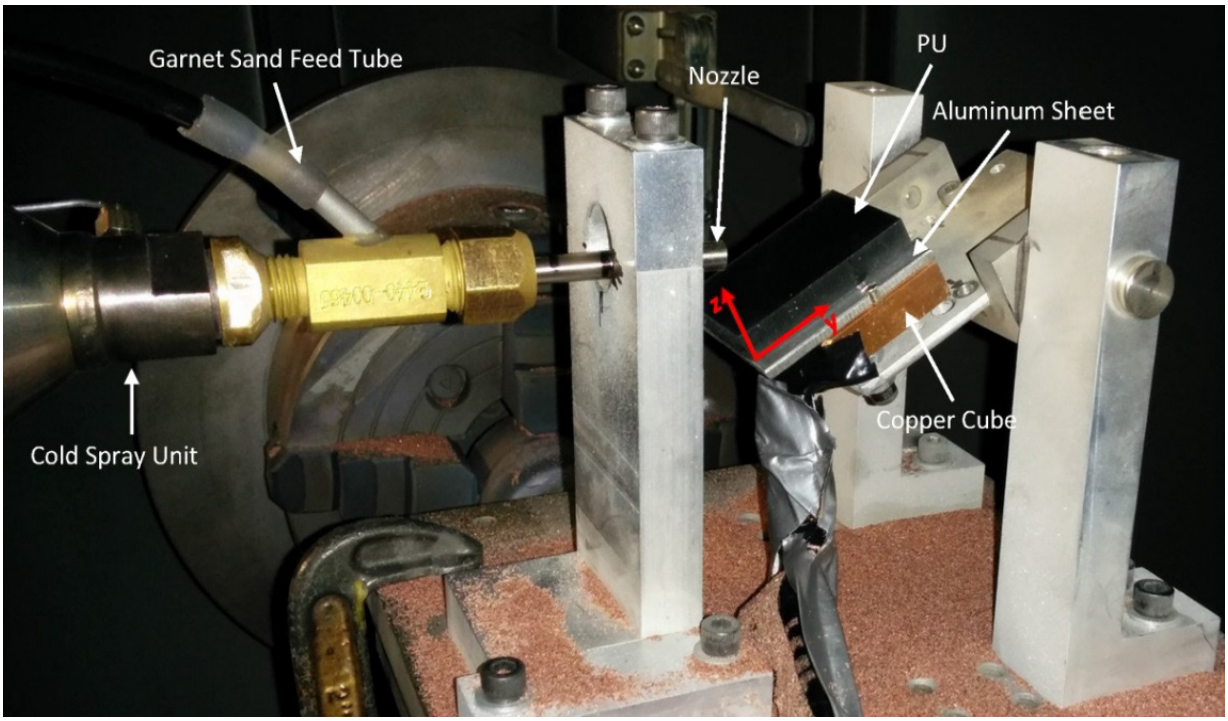

(b)

Figure 1-6 a) Schematic of the testing and b) Image of the actual testing apparatus [58]

1.5 Application of Thermally Sprayed Coatings as De-icing Systems

One of the significant issues concerning the renewable energy generation and aerospace industries is ice accumulation on airfoil surfaces. This would cause serious operational issues especially during the cold seasons. However, it is already established that in terms of efficiency it would be beneficial to build wind farms in colder region due to the higher air density. The other suitable sites for building wind farm would be locations with high altitude owing to the higher air velocity. Generally, wind velocity would increase by 0.1 m/s for every 100 m. These advantages necessitates devising of novel next-generation de-icing systems in order to combat the undesired effects of icing [1]. Nonetheless, there are critical issues that must be addressed

and studied. The most important of these drawbacks are 1) Measurement errors, 2) Power losses, 3) Overproduction 4) Mechanical failures, 5) Electrical failures, and 6) Safety hazard [1].

Accumulation of ice on the different measurement devices installed on wind turbines or aircrafts could cause significant errors. Temperature sensors, anemometers, and wind vanes are the main compromised devices. The effect of icing on the surface shape and roughness would result in appreciable power losses. The intensity of icing and the duration of it are the key determining factors in estimation of power loss which could reach up to 50% of the total annual energy generation [1]. In terms of mechanical properties and physical strength, icing on the airfoils would increase loading on the blades, high-altitude vibration, and causes mass imbalance in the blades. As a result, the risk of mechanical blade failure would definitely increase. Detachment of ice from the blades at high velocities introduces serious safety hazard as the pieces of ice could be thrown to a relatively large distance [1]. There are several types of atmospheric icing among which the in-cloud icing is the most significant. In-cloud icing occurs as a result of supercooled water droplets impacting a surface at sub-zero temperatures and immediately freeze upon impact. There three categories of in-cloud icing namely, soft rime, hard rime, and glaze. The adhesion of the hard rime and glaze to the surface are considerably higher than the soft rime icing [1]. LCW is the air liquid water content which plays an important role on the type of icing. In addition to the icing on the wind turbine blades, aircraft icing should also be studied due to the adverse effects of ice accretion. The icing would lead to significant design and operation problem and has been studied since the 1940s.

The traditional method for aircraft icing analysis were devised to estimate where the water droplet impact occurs and at what rate. This type of analysis required a model for

prediction of droplet trajectory in addition to the examination of proportion of the free stream water concentration which is referred to as water catch. The rate of icing is mainly governed by the heat transfer from the surface of the wings. The main heat transfer processes pertaining to aircraft icing are: 1) kinetic heating, 2) convective cooling, 3) evaporative cooling, and 4) latent phase change heat transfer [68].

The de-icing system devised by Lopera-Valle *et al*. [29] used NiCrAlY as the resistive heating layer to be deposited on FRPC substrates. For enhancing the adhesion, garnet sand was applied to the FRPC surface using an epoxy resin. The Scanning Electron Micrscope (SEM) image of the NiCrAlY coating is depicted in Fig 1-7. These samples were placed inside an open-loop airduct and were exposed to forced convection under different sub-zero temperatures.

The dependency of the transient temperature trace on the applied voltage were also investigated. In order to consider the elements as ohmic, voltage was plotted against the current for different temperatures. The results as depicted in Fig 1-8 evidently confirm these coating-based heating elements as ohmic [29]. In order to measure the speed of the water-ice interface, different stages of icing were applied on the element so that a K-type thermocouples could be placed within the ice. Using this method, the average velocity of the water-ice interface could be determined.

The speed of the water-ice interface is significant in explicating the impact of ambient temperature and the overall heat generated by the coating-based element. A novel one-dimensional finite length scale model was developed in order to predict the water-ice interface velocity. The pertaining heat transfer mechanism has two stages: 1) heating and temperature increase, 2) phase change. The experimentally obtained data showed good agreement with the

model predictions. Figure 1-9 shows the melting time of the ice versus temperature as measured by the experiments and calculated by the aforementioned model [29]. This finite length scale model could be improved by considering the FRPC substrate and ice as a multi-layered composite, with the coating as the heat source in between [29].

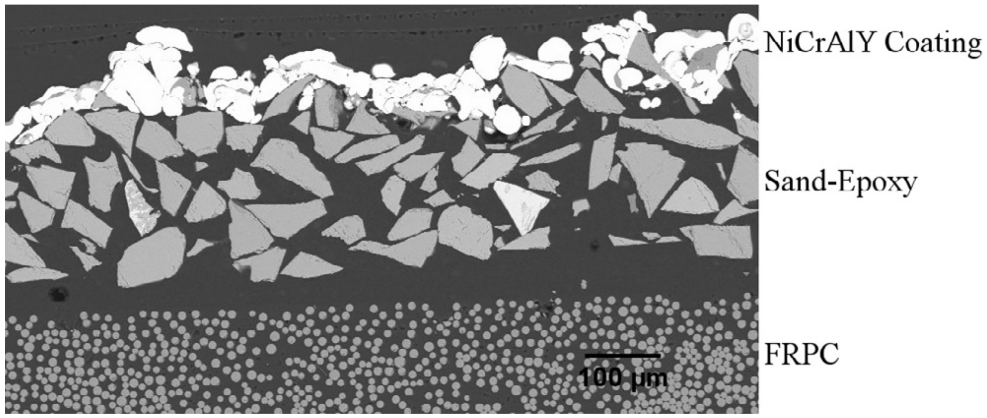

Figure 1-7 SEM micrograph of the resistive heating element [29]

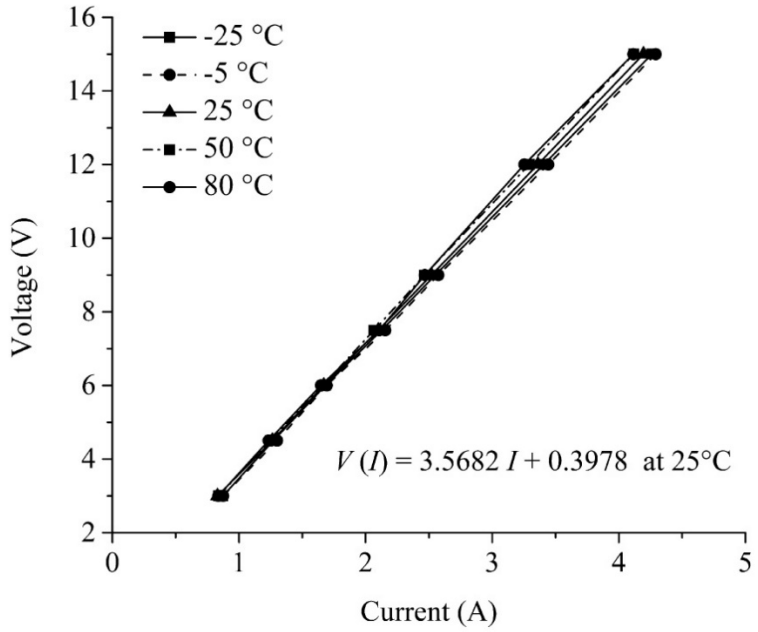

Figure 1-8 Applied voltage versus electric current for different temperatures [29]

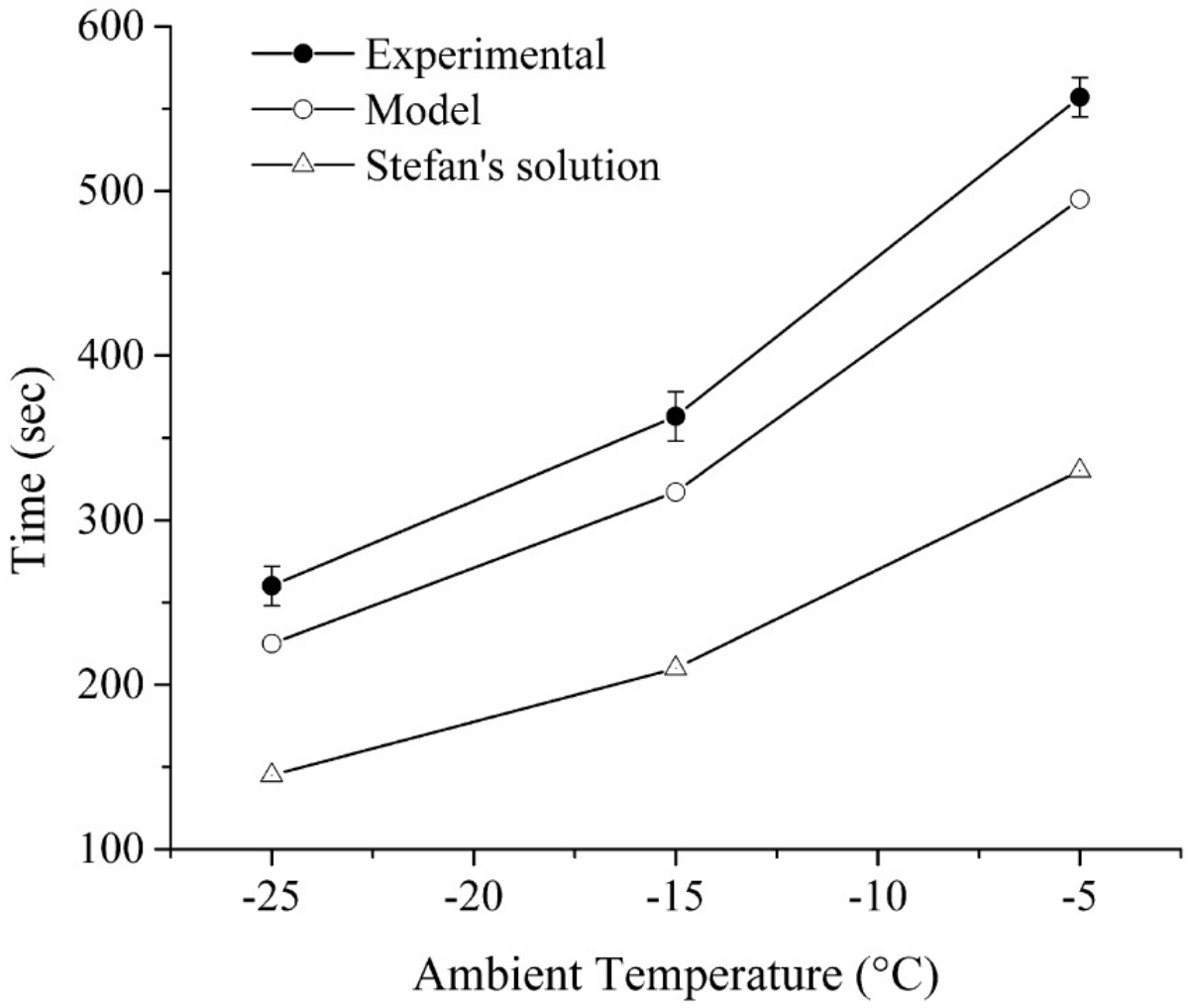

Figure 1-9 Comparison between the experimental data and model results in predicting the melting time of the ice [29]

1.6 Summary

In cold and harsh environments and high altitudes, the risk of ice accretion on the wind turbine blades and aircraft wings is very high. As this issue causes various operational problems, deficiency, overloading, fracture, and safety hazards. This necessitated developing novel de-icing systems to combat this problem. Prior to this research, different approaches to de-icing had been presented and examined. The most prominent of them are blowing the warm bleed air, embedded

electrical heating, implementing hydrophobicity, and coating-based heating element. Several metallic coatings had been previously presented as resistive heating, the most prominent of those are NiCr and MCrAlY coatings. The novelty of this research was to go one step further in order to improve the performance of the coatings as de-icing systems with use of metal matrix composites.

By introducing three distinct ceramics into the mixture of the feedstock, three types of MMC coatings were fabricated namely, NiCrAlY-alumina, NiCrAlY-titania, and NiCrAlY-WC-12Co. The application of this MMC approach was based on two major ideas: 1) Using the reinforcing phase as a means to change the electrical resistivity of the coatings due to specific electrical properties of the reinforcing phases. For instance, the dielectric behavior of Al_2O_3 would make the coating more resistant to the passage of electrons, therefore the electrical resistivity of the coating would increase. This research also examines the effect of different reinforcing phases on the overall heating performance. 2) Improving the wear resistance of the metallic coatings by adding materials with established desired mechanical properties. For instance, adding tungsten carbide (a very hard material) to the metallic mixture would contribute to its wear resistance. Thus, the other novelty of this research is developing wear resistant resistive heating elements which had not been conducted before.

Using a heating system with temperature control and real-time monitoring of the electrical current and temperature, various heating tests were performed under harsh conditions in a cold room. These experiments provide a comparative analysis as to the heating performance of the coatings for different conditions. A series of erosion tests were also conducted for

evaluating the effect of the MMC approach on improving the wear resistance of materials. Again in this case, a comparative study was also made to compare different materials.

A novel type of testing was devised in order to assess the overall performance (wear resistance, heating performance, durability, and functionality) of the coatings under more practical conditions. For the first time, the erosion testing was conducted on the surface of materials while the Joule heating is activated. Using heaters with temperature controllers to heat the eroding surface had been studied before. However, direct impingement of eroding particles on the very coated surface which is heated by Joule heating, had not been studied before.

The last phase of this research was to finally evaluate the actual de-icing capability of the materials by testing them in a closed-loop icing wind tunnel. There is extensive research with regards to ice accretion on solid surfaces inside the wind tunnel. There have also been many studies with regards to de-icing in the wind tunnel by different methods such as indirect heating. However, similar to the previous approaches, the resistive heating was activated while the sample was inside the wind tunnel. Another novelty of this research was studying the melting process of the solidified water droplets on the coatings surfaces, with the resistive coating surface as the heating source.

1.7 Objectives

The objectives of this doctoral research project were to:

i) Develop novel thermally sprayed metal matrix composite de-icing elements.

ii) Contribute to enhanced controllability and heating performance of the de-icing system.

iii) Make a significant increase in the wear resistance of the coating heating elements.

iv) Develop novel heat transfer model for predicting the transient two-dimensional temperature distribution within the multi-layered coatings

v) Evaluate the de-icing performance of the heating elements and making a comparative study for better material and process selection.

1.8 Thesis Organization

The present thesis document has several chapters with the following structure: Chapter 2 focuses on the fabrication of thermally sprayed metal matrix composite heating elements and evaluation of their heating performance. In Chapter 3 of this thesis document, the erosive wear resistance of the developed coating-based heating element were examined by conducting water droplet erosion and solid particle impact erosion testing. Chapter 4 presents a series of experimental results for the de-icing tests conducted in a closed-loop wind tunnel and gives a comparison between the used materials. High-speed imaging was also used to compare the surface energy of the coating surfaces and observing the melting process of droplets upon activation of the heating system. Chapter 5 summarizes the conclusions from this thesis. Finally, Chapter 6 provides the suggestions for future work for extension and modification of this research work.

Chapter 2

Thermally Sprayed Metal Matrix Composite Heating Elements

Accretion of ice on the surface aircraft wings and wind turbine blades is the cause of many undesired outcomes such as decrease in aerodynamic performance, power generation, mechanical failure, and safety hazards. These issues necessitate developing of novel next generation heating elements. This chapter focuses on fabrication of flame sprayed metal matrix composite (MMC) coatings in order to enhance the heating performance of coating-based de-icing systems. Nickel chromium-aluminum-yttrium (NiCrAlY) powder was chosen as the matrix and was mechanically admixed with aluminum oxide, titanium dioxide, and tungsten carbide-cobalt powders in order to deposit MMC coatings on carbon steel substrates. Based on the principle of Joule heating, applying voltage across a resistive coating would result in heating of the surface due to the resistance to the passage of electrons. By conducting several experiments, the heating performance of these fabricated MMC elements is examined in various conditions. The dependency of heating performance on the electrical resistance and microstructure is investigated. In addition, a two-dimensional transient heat transfer model was developed for the multi-layered coating in order to predict the temperature distribution.

The presented work in this chapter has been published in the proceedings of The International Thermal Spray Conference (ITSC), Yokohama, Japan, May 26–29 (2019), p 527-534, and Applied Thermal Engineering, Vol. 196, pp. 117321, 2021.

2.1 Experimental Method

2.1.1 Substrate Preparation and coating deposition- Preliminary tests

Eight identical low-carbon steel (ASTM A36) samples with the dimensions of 127 mm × 25.4 mm with 6.35 mm thickness were prepared for coating deposition. In order to roughen the surface of the samples and improve coating adhesion, they were grit blasted with #24 alumina grit (Manus Abrasive Systems Inc., Edmonton, AB, Canada), operating with compressed air at 722 kPa (90 psig). An oxy-acetylene flame spray torch (6PII, Oerlikon Metco, Westbury, NY, USA) was used to deposit alumina, NiCrAlY, and all the MMC coatings. A volumetric powder feeder (5MPE, Sulzer Metco, Westbury, NY, USA) was employed to deliver the required amount of powder to the torch. In this system, the particles are propelled by argon as the carrier gas.

Due to the high electrical conductivity of the steel substrates, a layer of alumina (AMDRY 6060, Oerlikon Metco, Westbury, NY, USA) was deposited on the substrate prior to deposition of the Ni-based MMC coatings. This layer acts as electrical insulation and prevents short-circuiting of the Ni-based MMC coatings during Joule heating. The size distribution of the alumina powder was -45+5 μm. One pass of preheating was conducted prior to deposition of alumina for all the samples. As reported by Rezvani-Rad and McDonald [50], preheating of the substrate reduced the tensile residual stress that is generated due to solidification of molten droplets.

NiCrAlY powder (AMDRY 964, Oerlikon Metco, Westbury, NY, USA) was used as the metal matrix for producing the MMC coatings. Coatings of pure NiCrAlY were fabricated to serve as controls in evaluating the heating performance of the MMC coatings. Alumina (Al_2O_3,

AMDRY 6060, Oerlikon Metco, Westbury, NY, USA), titania (TiO_2, Metco 102, Oerlikon Metco, Westbury, NY, USA), and tungsten carbide (WC-12Co, Metco 72F-NS, Oerlikon Metco, Westbury, NY, USA) powders were selected as reinforcing ceramic particles for fabrication of the MMC coatings. In order to maintain consistent coating deposition, the torch was operated by a programmable robot (HP-20, Motoman, Yaskawa Electric Corp., Waukegan, IL, USA). Two samples with the same spraying parameters were made for each feedstock powder blend. All the ceramic powders were mechanically admixed with NiCrAlY powder in a 50 wt.%/50 wt.% blend. Table 2-1 lists the spraying parameters that were used for alumina (S1), NiCrAlY (S2), NiCrAlY-Al_2O_3 (S3), NiCrAlY-TiO_2 (S4), and NiCrAlY-WC-12Co (S5).

Table 2-1 Spraying parameters for alumina (S1), NiCrAlY (S2), NiCrAlY-Al_2O_3 (S3), NiCrAlY-TiO_2 (S4), and NiCrAlY-WC-12Co (S5)

Spraying parameters	S1	S2	S3	S4	S5
Stand-off distance [mm]	127	190.5	177.8	177.8	177.8
Torch velocity [mm/s]	300	350	350	350	350
Acetylene flow [NLPM]	22	17	20	20	20
Oxygen flow [NLPM]	32	30	30	30	32
Argon flow rate [m^3/h]	0.56	0.56	0.56	0.56	0.56
Passes	5	4	4	4	4
Powder feed rate (FMR)	100	80	80	80	80
Increment (mm)	3	3	3	3	3

In order to prepare the samples for the Joule heating tests, two vertical strips of copper were cold-sprayed at the opposite ends of each sample. A low pressure cold gas dynamic spray system (SST series P, CenterLine, Ltd., Windsor, ON, Canada) was used to deposit the copper powders (Copper, SST-C5003, CenterLine, Windsor, ON, Canada), which were produced specifically for cold spraying. The size distribution of the copper powder was -45+5 μm. Table 2-2 lists the detailed spraying parameters for the deposition of copper.

Table 2-2 Cold spray parameters for deposition of copper.

Compressed air pressure (kPa)	634
Powder feed rate (%)	5
Compressed air temperature (°C)	400
Stand-off distance (mm)	6
Number of passes	2

2.1.2 Joule Heating Experiments- Preliminary tests

Prior to conducting the Joule heating tests, two electrical wires were directly soldered to the cold-sprayed coatings on the opposite sides of each sample. A heating gun was used in the soldering process in order to enhance the adhesion of the soldering material (tin) to the copper strips and reduce the electrical contact resistance. Figure 2-1 shows the fully prepared samples for the Joule heating experiments. For generating electrical current through the coatings, a DC power supply (1902B DC, B&K Precision Corporation, Yorba Linda, CA, USA) was used. The maximum voltage and electrical current produced by this power supply are 60 V and 15 A,

respectively. The safety mechanism in this power supply measures the resistance between two terminals and controls the voltage in a way that the current falls within the allowable range. In this study, in order to compare the heating performance of the coatings, the maximum possible heat generation was set as the criterion.

Figure 2-1 Fully prepared samples for Joule heating tests

Based on the electrical resistance of each coating, a specific voltage was supplied to the coatings in order to generate the maximum possible power. Selection of the applied voltage values were based on the specifications and limitations of the power supply. In order to reduce the effect of contact resistance, Kelvin connections with four terminals were used to measure the electrical resistance for each sample. All the resistance measurements were conducted by using a digital multimeter (34461A Digital Multimeter, 6 ½ Digit, Keysight Technologies, Mississauga, ON, Canada). All the samples were placed inside an 18 m^3 cold room (Foster Refrigerator USA, Kinderhook, NY, USA). The cold room temperature was maintained at -25 °C for all the tests. A J-type thermocouple (Omega, Montréal, QC, Canada) was used for measuring the ambient temperature during the tests. T-type surface thermocouples (TC50, WIKA Instruments, Edmonton, AB, Canada) were used in order to read the temperature at the middle section of the coating surface.

In order to reduce the measurement error of the T-type surface thermocouple, it was covered with thermal insulation. With the NiCrAlY coating as control, several Joule heating tests were performed under free convection in order to compare the heating performance of the MMCs. In addition, two Joule heating tests under forced convection, with different applied voltages, were conducted on the sample exhibiting the best heating performance. For the experiments under forced convection conditions, the samples were positioned inside a 2 m × 0.66 m × 0.48 m closed duct made of galvanized steel. A 0.25 kW direct-drive axial fan (DDA-12-10033B, Leader Fan Industries, Toronto, ON, Canada) was used to generate air flow for tests performed under forced convection conditions. The air flow velocity was 8.6 m/s.

The temperatures that were measured by the installed thermocouples were collected by a data acquisition system (SCXI-1600, National Instruments, Austin, TX, USA) at a rate of 1 Hz, i.e., one data point per second. A data logger software (NI MAX, National Instruments, Austin, TX, USA) was used to collect and store the temperature measurements. Before conducting each test, the samples were allowed to equilibrate with the environment at -25 °C. In order to improve the experimental design of these tests for a more detailed comparative study, a modified testing system is also introduced in Section 2.1.6. The modified system has significantly more advanced measurement mechanism and temperature control.

2.1.3 Coating characterization- Preliminary tests

In order to observe the microstructure of the coatings, the samples were sectioned and cold-mounted in an epoxy resin (LECO, Mississauga, ON, Canada). The samples were then ground with 180, 240, 320, 400, 600, 800, and 1200 silicon carbide grit papers (LECO, Mississauga, ON, Canada) and polished using 3 μm and 1 μm diamond slurries (LECO, Mississauga, ON, Canada). Due to the presence of ceramic particles in the coatings, which do not conduct electricity well, a thin film of carbon was deposited over all the samples by using a carbon evaporation device (EM SCD 005, Leica Baltec Instrument, Balzers, Liechtenstein). Carbon coating is a necessary step in order to avoid super charging of the non-conductive ceramics.

A scanning electron microscope (Zeiss Sigma 300 VP-FE, Carl Zeiss Canada Ltd., Toronto, ON, Canada) was employed to capture micrograph images of the coatings and to analyze the microstructure of the coatings. In addition, energy-dispersive X-ray spectroscopy (EDS) was used to distinguish the different phases in MMC coatings. Image analysis software

(ImagePro, Media Cybernetics, Bethesda, MD, USA) was used to determine the average thickness, porosity, and volumetric percentage of different phases in the coatings.

2.1.4 Substrate Preparation and Coating Deposition- Modified Testing System

The thermal spray process and the feedstock material used for these tests are identical to that of Sec 2.1.1. However, the mass percentage of the reinforcing ceramics was reduced to 40% and slight changes were applied to the spraying parameters outlined in Table 2-3. The method described in Section 2.1.1 is also applied here to prevent short-circuiting. Substrates were preheated prior to deposition of the alumina layer. Preheating results in a considerable decline in residual tensile stress, which is created because of cooling and solidification of molten particles [48]. For each MMC powder, six samples were deposited using identical spraying parameters. Six samples were also deposited with pure NiCrAlY powder to serve as the control coating. Figure 2-2 shows the distribution of tungsten carbide particles in the NiCrAlY-40 wt. %WC-12Co powder mixture, and morphology of NiCrAlY and NiCrAlY-WC-12Co powders. The weighted percentage of the reinforcing powder were changed from 50% to 40% (compared to preliminary tests) in order to achieve coatings with more uniform microstructure.

Table 2-3 Spray parameters for flame-sprayed NiCrAlY (N1), NiCrAlY-WC-12Co (N2), NiCrAlY-Al_2O_3 (N3), NiCrAlY-TiO_2 (N4).

Parameter	**N1**	**N2**	**N3**	**N4**
Stand-off distance [mm]	177.8	165.1	165.1	165.1
Torch velocity [mm/s]	330	300	300	330
Acetylene flow [NLPM]	19	23	23	21
Oxygen flow [NLPM]	30	32	32	30
Increment [mm]	3	3	3	3

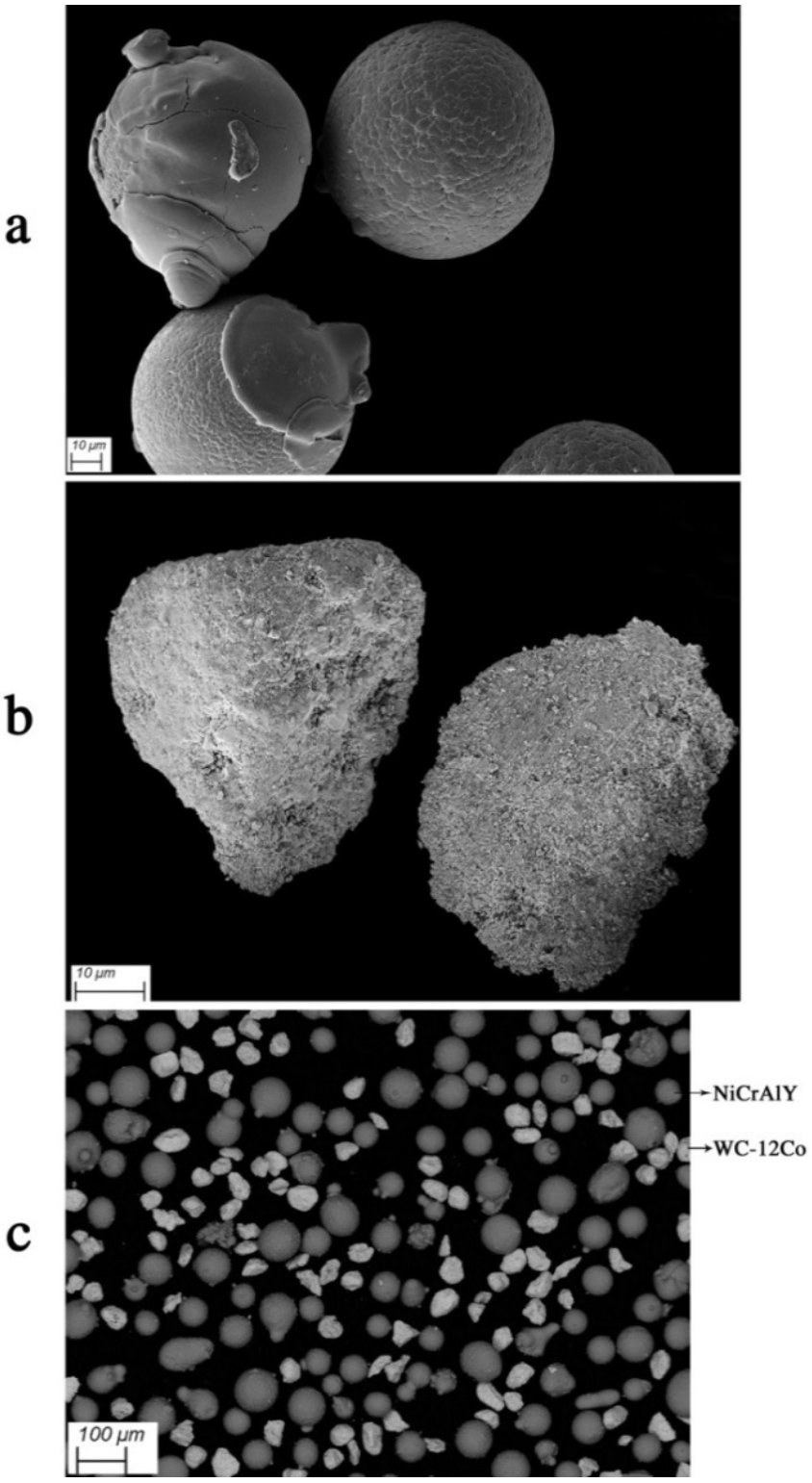

Figure 2-2 Secondary electron image of the a) NiCrAlY powder and b) WC-12Co powder, and c) Backscattered electron microscopy image of the NiCrAlY-WC-12Co MMC powder blend

2.1.5 Coating Characterization- Modified Testing System

The cross-sectional microstructure of the powders and coatings was analyzed using a scanning electron microscope (Zeiss Sigma 300 VP-FE, Carl Zeiss Canada Ltd., Toronto, ON, Canada). In order to prepare the samples for SEM imaging, they were cold-mounted in an epoxy resin and cured for 24 hours. The samples were then ground with silicon carbide grit papers and polished with 3 μm and 1 μm diamond suspensions (LECO, Mississauga, ON, Canada), consecutively. Prior to imaging the coating cross-sections, the samples were carbon coated in order to prevent super-charging of the electrically non-conductive materials. A carbon evaporation device (EM SCD 005, Leica Baltec Instrument, Balzers, Liechtenstein) was used to deposit a thin film of carbon over the samples. Porosity, thickness and volumetric percentage of reinforcing phase materials in the coatings were measured using an image analysis software (ImagePro, Media Cybernetics, Bethesda, MD, USA).

2.1.6 Joule Heating Experiments- Modified Testing System

Electrical wires were soldered to the vertical copper strips located at the opposite sides of the samples to prepare them for Joule heating. In order to improve the adhesion in soldering, a heating gun was used to preheat the cold sprayed copper. This resulted in decreasing the electrical contact resistance between the soldering material (tin) and copper. This methodology for connection of electrical contact was effectively used by Rezvani Rad *et al.* [48] for fabrication of resistive heating elements on carbon steel pipes. In order to generate voltage differences within the heating elements, a DC power supply (1902B DC, B&K Precision Corporation, Yorba Linda, CA, USA) was employed. This power supply could generate maximum electrical voltage of 60 V. In all the tests, a safety mechanism was implemented by

real-time measurement of electrical resistance, ensuring that the electrical current stayed below 15 A. Prior to the tests, the electrical resistance of all the samples were measured employing the four-point Kelvin connection technique using a digital multimeter (34461A Digital Multimeter, 6 ½ Digit, Keysight Technologies, Mississauga, ON, Canada).

In order to conduct a comparative study on the heating performance of the coating-based heating elements, the initially applied voltage was adjusted so that the supplied power to the heating system was identical for different elements. This adjustment was performed based on the initial measurements of the electrical resistance between two terminals of the power supply. A solid state relay (SSRL240DC25, OMEGA, QC, Canada) and a temperature controller (CN7500 ramp/soak controller, OMEGA, QC, Canada) were linked to the power supply as part of a fail-safe mechanism. This safety apparatus was operated based on a specified allowable temperature range and real-time readings of the coating surface temperature. Experiments were conducted inside an 18 m^3 cold room (Foster Refrigerator USA, Kinderhook, NY, USA), which was maintained at -25 °C for all the experiments to examine the heating performance of the coatings under harsh environmental conditions.

Surface temperature measurements were performed by using T-type surface thermocouples (TC50, WIKA, Edmonton, AB, Canada), which were covered by thermal insulation for minimizing the ambient impact on temperature readings. The ambient temperature was measured using a K-type (Omega, Montréal, QC, Canada) thermocouple. As shown in Fig 2-3, the specimens were placed inside a closed duct (2 m × 0.66 m × 0.48 m) on a flat steel bar positioned at the middle section of the duct. Fiber glass was used for covering the steel bar for thermal insulation. A schematic illustration of the Joule heating experiments is shown in Fig 2-4.

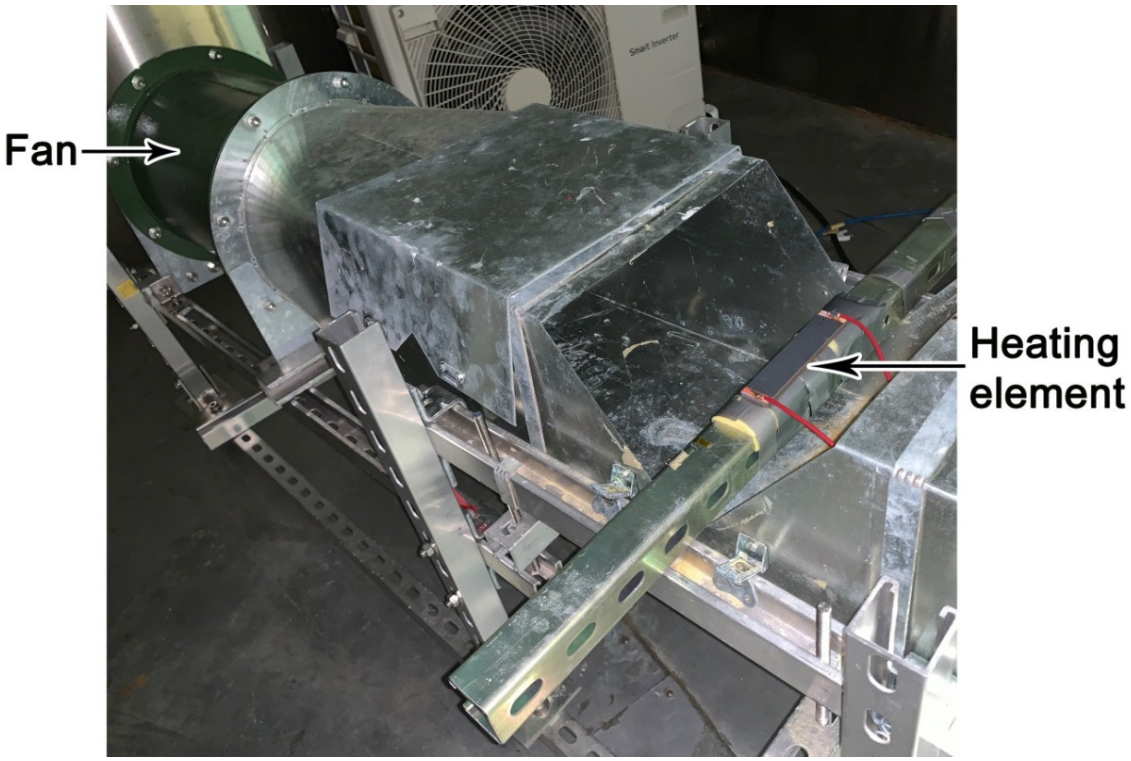

Figure 2-3 Testing apparatus for Joule heating.

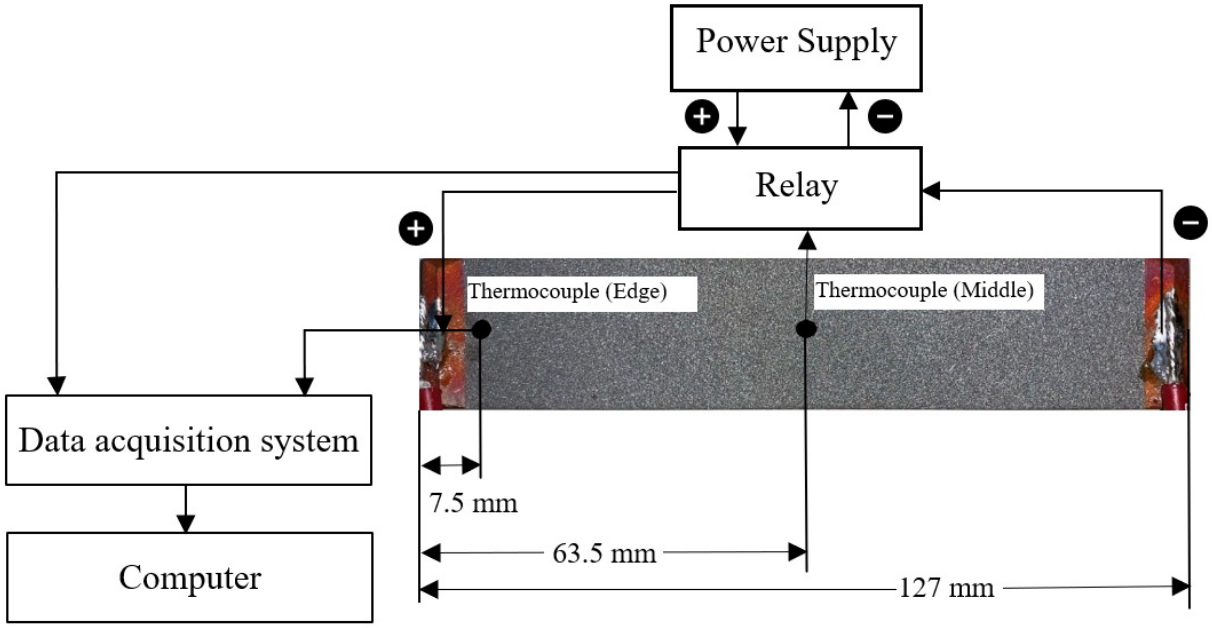

Figure 2-4 Schematic illustration of the experimental setup

For performing the tests under forced convection, a 0.25 kW direct-drive axial fan (DDA-12-10033B, Leader Fan Industries, Toronto, ON, Canada) was used to generate air flow with 8.6 m/s velocity. For the tests performed under free convection, the fan was turned off.

2.2 Heat Transfer Modelling and Numerical Simulations

Figure 2-5 shows the schematic of the geometry of the mathematical model for the two-layered coating composite system. This is a representation of a two-dimensional transient heat conduction model with energy generation for a two-layered slab. The top layer is the conductive electrical heating element, with a layer of electrical insulation (alumina) under it. The problem description schematic, along with dimensions and boundary conditions, are also shown in Fig 2-5. Near perfect thermal contact was assumed at the interface between the layers. This simplifying assumption is justified by the observation that no visible cracks, air bubbles, or other evidence of delamination were observed at the interface (see Fig 2-). In order to take advantage of the symmetry, $x = 0$ is positioned in the middle of the domain.

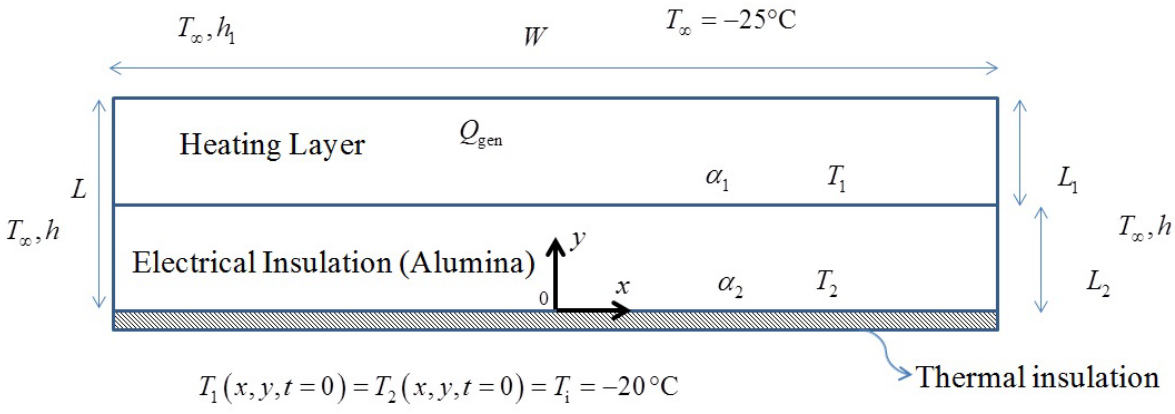

Figure 2-5 Schematic description of the transient heat conduction model

The governing equations for the temperature distribution functions are:

$$\alpha_1\left(\frac{\partial^2 T_1}{\partial x^2}+\frac{\partial^2 T_1}{\partial y^2}\right)+\frac{Q_{\text{gen}}}{\rho_1 C_{\text{p}_1}} = \frac{\partial T_1}{\partial t} \text{ and} \tag{1}$$

$$\alpha_2\left(\frac{\partial^2 T_2}{\partial x^2}+\frac{\partial^2 T_2}{\partial y^2}\right)=\frac{\partial T_2}{\partial t}. \tag{2}$$

The boundary conditions are given as

$$-k_1\frac{\partial T_1(x,\,L)}{\partial y} = h_1[T_1(x,\,L)-T_\infty], \tag{3}$$

$$T_1(x,L_2)=T_2(x,L_2), \tag{4}$$

$$\frac{\partial T_1(0,\,y)}{\partial x}=0, \tag{5}$$

$$k_1\frac{\partial T_1(x,\,L_2)}{\partial y} = k_2\frac{\partial T_2(x,\,L_2)}{\partial y}, \tag{6}$$

$$-k_1\frac{\partial T_1\left(\frac{W}{2},\,y\right)}{\partial x} = h\,[T_1(\frac{W}{2},\,y)-T_\infty], \tag{7}$$

$$-k_2 \frac{\partial T_2\left(\frac{W}{2}, \mathrm{y}\right)}{\partial x} = h\,[T_2(\frac{W}{2}, y)], \tag{8}$$

$$\frac{\partial T_2(x, 0)}{\partial y} = 0\,, \text{ and} \tag{9}$$

$$\frac{\partial T_2(0, y)}{\partial x} = 0\,. \tag{10}$$

The initial conditions are

$$T_1(t=0) = T_2(t=0) = T_{\mathrm{i}}\,. \tag{11}$$

In order to resolve the non-homogeneity of the boundary conditions, θ_1 and θ_2 were defined as follows [69]:

$$\theta_1 = T_1 - T_\infty \tag{12}$$

$$\theta_2 = T_2 - T_\infty \tag{13}$$

Due to the assumption of perfect thermal contact at the interface, the inner boundary conditions were homogeneous [39]. The superposition principle is used as a means to solve non-homogeneous problems. According to Hahn and Özişik [39], a non-homogeneous transient problem can be divided into a transient problem and a steady state problem, with the non-homogeneities transferred into the steady state problem:

$$T_{\mathrm{nH}}(\hat{r}, t) = T_{\mathrm{H}}(\hat{r}, t) + T_{\mathrm{SS}}(\hat{r}) \tag{14}$$

In Eq. 14, T_{nH} and T_{H} are the non-homogeneous and homogeneous transient problems, respectively. Note that the non-homogeneities in the governing equation and boundary conditions must not depend on time. For direct application of separation of variables and orthogonal expansion technique in a transient problem, all the boundary conditions must be homogeneous [39]. The only non-homogeneity should manifest itself in the initial condition. After proper application of the superposition principle, two homogeneous transient problems remained which were coupled to each other at the interface. For a two-dimensional problem with only one layer, the transient solution is of the general form:

$$\tau(t) = \exp[-\alpha(\lambda_n^{\,2} + \beta_m^{\,2})] \tag{15}$$

However, for a multi-layered problem, when applying separation of variables, the thermal diffusivity (α) should be retained on the side of space-dependent functions. This change of approach is implemented because in a composite problem, thermal diffusivity is discontinuous at the interfaces [39, 41]. Therefore, the eigenfunctions were of the forms $\sin(\frac{\lambda_{\mathrm{n}}}{\sqrt{\alpha_{\mathrm{i}}}}x)$ and $\cos(\frac{\lambda_{\mathrm{n}}}{\sqrt{\alpha_{\mathrm{i}}}}x)$ for the x-direction and $\sin(\frac{\beta_{\mathrm{m}}}{\sqrt{\alpha_{\mathrm{i}}}}y)$ and $\cos(\frac{\beta_{\mathrm{m}}}{\sqrt{\alpha_{\mathrm{i}}}}y)$ for the y-direction. Applying the aforementioned methodology and expanding it into a two-dimensional problem, the general form of the temperature distribution for the top layer was obtained as described by Eq. 16 as

$$T_1 = \sum_{\mathrm{n}=1}^{\infty}\sum_{\mathrm{m}=1}^{\infty} A_{\mathrm{nm}} \cos\left(\frac{\lambda'_n}{\sqrt{\alpha_1}}x\right)\left[\sin\left(\frac{\delta'_{\mathrm{m}}}{\sqrt{\alpha_1}}y\right) + \frac{G_{1\mathrm{m}}}{G_{2\mathrm{m}}}\cos\left(\frac{\delta'_{\mathrm{m}}}{\sqrt{\alpha_1}}y\right)\right] \times \exp\left[-\left(\lambda'_{\mathrm{n}}{}^2 + \delta'_{\mathrm{m}}{}^2\right)t\right] +$$

$$\sum_{n=1}^{\infty} a_n^{*} \cos\left(\lambda''_n x\right)[\sinh\left(\lambda''_n y\right)+\Lambda_n \cosh\left(\lambda''_n y\right)]+$$

$$\sum_{n=1}^{\infty} a_n \cos\left(\lambda_n x\right)[-\tanh(\lambda_n L_2)\sinh(\lambda_n y)+\cosh(\lambda_n y)]+\frac{-Q_{gen}}{2k_1}x^2+B+T_{\infty}. \quad (16)$$

In Eq. 16, G_{1m} and G_{2m} are defined as follows:

$$G_{1m}=\frac{-k_1\delta'_m}{\sqrt{\alpha_1}}\cos\left(\frac{\delta'_m}{\sqrt{\alpha_1}}L\right)-h_1\sin\left(\frac{\delta'_m}{\sqrt{\alpha_1}}L\right) \text{ and} \quad (17)$$

$$G_{2m}=h_1\cos\left(\frac{\delta'_m}{\sqrt{\alpha_1}}L\right)-\frac{k_1\delta'_m}{\sqrt{\alpha_1}}\sin\left(\frac{\delta'_m}{\sqrt{\alpha_1}}L\right) \quad (18)$$

The unknown constants, coefficients, and eigenvalues were obtained by applying the boundary and initial conditions. Orthogonality is invoked in the last step after the initial condition is applied. The results generated by application of this model were compared with experimentally obtained data acquired from the forced convection tests. Equation 19 shows the heat convection coefficient under forced convection from Pohlhausen's solution for a laminar flow regime [70, 71]. In the case of mixed flow, the average heat transfer coefficient over a flat plate was obtained using White's model and Colburn's analogy [70-72]. Assuming that Reynolds number for transition from laminar to turbulent flow over the plate was 5×10^5, the average Nusselt number is given by Eq. 20. For natural convection from a horizontal plate that is heated

at the upper surface, the correlation equation developed by Lloyd and Moran [73] was used, which is shown in Eq. 21:

$$\overline{\mathrm{Nu}_L} = \frac{\bar{h}L}{k} = 0.664\,\mathrm{Pr}^{1/3}\sqrt{\mathrm{Re}_L}; \quad 0.6 < \mathrm{Pr} < 10 \tag{19}$$

$$\overline{\mathrm{Nu}_L} = \frac{\bar{h}L}{k}\left(0.0158\mathrm{Re}_L^{\,6/7} - 739\right)\mathrm{Pr}^{1/3} \tag{20}$$

$$\overline{\mathrm{Nu}_L} = \frac{\bar{h}L}{k} = 0.54\,\mathrm{Ra}^{1/4}; \quad 10^5 < \mathrm{Ra} < 2\times10^7 \tag{21}$$

2.3 Results and Discussion

2.3.1 Coating Characterization- Preliminary Testing

Figure 2-6 shows a backscattered SEM image of the NiCrAlY coating. It is evident that the NiCrAlY layer has adhered well to the alumina coating beneath it. Furthermore, no delamination of alumina from the steel substrate is observed. The good adhesion of alumina to the substrates results in proper electrical insulation and prevents short circuiting of the metal top coating during heating. Although a number of non-molten or partially molten NiCrAlY particles are present, it can be seen that most of the particles have been fully melted and formed into splats. Table 2-4 lists the average porosity, thickness, and the volumetric percentage of the matrix and reinforcing phases for the MMC coatings. Using image analysis, the average thickness and porosity of the NiCrAlY layer were 121 μm and 10.2%, respectively.

Table 2-4 Average porosity, thickness, and volumetric percentage of the matrix and reinforcing phases for NiCrAlY-Al_2O_3 (S3), NiCrAlY-TiO_2 (S4), and NiCrAlY-WC-12Co (S5).

	S3	S4	S5
Thickness [μm]	130	238	165
Porosity (%)	13.4	1.8	11.7
Matrix phase [Vol%]	24	7.2	53.3
Reinforcing phase [Vol%]	61.8	90.9	33.8

As shown in Figure 2-7, the alumina at the NiCrAlY-alumina MMC showed excellent cohesion with the layer of alumina located below it. As a result, no clear boundary could be observed between the different layers of coating. Given the relatively higher melting point of alumina, a significant portion of alumina particles have not been fully melted. Mechanical interlocking between the NiCrAlY matrix and the partially molten alumina particles promotes the adhesion within the MMC coating.

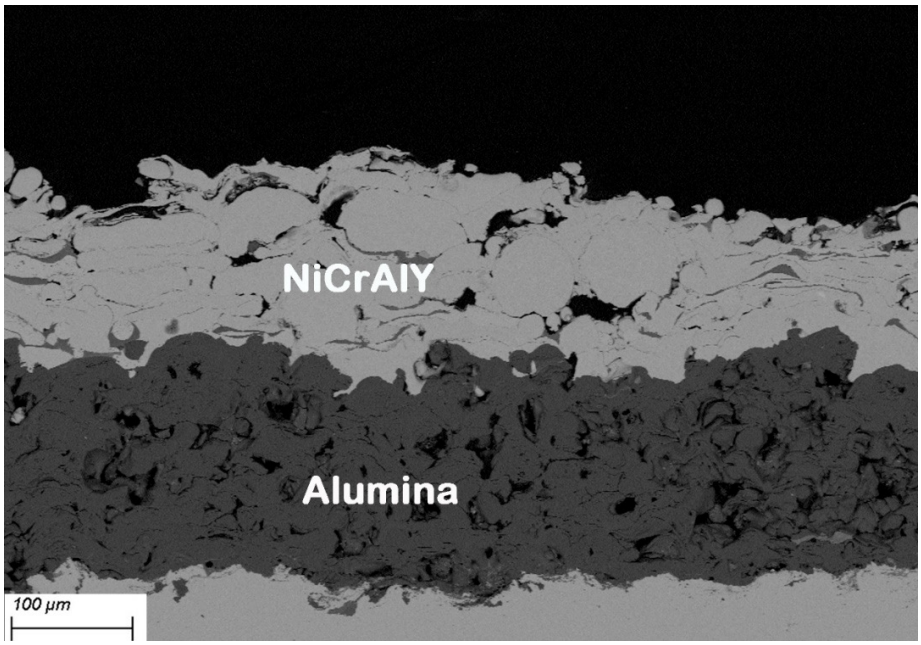

Figure 2-6 Backscattered SEM image of the microstructure of the NiCrAlY coating

Since a portion of the cross-sectional area of the NiCrAlY coating is now occupied by a dielectric material, in this case alumina, the flow of electrons through the NiCrAlY-alumina coating is expected to be significantly less than that of pure NiCrAlY. Thus, the electrical resistance of the resistive heating coatings is expected to increase when using reinforcing phases with dielectric behavior.

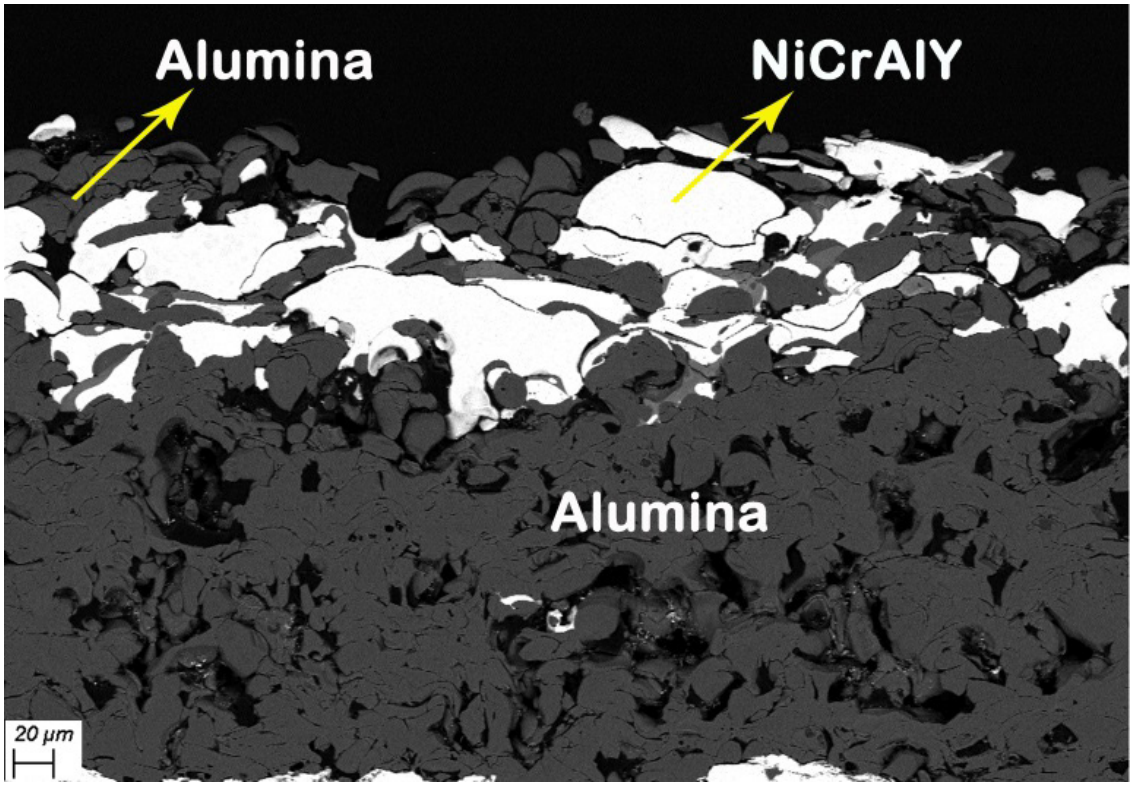

Figure 2-7 Backscattered SEM image of the microstructure of the NiCrAlY-alumina MMC coating

Figure 2-8 shows the backscattered SEM image of the NiCrAlY-WC-12Co coating. Although tungsten carbide is not a dielectric material, it was considered in this study owing to its well-established impact on promoting wear-resistance and hardness of MMC coatings [34, 36,

38].As observed in Fig 2-8, the MMC coating has good adhesion to the alumina layer. It is observed that the reinforcing phase is well dispersed through the matrix. Adhesion, through mechanical interlocking and metallurgical bonding, likely contributed to the integrity of the NiCrAlY-WC-12Co MMC coating. Figure 2-9 shows an image of the cross-section of the NiCrAlY-titania MMC coating that was captured in backscattered electron mode of the SEM.

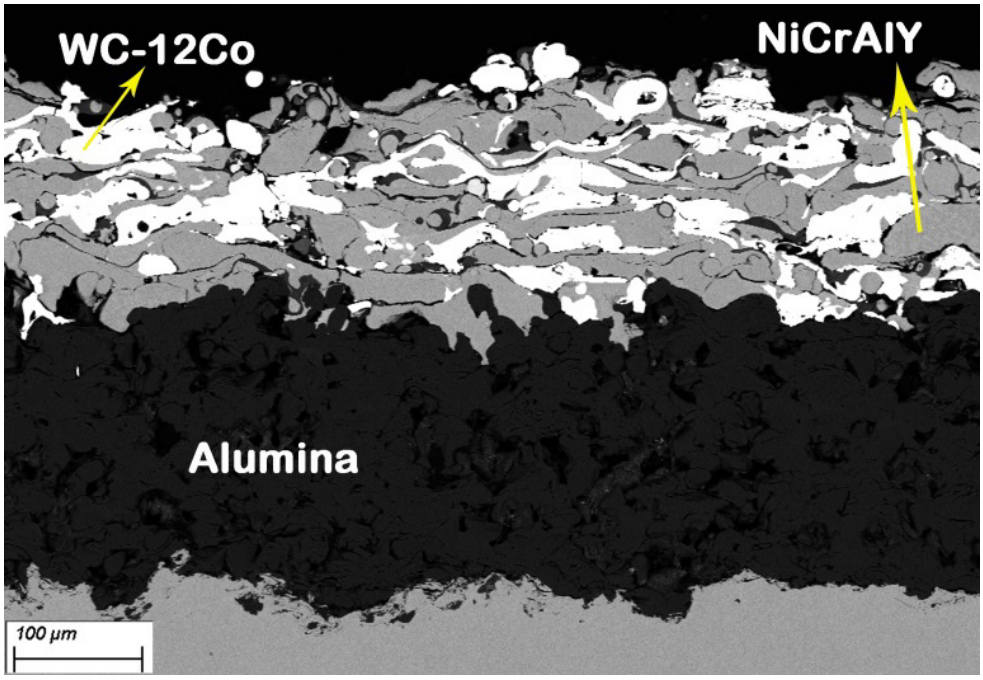

Figure 2-8 Backscattered SEM image of the microstructure of the NiCrAlY-WC-12Co MMC coating

In this study, titania was considered because of its low electrical conductivity and semi-conductor properties under certain conditions. From Fig 2-9, it is observed that the volumetric percentage of the ceramic phase in the final coating is appreciably higher than that of the other MMC coatings. This could be mainly due to the considerably lower melting point of titania compared to alumina and tungsten carbide. Thus, a large percentage of titania particles were

fully molten and have adhered well to the alumina coating. Moreover, good cohesion and consequently low porosity were observed within the reinforcing phase itself. As shown in Fig 2-9, it appears that there is good adhesion between the NiCrAlY matrix and what was to be the reinforcing phase titania.

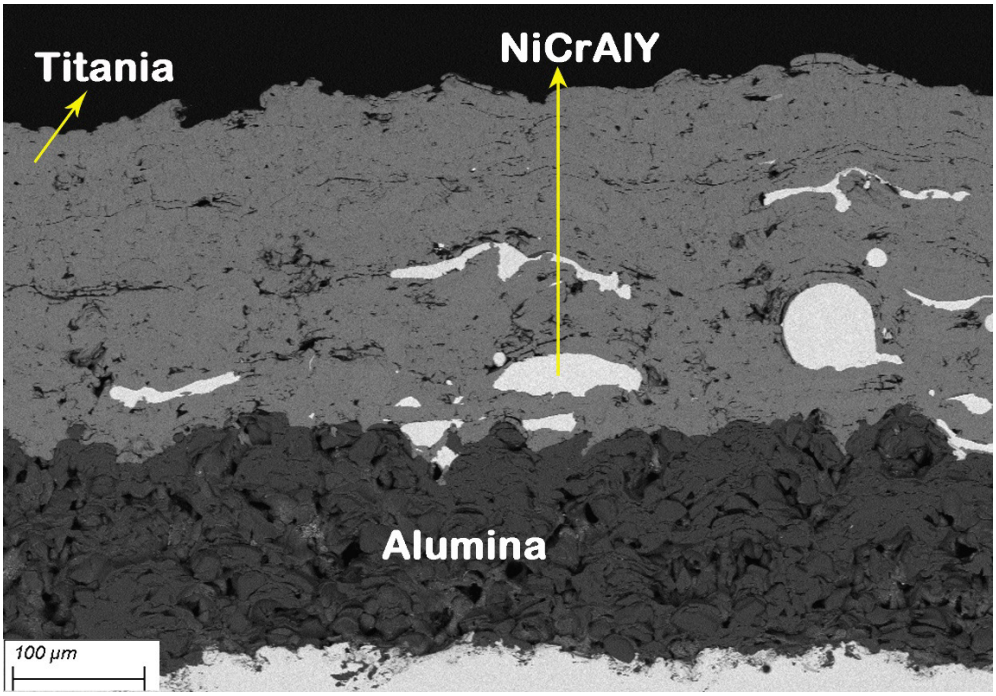

Figure 2-9 Backscattered SEM image of the microstructure of the NiCrAlY-titania coating

2.3.2 Joule Heating Experiments- Preliminary Testing

Prior to conducting the Joule heating experiments, the values of electrical resistance of the coatings (the heating elements) were measured. Table 2-5 lists the average values of electrical resistance that were measured at room temperature for the heating elements in this study. The voltages that were applied across the coatings initially for the Joule heating tests of each coating heating element are also listed in Table 2-5.

Table 2-5 Electrical resistance for different coating heating elements and initial applied voltages

	R [Ω]	V [V]
NiCrAlY	0.238	4.9
NiCrAlY-Al_2O_3	3.170	48.1
NiCrAlY-TiO_2	67.632	60
NiCrAlY-WC-12Co	0.153	3.6

As expected, the resistance of the NiCrAlY-titania MMC coating was significantly greater than that of the other coatings. This could be attributed to amount of titania that was deposited and the relatively higher thickness of this coating. As indicated in Table 2-5, the NiCrAlY coating has a higher resistance than that of the NiCrAlY-WC-12Co MMC coating. This difference in resistance was possibly due to two reasons: 1) lower thickness of the NiCrAlY coating 2) compaction of the matrix phase (NiCrAlY) by the tungsten carbide reinforcing particles and the increase in the effective space for the flow of electrons through the coating.

Owing to the dielectric behavior of alumina, the NiCrAlY-alumina MMC coating exhibited considerably higher resistance than that of the NiCrAlY control coating. The alumina particles that were dispersed through the matrix inhibited the flow of the charged electrons and consequently reduced the effective cross-sectional area for the flow of those electrons. As a result, the electrical resistance of the NiCrAlY-alumina coating heating element was higher than that of the NiCrAlY coating heating element.

Figure 2-10 shows the surface temperature of the different heating elements at the center of the samples versus time in the Joule heating tests under free heat convection. The surface temperature will likely be a maximum close to the center of the sample [28]. Accordingly, the measured temperatures will likely represent the maximum surface temperature of the coated surface. In order to evaluate the heating performance of the elements in low ambient temperatures, all the Joule heating experiments were conducted at an ambient temperature of -25 °C. Since the electrical resistance varies significantly among different elements, applying the same voltage to all the elements was not appropriate in order to compare their heating performance. For this reason, the applied voltage for each element was adjusted such that the maximum heat generation using the same DC power supply was produced.

Based on Ohm's law, heating elements with lower values of electrical resistance required lower voltages to generate the same amount of electrical current. The maximum allowable electrical current was fixed to 15 A for all the tests. The generated power is the product of voltage and current, and is the most significant factor in evaluating the heating performance of the elements. In the Joule heating tests, the initial values of generated power for NiCrAlY, NiCrAlY-titania, NiCrAlY-WC-12Co, and NiCrAlY-alumina were 73.5 W, 66 W, 54 W, and 714 W, respectively.

The electrical resistance of the NiCrAlY-titania coating decreased by 50% after a temperature increase of 60 °C. As reported by Al-Aql [74], the electrical resistivity of Ni-Cr alloys increase considerably with increases in temperature. However, for the NiCrAlY-titania coating, a significant decrease in resistance was observed with increasing temperature. This

phenomenon could have been caused by the electrical behavior of titania as a semi-conductor, therefore, leading to higher electrical conductivity and consequently lower resistance.

As shown in Figure 2-10, the heating performance of the NiCrAlY-alumina MMC coating was significantly higher than that of other coatings. The NiCrAlY-alumina heating element was able to reach 20 °C after only 11 seconds, while it took much longer for other elements to reach the same temperature. It is evident that NiCrAlY-WC-12Co coating has the weakest heating performance. Besides its relatively low electrical resistance, the high thermal conductivity of WC-12Co (around 90 W/m.°C) causes this heating element to exchange heat with the environment at a higher rate.

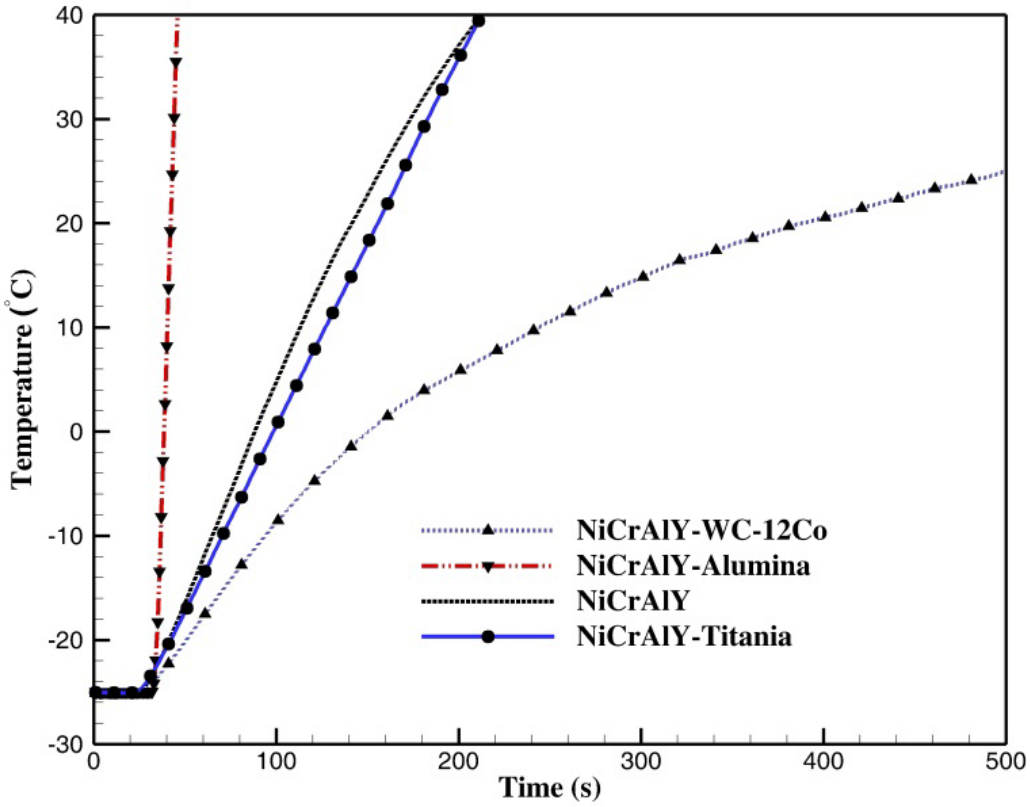

Figure 2-10 Surface temperature of the different heating elements at the sample middle section versus time in the Joule heating tests under free convection

As a result, it will take longer for the surface temperature of this MMC coating to reach a specific value compared with the other elements. Immediately after applying the electrical current, the electrical resistances of NiCrAlY, NiCrAlY-WC-12Co, and NiCrAlY-titania coatings increased by 38%, 56%, and 47%, respectively. The electrical resistance of the NiCrAlY-alumina coating increased by only 2% after connection to the power supply.

Owing to the appreciable improvement in the heating performance of the NiCrAlY-alumina coating heating element, it was selected for further study under Joule heating tests under forced heat convection. These tests were performed for two different voltages namely, 10 V and 20 V. Similar to the free convection tests, the ambient temperature in the cold room was fixed on -25 °C.

Figure 2-11 shows the surface temperature of middle section of the NiCrAlY-alumina coating samples versus time for two different voltages under forced convection. It is observed that the surface temperature increased at a higher rate when 20 V and 6.3 A were applied compared to when 10 V and 3.1 A were applied. Nevertheless, even over 10 V, which supplies a power of around 30 W, the surface temperature was 0 °C in less than 150 seconds. This makes the NiCrAlY-alumina coating heating element a good candidate for implementation in de-icing systems.

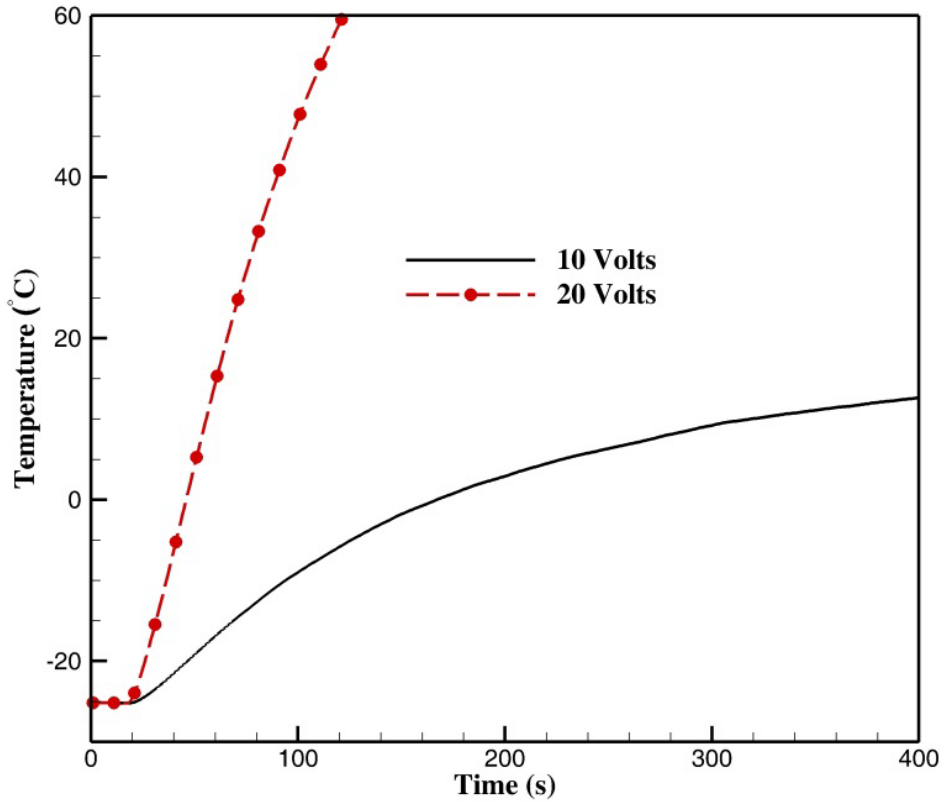

Figure 2-11 Surface temperature of the middle section of NiCrAlY-alumina coating heating element versus time in the Joule heating tests under forced convection

2.3.3 Coating Characterization- Modified Testing System

Given that this study primarily focuses on a comparative investigation of the performance of coatings as heating elements, low carbon steel substrates were employed, instead of FRPC or Al alloys, which are commonly used in aerospace and wind-based renewable energy generation sectors. Back-scattered electron images of the microstructure of all the coatings were captured and shown in Fig 2-12. As shown in Fig 2-12 (a), there are no observed discontinuities, cracks, or other evidence of delamination at the interface between the NiCrAlY and alumina coating, which supports the simplifying assumption of near perfect contact between the layers of the coatings. Moreover, most of these particles have formed splats and are fully melted. It can be

observed that the particles that were fully molten upon impact in the NiCrAlY coating layer have good cohesion to each other. Given that the tungsten carbide has the highest melting point compared with other deposited ceramic particles, the spraying parameters were adjusted so that they could reach relatively higher temperatures during deposition. It is observed that the tungsten carbide particles have dispersed well throughout the NiCrAlY matrix. Based on the microstructure demonstrated in Fig. 2-12 (b), most of the tungsten carbide particles have been fully melted. Due to the low degree of discontinuity between the matrix and the reinforcing phase, it is likely that NiCrAlY and tungsten carbide particles adhered well to each other.

Table 2-6 lists the average thickness, porosity, and the weighted percentage of both the matrix and the reinforcing phases for all the fabricated MMC coatings. As shown in Fig 2-12 (c), most of the alumina particles have been fully melted and the reinforcing phase is well distributed in the matrix. In a study conducted by Mohammadian Bajgiran *et al*. [75], a detailed phase analysis of flame sprayed alumina (deposited using the same equipment and feedstock alumina powder) was given. It was reported that the alumina feedstock powder was pure alpha phase alumina (α-Al_2O_3), while the deposited alumina coating contained around 60% α-Al_2O_3. Based on the results of the XRD and Raman spectroscopy, they suggested that the initial α-Al_2O_3 was maintained at the center of the flame sprayed particles (light gray phase), while their outer layer was γ-Al_2O_3 (dark gray phase). The porosity of the NiCrAlY-alumina coating is noticeably higher than that of the NiCrAlY-WC-12Co, and a higher degree of discontinuity is observed between the matrix and reinforcing alumina phase. Furthermore, in terms of homogeneity, the NiCrAlY-WC-12Co coating exhibits a more uniform and homogeneous microstructure. The content of WC-12Co in the coatings was 38.6 wt.%, which is the closest to the original tungsten carbide content in the feedstock material, which was 40 wt.%.

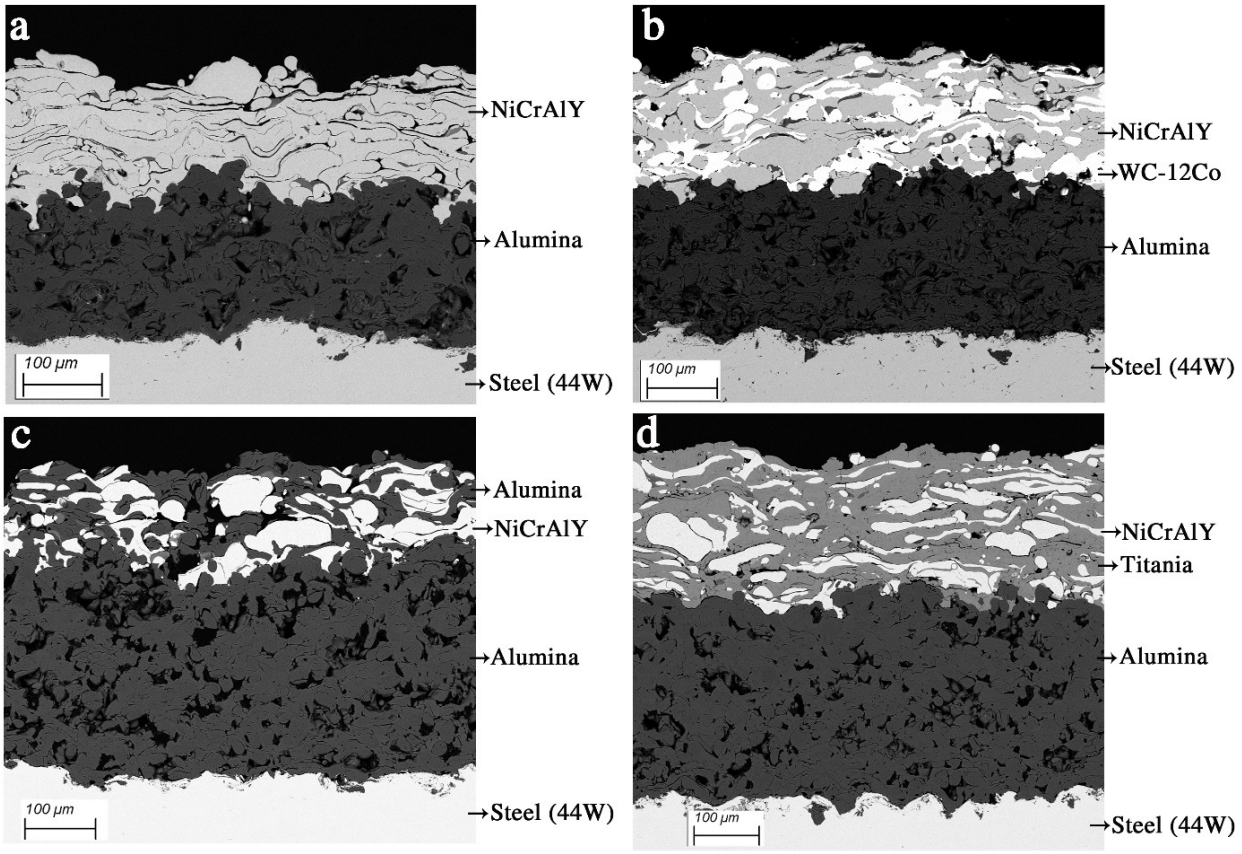

Figure 2-12 Back-scattered electron image of the microstructure of the coatings: a) NiCrAlY, b) NiCrAlY-WC-12Co, c) NiCrAlY-alumina, d) NiCrAlY-titania.

Table 2-6 Characteristic parameters of the coatings

Coating characteristic	NiCrAlY	NiCrAlY-WC-12Co	NiCrAlY-Al_2O_3	NiCrAlY-TiO_2
Porosity [%]	3.9	4.3	7.5	2.4
Thickness [µm]	164 ± 8	167 ± 8	149 ± 9	177 ± 6
Matrix phase [wt. %]	-	61.4	73.2	55.1
Reinforcing phase [wt. %]	-	38.6	26.8	44.9
Matrix phase [vol. %]	-	65.8	54.7	38.1
Reinforcing phase [vol. %]	-	29.9	37.8	59.5

From Table 2-6, it is observed that the NiCrAlY-titania coating has the lowest porosity of all the MMC coatings. Also, the NiCrAlY-titania coating contains the highest weight percentage of reinforcing phase compared to the other MMC coatings. The existence of only a few visible gaps in the boundaries between the two phases is likely caused by good mechanical interlocking. As shown in Fig 2-12 (d), it appears that the titania particles were molten compared to the other deposited ceramic reinforcements. This could be partly due to their melting point which is considerably lower than that of alumina and tungsten carbide. The electrical resistivity of the coating-based heating elements is considerably affected by microstructure of the coatings along with the electrical properties of the matrix and reinforcing phases. Due to the relatively low thermal conductivity of the entrapped air inside the pores, porosity should also be considered as a significant factor in determining the electrical resistance.

Electrical properties of composite coatings containing electrically conductive metal particles generally depend on the geometrical configuration, volume fraction of different phases, porosity, and the electrical properties of the individual coating material phases [48, 76]. In addition, existence of oxides and microcracks could noticeably affect the electrical resistivity of coatings containing Ni and Cr [48, 77]. Electrical resistivity of materials is an intrinsic property and independent of physical dimensions of the heating elements. As reported by Ashrafizadeh *et al*. [78], electrical resistivity decreases with reduction in the coating porosity. Furthermore, due to formation of oxides during the flame-spraying process and the high electrical resistivity of oxides, they could noticeably hinder the passage of electrons through the coating-based heating

element [78]. In this study, varying spraying parameters among different MMC coatings has likely generated different levels of oxidation within the materials.

Table 2-7 lists the averaged electrical resistance and apparent electrical resistivity of the heating elements. In this study, the chosen materials for the reinforcing phases have distinctly different electrical properties. Owing to the dielectric behavior of alumina, the effective cross-sectional area for passage of electrons in NiCrAlY-alumina coatings will be lower than that of the single phase NiCrAlY coating. In NiCrAlY-alumina coatings, the electrons are forced to pass only through the metal matrix. As a result, the electrical resistance of NiCrAlY-alumina is expected to be significantly higher than that of NiCrAlY, which is confirmed by measurements listed in Table 2-7. The semi-conductive behavior of titania and its higher electrical resistivity, compared to NiCrAlY, could be used to explain its relatively high electrical resistance. In the case of titania and due to its electrical properties as a semiconductor, oxidation of materials such as Cr could increase the electrical conductivity of titania by placing oxides and impurities, e.g. Cr_2O_3, within its crystal lattice structure [77]. This could explain the lower electrical resistance in NiCrAlY-titania coatings compared to that of NiCrAlY-alumina coatings. The electrical conductivity of tungsten carbide is considerably higher than that of NiCrAlY. Thus, it is expected that the tungsten carbide phase dispersed in the metal matrix would contribute to an enhanced electrical conductivity by providing ease of passage for electrons.

According to Al-Aql [74], the electrical resistance of Ni-Cr alloys exhibits an appreciable increase with considerable increases in temperature. However, the range of temperature variations in this study is significantly less than that studied by Al-Aql [74]. As a result, the variation of electrical resistance with temperature for the tested heating elements was negligible

within the temperature ranges observed in this research. Figure 2-13 shows the variation of electrical current with temperature which shows negligible variation in electrical resistance with temperature for heating elements under study. It should be noted that the variation between electrical resistances of the heating elements deposited with the same powder and identical spraying parameters did not exceed 5%.

Table 2-7 Values of electrical resistance and apparent electrical resistivity

Coating	Electrical resistance [Ω]	Electrical resistivity [Ω -µm]
NiCrAlY	0.24	6.5
NiCrAlY-WC-12Co	0.15	5.7
NiCrAlY-alumina	3.20	93.5
NiCrAlY-titania	1.84	57.3

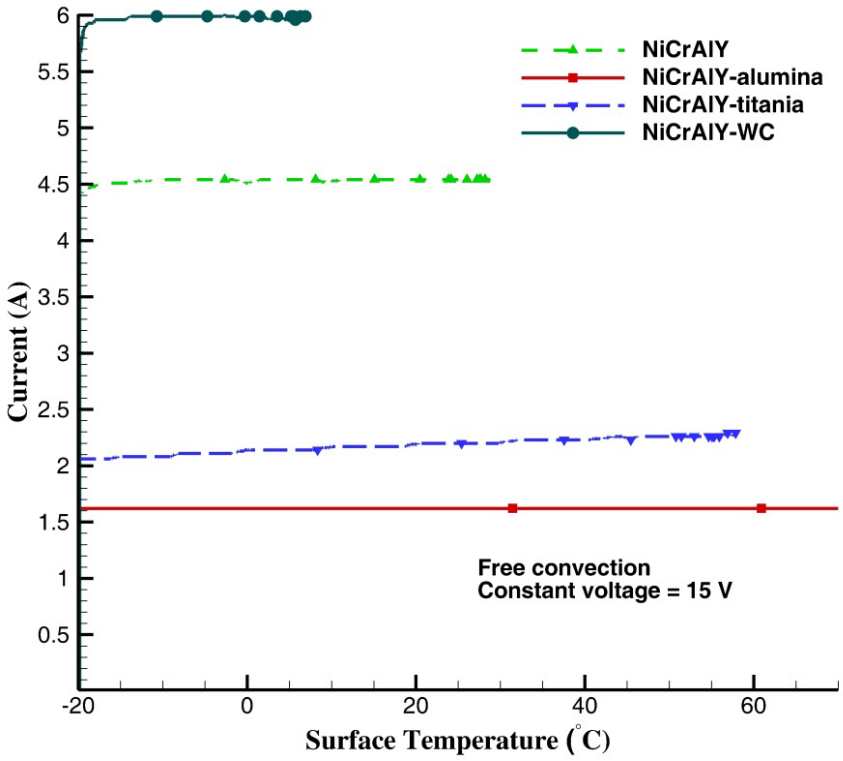

Figure 2-13 Variation of electrical current with temperature under free convection

2.3.4 Joule Heating Experiments- Modified Testing System

Joule heating tests were conducted with the metal matrix composite coatings as a proxy measurement of their heating performance. Figures 2-14 and 2-15 show the mid-section surface temperature of the heating elements, for free and forced convection, respectively. These figures highlight a comparative representation of the increasing surface temperature behavior of the coatings under study. The NiCrAlY-alumina coating had an average ramp-up rate of 0.044 °C/s and 0.026 °C/s for forced and free convection, respectively, which were the highest values of all the metal matrix coatings that were studied. In addition to the ramp-up rate, the value of the achieved steady-state temperature is of great significance, especially in de-icing and anti-icing applications.

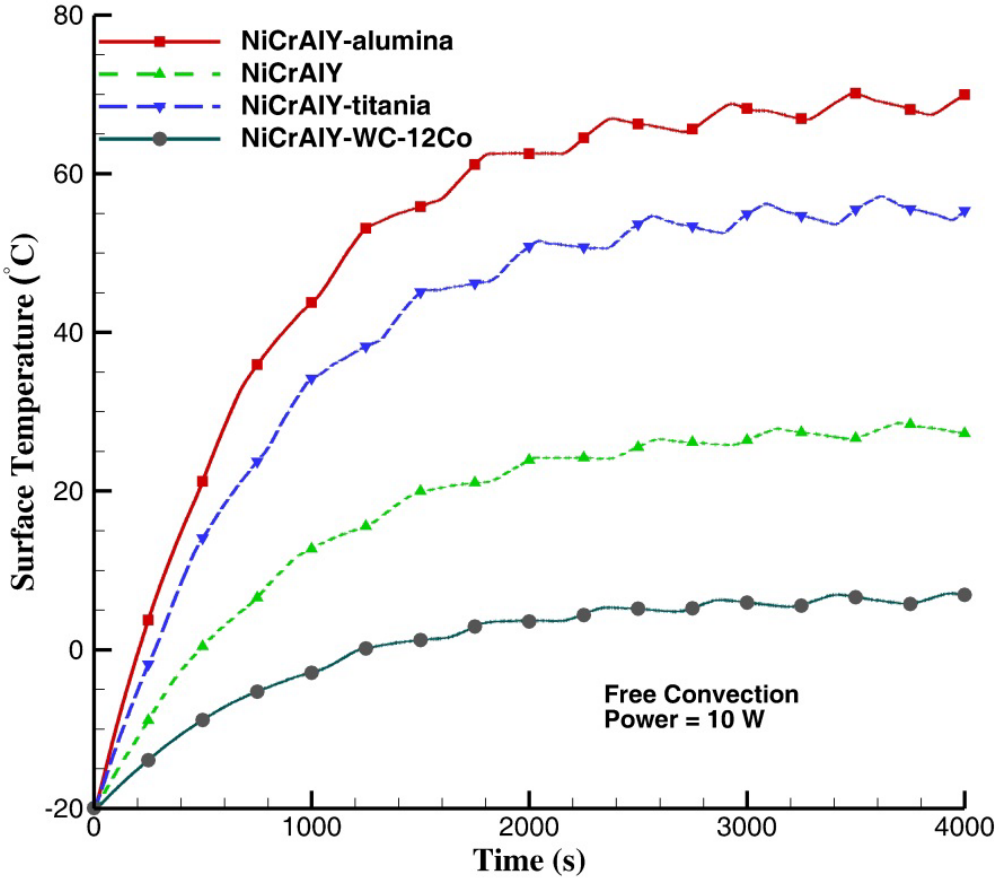

Figure 2-14 Surface temperature of the elements at the middle versus time- Free convection

In forced convection experiments, NiCrAlY and NiCrAlY-WC-12Co coatings could not reach the melting temperature of ice, i.e. 0 °C. In contrast, NiCrAlY-alumina and NiCrAlY-titania coatings achieved steady-state temperatures of 15.1 °C and 8.4 °C, respectively, which shows their superior de-icing capability. The fluctuations in graphs pertaining to the free convection tests was likely due to the intermittent operation of the cold room cooling system. Using a thermostat, the compressor stops operating when the room reaches -25 °C and restarts after a temperature increase of 1 °C to 2 °C.

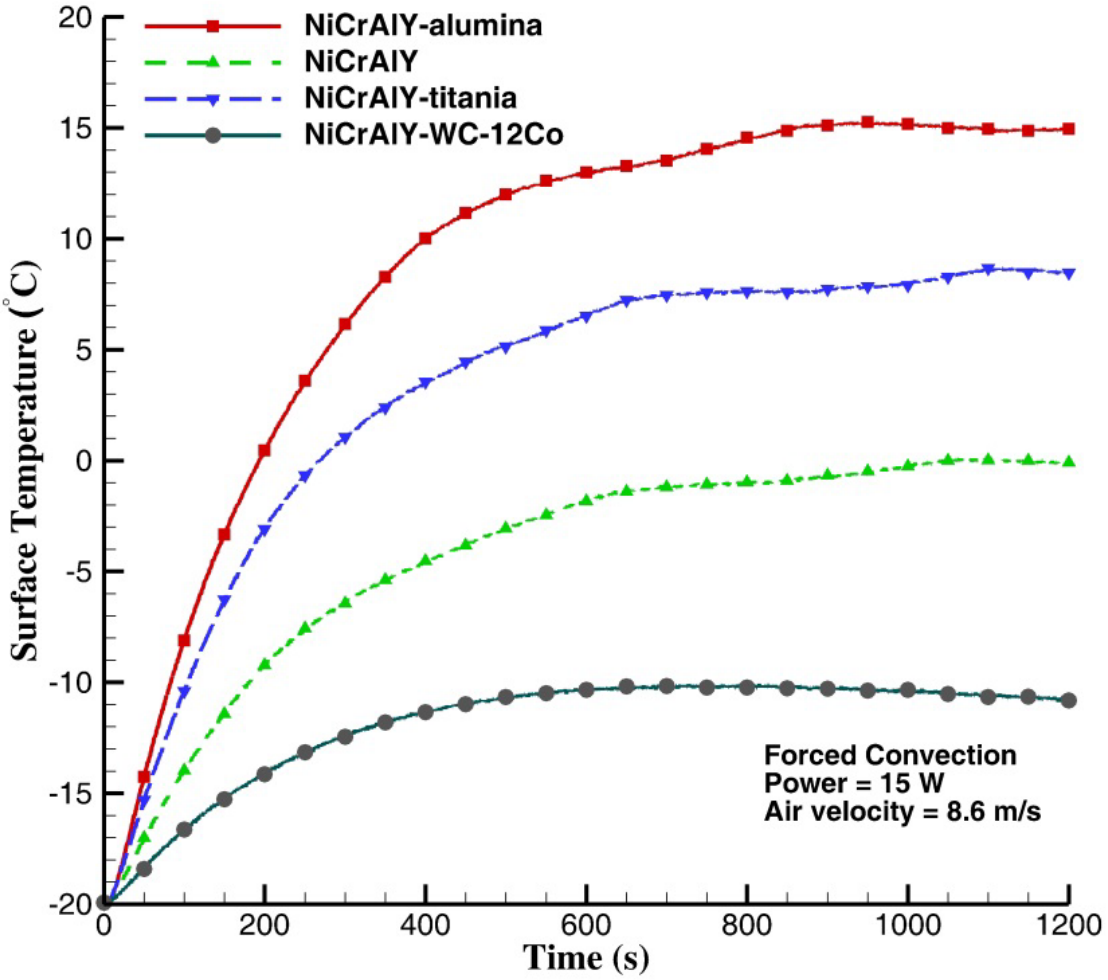

Figure 2-15 Surface temperature of the different heating elements at the middle section versus time- Forced convection

The experimentally obtained results suggest that MMC coating heating elements with relatively higher resistances show better heating performance. In electric flow through a potential difference, the collision of electrons with material atoms generates heat. Accordingly, the microstructure, pores, cracks, and material properties play an important role in determining the amount of the generated heat. This impact of microstructure and coating properties presents itself as electrical resistivity and has significant impact on heating performance [79]. However, in addition to Joule heating, another phenomenon namely, electro-migration also occurs when a current with high current density is induced in an electrical element [80].

Electro-migration is a form of enhanced atomic diffusion and is highly affected by material microstructure and properties similar to Joule heating. Dissipation of the heat generated by Joule heating is partly impacted by kinetics of electro-migration and is not only a function of resistivity. As a result of electro-migration, the degree of Joule heating around the voids (e.g. porosities) will increase and the local current density will reduce in locations with larger electrically conductive cross-sections [80]. Due to the evident variation in the microstructure, and electrical properties of the particle reinforcement materials used in the MMC coatings under study, electro-migration could appreciably affect the heating performance of the elements.

The primary reason for selecting reinforcing materials with considerably different electrical properties was to examine the utility of MMCs as a means to manipulate electrical resistance and consequently heating performance of the heating elements. Although the amount of applied power was approximately the same for all the MMC coating heating systems, the total amount of consumed energy (RI^2t) for achieving a certain target temperature significantly varied with the coating composition and material phases.

For instance, for the free convection experiments, the NiCrAlY-alumina MMC coating heating element consumed only 2,070 J in order to reach 0 °C, which is significantly less than that of NiCrAlY, which required 4,830 J of energy. Therefore, in order to minimize the amount of energy consumption, employing MMCs fabricated with low-resistance or dielectric particulate reinforcement is an energy efficient and practical methodology for de-icing purposes.

Based on conservation of energy, the surface temperature continues to rise as long as the generated heat on the surface is more than the heat removed from it by convection. In general, the heat transfer rate for free convection is considerably less than that of forced convection. This might explain the observation that the experiments conducted under forced convection have reached the steady state at a higher rate. Despite the equal amount of supplied power, the heating elements demonstrated different amounts of heat generation.

For Ohmic materials, the amount of Joule heating in an element is directly proportional to its electrical resistance (R) and square of the electrical current (I) that flows through it, i.e. RI^2. However, a resistive heating element is not necessarily the only medium in the circuit with considerable electrical resistance. The R in $P = RI^2$ should account for the overall electrical resistance between the two terminals of the power supply. For this reason, for relatively low-resistance heating elements, e.g., NiCrAlY, a relatively greater portion of the generated heat is dissipated through the wires, plugs, and other connections.

Contrary to electrical resistivity, electrical resistance is highly affected by the length and the cross-sectional area of a heating element. In order to study the impact of coating thickness on electrical resistance and heating performance, two NiCrAlY-titania coatings were fabricated using different numbers of deposition passes to create significantly different coating thicknesses.

As expected, the coating with the higher thickness (177 ± 6 µm versus 252 ± 7 µm) exhibited lower electrical resistance. Figure 2-16 illustrates a comparison between the heating performance of these heating elements under forced convection and 20 V.

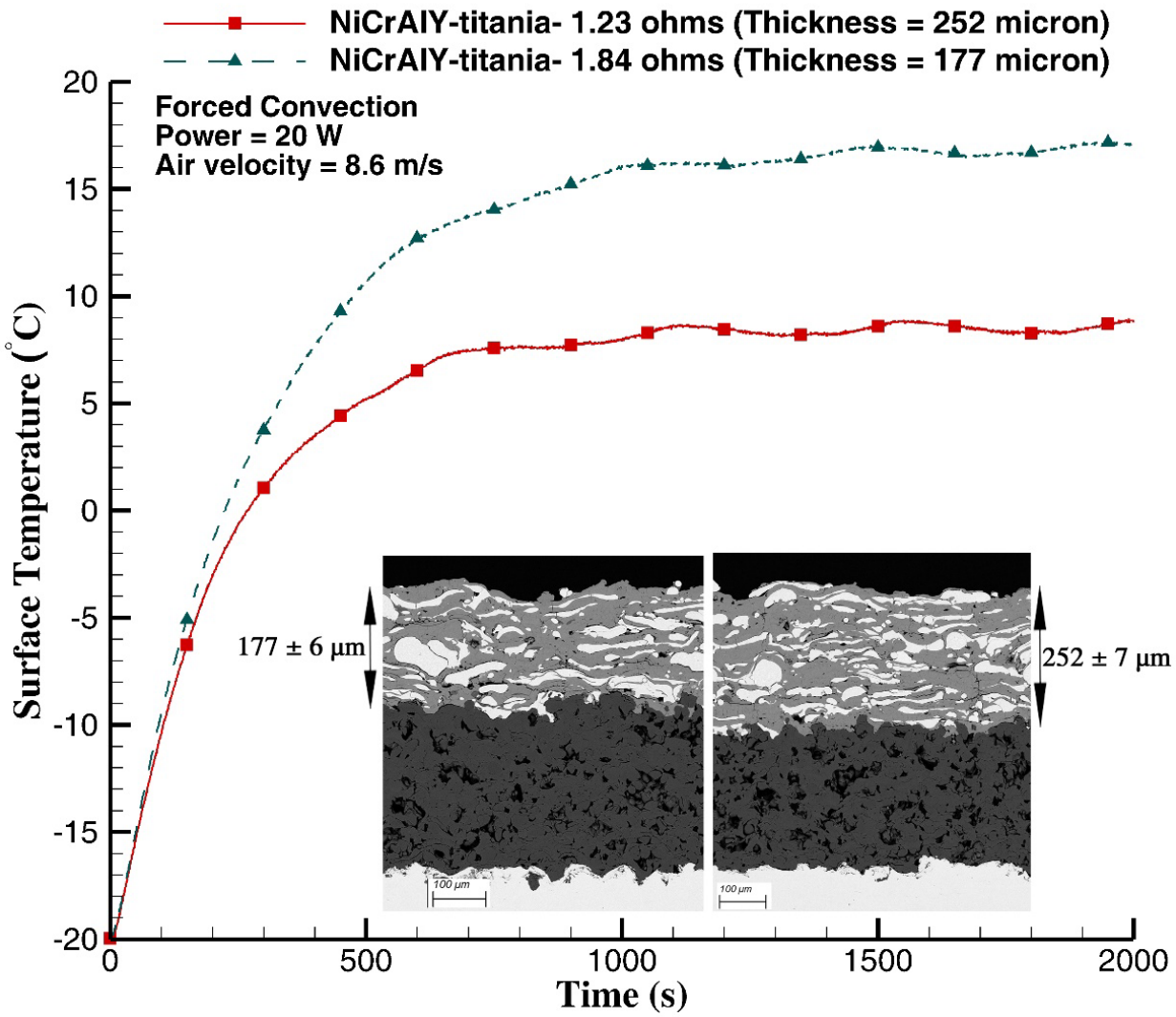

Figure 2-16 Surface temperature and SEM images of the NiCrAlY-titania coatings with different thicknesses under forced convection

2.3.5 Heat Transfer Modelling and Numerical Simulations

Figures 2-17 and 2-18 show a comparison between the results of the coating surface temperature trace obtained from the developed transient heat transfer model and experimentally obtained data for NiCrAlY-alumina coating. The temperature is measured in the middle section of the top surface. A numerical simulation for predicting the transient temperature distribution of the two layers of the NiCrAlY-alumina coating was also conducted using ANSYS Mechanical. For the ANSYS simulation, the carbon steel substrate was incorporated to the solution domain to account for the heat loss from both sides of the elements. Maxwell theoretical model was applied in order to calculate the thermal conductivity of metal matrix composites [81]. It is clear that both the analytical solution and that of the simulations are in good agreement with the experimentally obtained results. Using absolute temperature (˚K) for consistency in error estimations, both calculations overestimate the steady-state temperature by no more than 2%. This could be attributed to the error caused by the employed correlations estimating convection heat transfer coefficient.

The Lloyd and Moran correlation for free convection [73] is suitable for isothermal surface and surfaces with uniform heat flux with different approaches for calculating the Rayleigh number. However, none of these conditions applied to the experiments conducted in this study. In addition, imperfect thermal insulation at the bottom could be a cause of heat loss which is not reflected in the model. ANSYS Mechanical simulations were conducted for the entire domain, including the carbon steel substrate. As a result, these simulations have slightly better agreement with the experiments. The mathematical approach presented in this study does allow for greater flexibility to understand the physics of the problem better and modify

underlying parameters as the coatings are further improved to expand energy generation performance and efficiency.

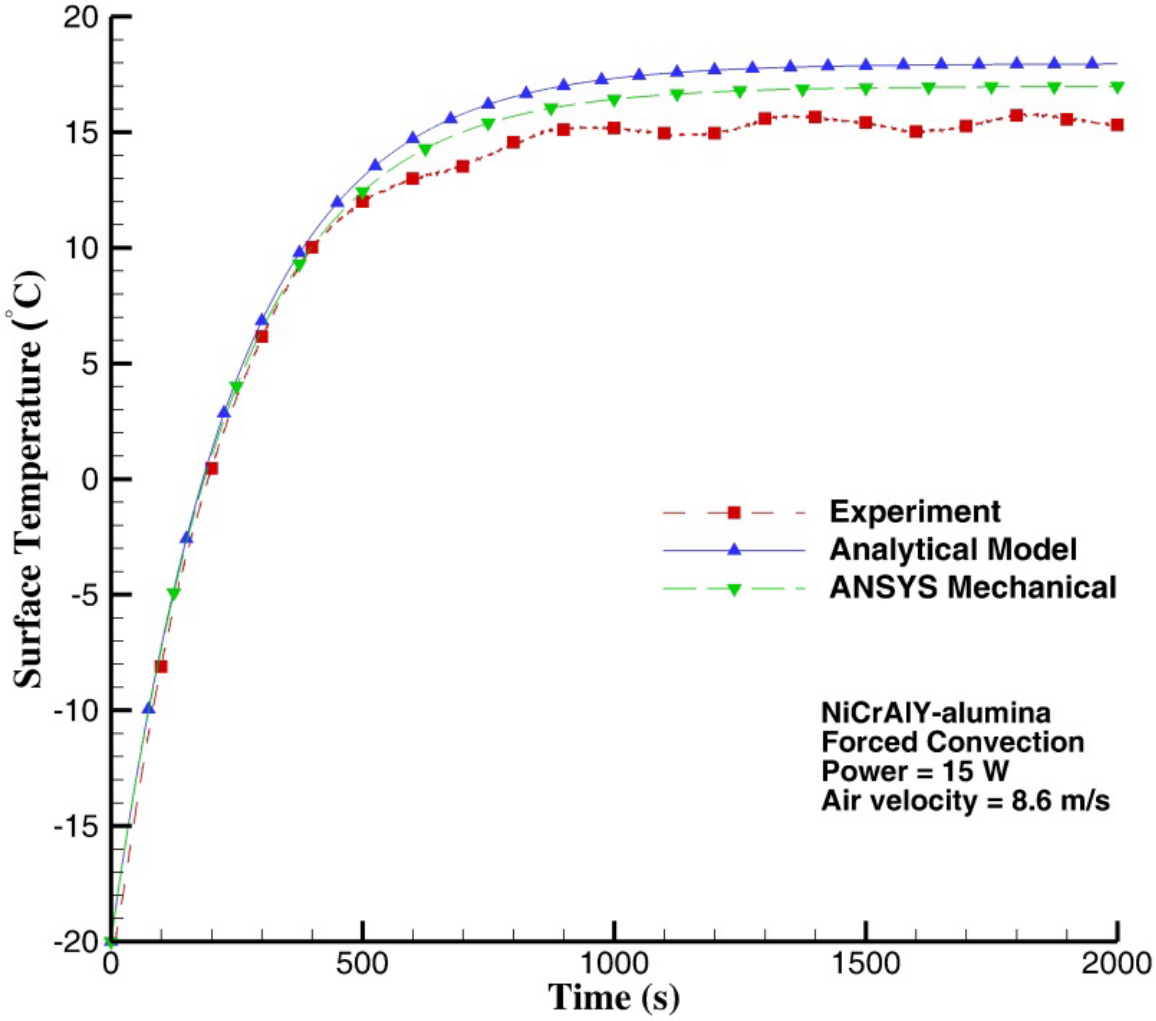

Figure 2-17 A comparison between the experimental data and the results of the mathematical model and ANSYS Mechanical- Forced convection

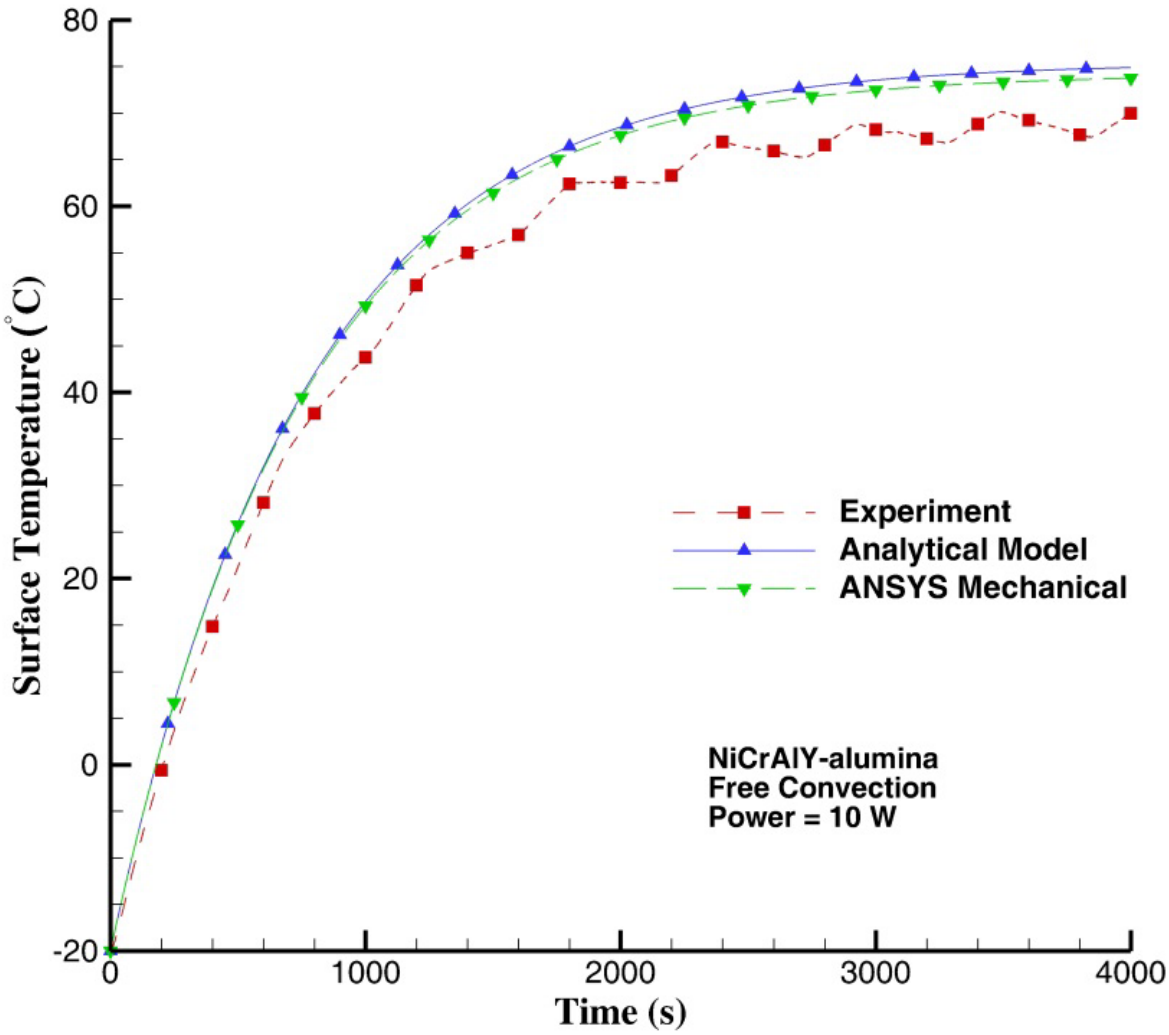

Figure 2-18 A comparison between the experimental data and the results of the mathematical model and ANSYS Mechanical- Free convection

Temperature measurements were also conducted near the edge of the heating elements. These temperatures were slightly lower than measurements conducted at the middle-section. This could be attributed to higher heat transfer rate near the edges due to higher proximity to the sides of the element, and consequently more exposure to the ambient air. Table 2-8 lists the steady state temperatures at two locations on the NiCrAlY-alumina coating along with model

predictions and ANSYS Mechanical results for forced convection. Since the model does not account for convection heat transfer through the sides of the carbon steel substrate, the accuracy of the model in predicting the temperature at the edges is lower than that of the middle section. During the transient heat transfer process, there is considerable temperature variation on the surface.

As demonstrated in Table 2-8, this temperature difference can also be observed for the steady-state condition. The analytical model and the ANSYS simulation were both capable of predicting the surface temperature distribution at every time step. The transient temperature variation at the edges follows the same trend as the middle section. As Figs 2-17 and 2-18 sufficiently describe the variation of surface temperature with time, transient surface temperature variation on the edges has not been presented here. Table 2-9 and Fig 2-19 illustrate additional details about the geometry and applied meshing for the ANSYS Mechanical simulations. Figure 2-20 shows the steady-state temperature distribution of the NiCrAlY-alumina coating using ANSYS Mechanical.

Table 2-8 Steady state temperatures at the middle section and near the edge of NiCrAlY-alumina coating- Forced convection

	Experiments	**Model**	**ANSYS Mechanical**
Temperature at the middle-section [°C]	15.1 ± 0.4 (n = 9)	17.92	16.88
Temperature near the edge [°C]	14.0 ± 0.5 (n = 9)	17.78	15.74

Table 2-9 Detailed information of the ANSYS simulations

Solver	ANSYS Mechanical (Multiphysics)
Time step of the transient solution	1 s
Element type	Solid: Quad 4node 55
Boundary conditions	See Fig. 5
Meshing: Substrate	Quad-mapped (Element edge length = 0.0005 m)
Meshing: Electrical insulation	Quad-mapped (Element edge length = 0.00001 m)
Meshing: Top layer	Quad-mapped (Element edge length = 0.00001 m)

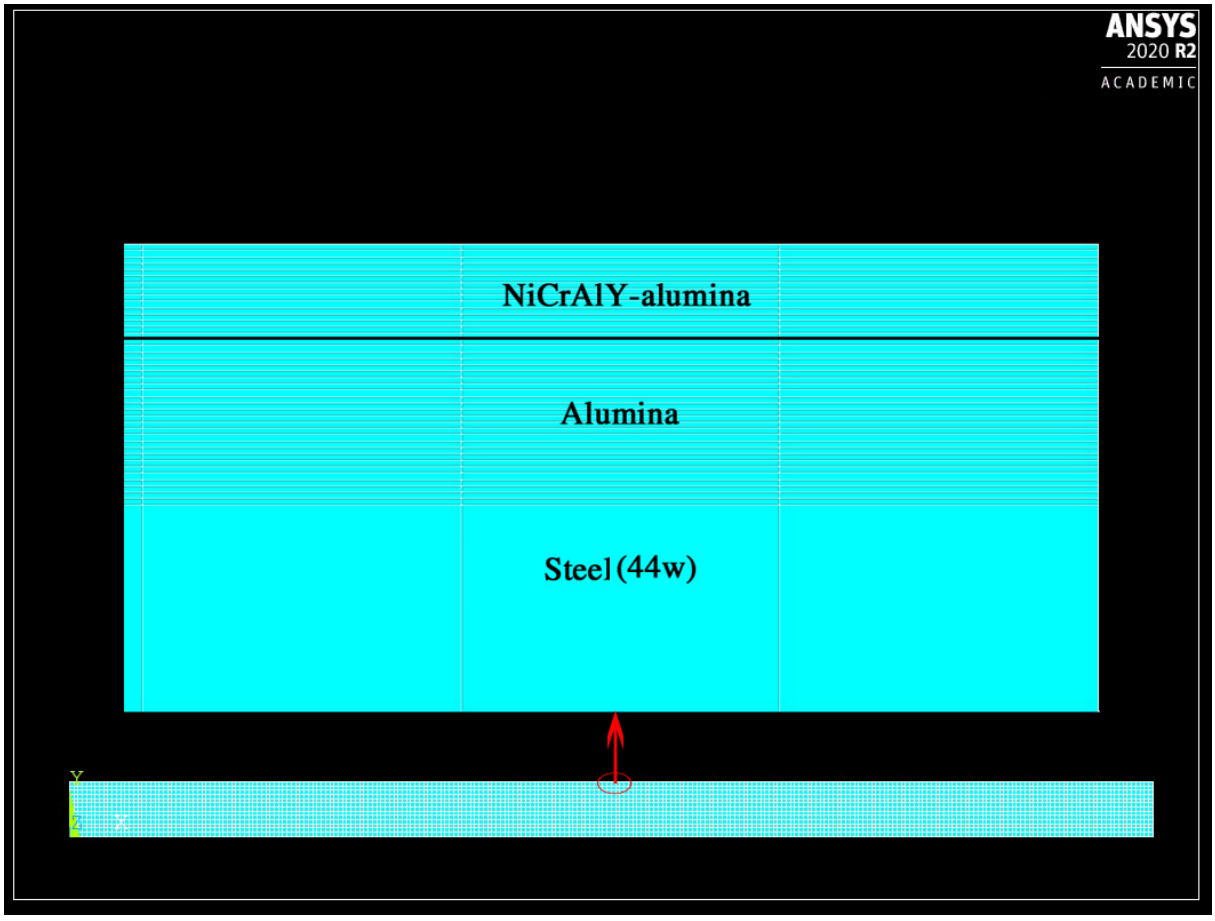

Figure 2-19 Illustration of the generated mesh for ANSYS Mechanical simulation of NiCrAlY-alumina

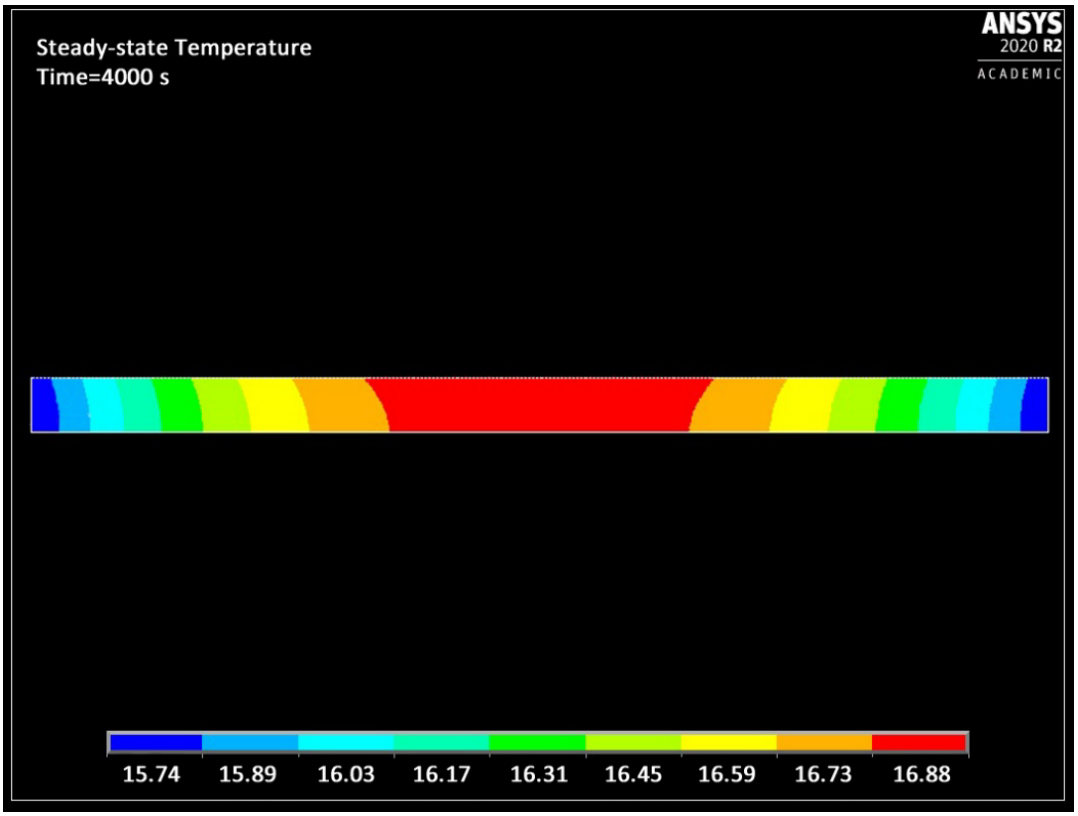

Figure 2-20 Steady-state temperature distribution of the NiCrAlY-alumina coating using ANSYS Mechanical- Forced convection

2.4 Conclusions

In this study, the effect of ceramic particle reinforcement on microstructure, electrical properties and heating performance of thermally sprayed MMC coating-based heating elements was studied. The results suggested that the electrical resistance of MMC heating elements could be adjusted by manipulation of feedstock powder and coating microstructure. It was observed that the electrical properties of the heating elements are significantly affected by that of the ceramic reinforcing phase. A comparative study was conducted in order to examine the ramp-up rate and stead-state temperature under forced and free convection. Coatings with higher electrical resistance exhibited better heating performance.

Given that the amount of supplied power was equal for all the heating systems, it is concluded that certain MMC heating elements could be effectively employed for reduction of requisite energy consumption for de-icing. A two-dimensional analytical transient heat conduction model was developed in order to predict the temperature distribution within the two-layered coating. A similar heat conduction problem was also simulated using the ANSYS Mechanical software.

The results of the model and that of the ANSYS simulations were in good agreement with the experimentally obtained data. Temperature predictions obtained by the analytical model, demonstrated a slight overestimation of the experimental data. The degree of this overestimation was increased for temperatures near the edges of the heating elements. This research clearly shows that the application of thermally sprayed MMC heating elements results in significant improvement of heating performance, efficacy, and functionality of de-icing systems

Nomenclature

A	Equation constant
B	Equation constant
C	Specific heat (J/kg.°K)
h	Convection heat transfer coefficient (W/m^2.°K)
k	Thermal conductivity (W/m.°K)
L	Length (m)
Pr	Prandtl number
Q	Heat (W/m^3)
R	Electrical resistance (Ω)
r	General space coordinate

Ra	Rayleigh number
Re	Reynolds number
T	Temperature (°C)
Greek symbols	
α	Thermal diffusivity (m^2/s)
β	Eigenvalue
δ	Eigenvalue
λ	Eigenvalue
ρ	Density (kg/m^3)
τ	Time-dependent temperature (°C)
Subscripts	
i	Initial
H	Homogeneous
nH	Non-Homogeneous
p	Constant pressure
SS	Steady State
1	Top layer
2	Lower layer

Chapter 3

Evaluation of the Erosive Wear Resistance

In practice, the surfaces of wind turbine blades and aircraft wings would be prone to surface degradation because of erosive wear. The erosion mechanism varies based on the application and the environmental conditions. The particles of dust or hard sand carried by the wind could cause considerable surface degradation, especially at higher linear velocity of the blades. Also, in cold environments the air carries droplets of water which could also result in material removal and damage. These two types of erosion namely, water droplet impact and solid particle impact must be taken into account for designing, material selection, and choosing the coating deposition technique. In this study, after the evaluation of the heating performance of the developed MMC coating-based heating elements, their wear resistance was also studied by examining the performance of the coatings, under the aforementioned erosion types.

Through implementing a metal matrix composite approach, the other objective is to also improve the physical strength of the coatings. For instance, use of the WC-12Co cermet as the reinforcing phase of the NiCrAlY-WC-12Co MMC coating, could potentially enhance the wear resistance of the surface due to its relatively high hardness. The material removal from the surface could result in variation of electrical resistance of the elements and disrupt the desired outcome, which could also cause failure. The electrical failure occurs when the electrical resistance of the elements goes to high due to discontinuity of the conductive layer. For this reason, a number of experiments were also devised in order to assess the erosive wear resistance of the elements while they are in operation.

The work presented in this chapter was published in the proceedings of International Thermal Spray Conference (ITSC-2021), Quebec City, Canada, May 24–27, 2021. The only exception is the parts related to the tests exposing the samples to erosive wear while heating.

3.1 Experimental Method

3.1.1 Substrate Preparation and Coating Deposition

An oxy-acetylene flame spray torch (6PII, Oerlikon Metco, Westbury, NY, USA) was employed in order to deposit the coatings onto low carbon steel (44W) identical round bars (outer diameter = 19.05 mm, length = 76.20 mm). Prior to coating fabrication, the specimens were grit blasted with #24 (~686 μm) alumina grit (Manus Abrasive Systems Inc., Edmonton, AB, Canada). With argon as the propeller gas, powders were fed into the torch using a volumetric powder feeder (5MPE, Sulzer Metco, Westbury, NY, USA). Due to the comparative nature of this study, and given that no heating tests were conducted, the coatings were not deposited on top of an electrical insulation layer such as zirconia or alumina.

Powders were prepared by mechanical blending of NiCrAlY (AMDRY 964, Oerlikon Metco, Westbury, NY, USA) as the metal matrix, with WC-12Co (Metco 72F-NS, Oerlikon Metco, Westbury, NY, USA), alumina (Al_2O_3, AMDRY 6060, Oerlikon Metco, Westbury, NY, USA), and titania (TiO_2, Metco 102, Oerlikon Metco, Westbury, NY, USA). For each MMC feedstock powder, identical spraying parameters were employed with 40 wt. % of the cermet or ceramic in the final mixture. For all the samples, 8 passes of coating deposition were done provided that the angular velocity was 600 rpm. A number of samples were also deposited with pure NiCrAlY to serve as a base for comparison. In order to maximize consistency, a robot (HP-

20, Motoman, Yaskawa Electric Corp., Waukegan, IL, USA) was programmed for moving the flame spray torch. Table 3-1 lists the spraying parameters.

Table 3-1 Spraying parameters for NiCrAlY (N1), NiCrAlY-WC-12Co (N2), NiCrAlY-Al_2O_3 (N3), NiCrAlY-TiO_2 (N4)

Parameter	**N1**	**N2**	**N3**	**N4**
Stand-off distance [mm]	177.8	165.1	165.1	165.1
Torch velocity [mm/s]	12	10	11	11
Acetylene flow [NLPM]	19	23	23	21
Oxygen flow [NLPM]	30	32	32	30
Angular velocity [rpm]	600	600	600	600
Argon flow rate [m^3/h]	0.56	0.56	0.56	0.56
Powder flow rate [FMR]	80	80	80	80
Passes of deposition	8	8	8	8

Figure 3-1 shows the high magnification secondary electron images of the applied alumina powder and the NiCrAlY-WC-12Co mixture, in which the morphology of the powders is demonstrated. These images were captured by using a scanning electron microscope (Zeiss Sigma 300 VP-FE, Carl Zeiss Canada Ltd., Toronto, ON, Canada). The flame spraying torch and the cylindrical specimen are shown in Fig 3-2 during coating deposition.

(a) [75]

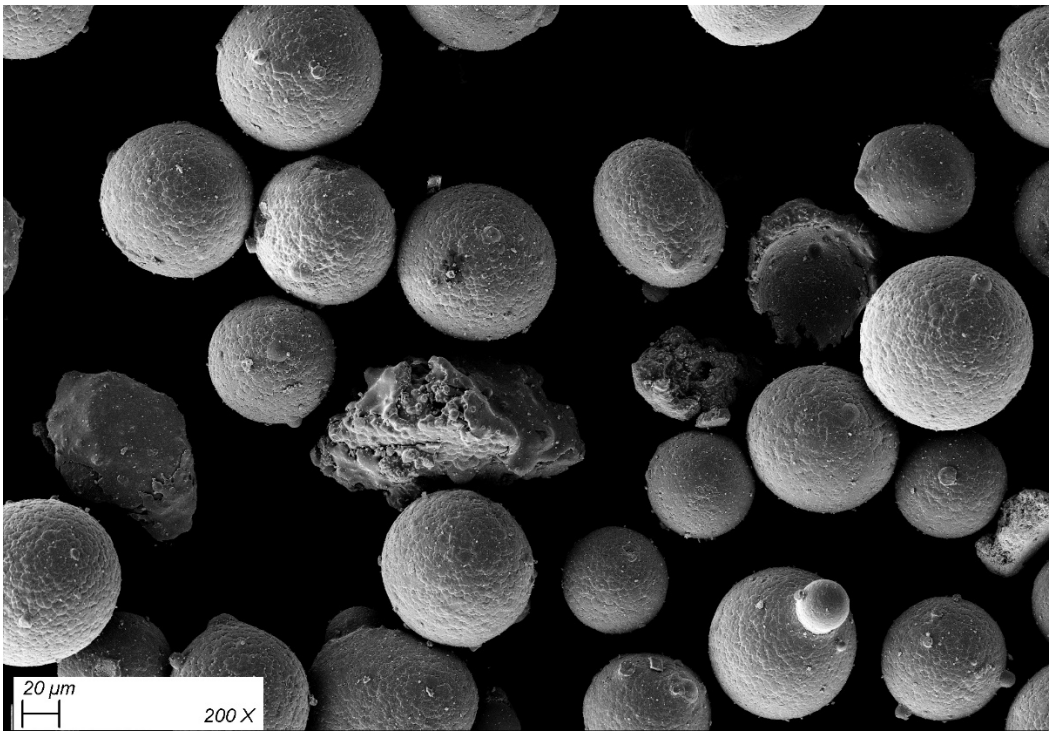

(b)

Figure 3-1 a) Secondary electron image of alumina Amdry 6060 powders [75], b) Secondary electron image of NiCrAlY-WC-12Co feedstock powder

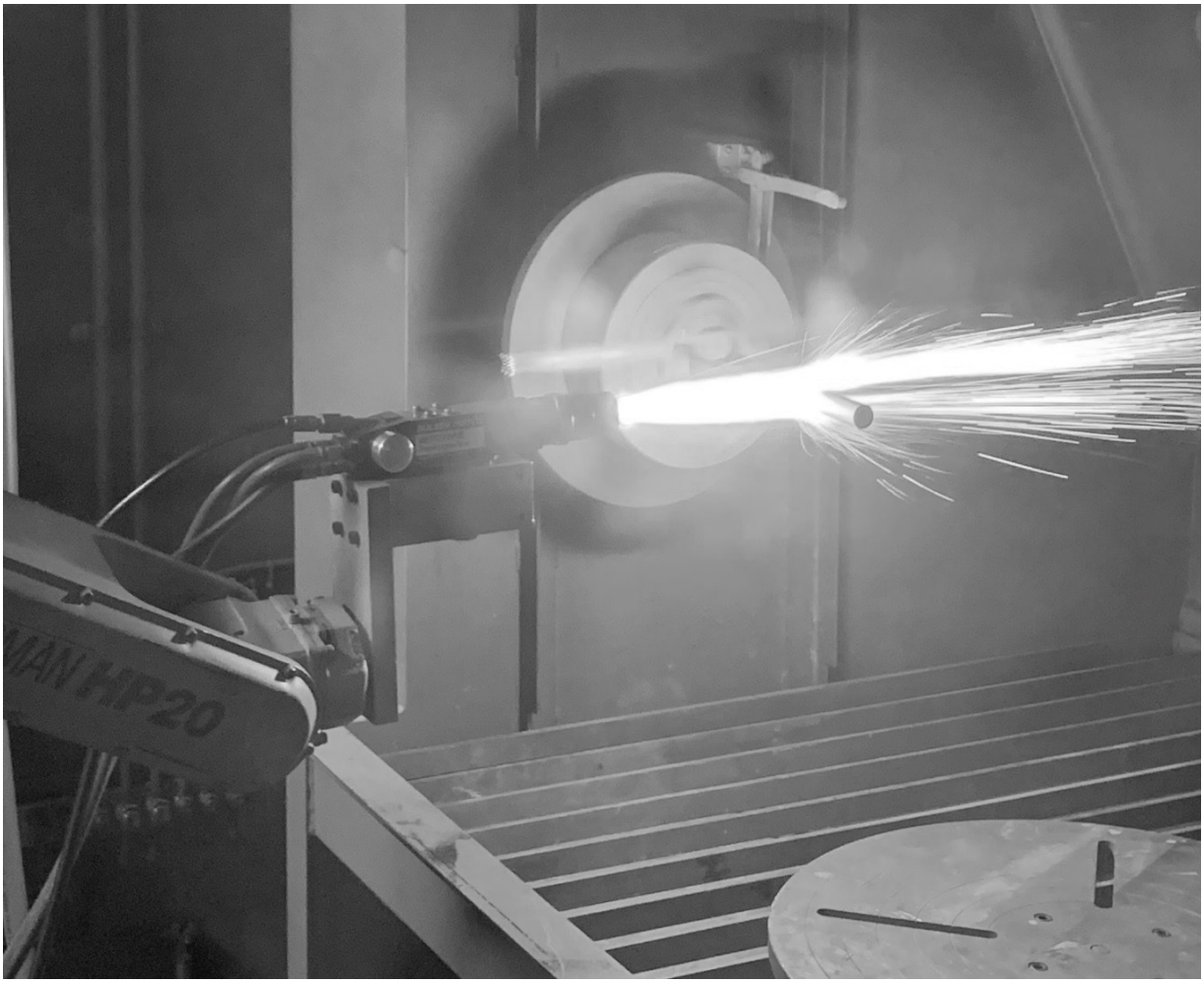

Figure 3-2 Coating deposition on cylindrical samples using a flame spraying torch

3.1.2 Coating Characterization

For microstructural analysis, the same method and equipment as Section 2.1.5 were used. These images were then analyzed using an image analysis software (ImagePro, Media Cybernetics, Bethesda, MD, USA) in order to calculate thickness, volumetric percentage of phases, and porosity. The Vickers hardness of the surfaces of the coatings was measured under 1 kgf (Wilson VH1202, Instron, Norwood, MA, USA) based on the ASTM-E384 standard. Prior to the hardness measurements, all the surfaces were ground using 240, 400, 600, 800, and 1200 silicon carbide grit papers (LECO, Mississauga, ON, Canada).

3.1.3 Water Droplet Impact Erosion

The water droplet erosion tests were conducted in a closed-loop high-speed wind tunnel. As shown in Fig 3-3, the sample was positioned vertically in the middle of a square-shaped test section with a 0.2 m × 0.2 m cross section. Fan frequency was fixed at 46.0 Hz for all the WDE experiments which provided an air velocity of approximately 60 m/s at the test section. An air atomizing spray nozzle was employed in order to generate water droplets and inject them into the air stream. The water and air pressure of the droplet generator system were 275.8 kPa (40 psig) and 68.9 kPa (10 psig), respectively. For all the tests, the mass flow rate of the consumed water was 0.024 m^3/h (6.4 gal/h).

With these parameters fixed, the system was calibrated to deliver an average water droplet size of 40 μm and liquid water content between 1.5 and 2.0 g/m^3. The duration of the tests for all the specimens was set to 45 minutes. A weighing balance (Acculab ATL423-I, Acculab, NY, USA), with readability and precision of 1 mg was used to measure the mass of the samples before and after the WDE tests. For each powder, the tests were conducted on three different samples. A confocal microscope (OLS40-CB, Olympus Corporation, Tokyo, Japan) was used in order to assess the effect of water droplet impingement on certain surface roughness parameters.

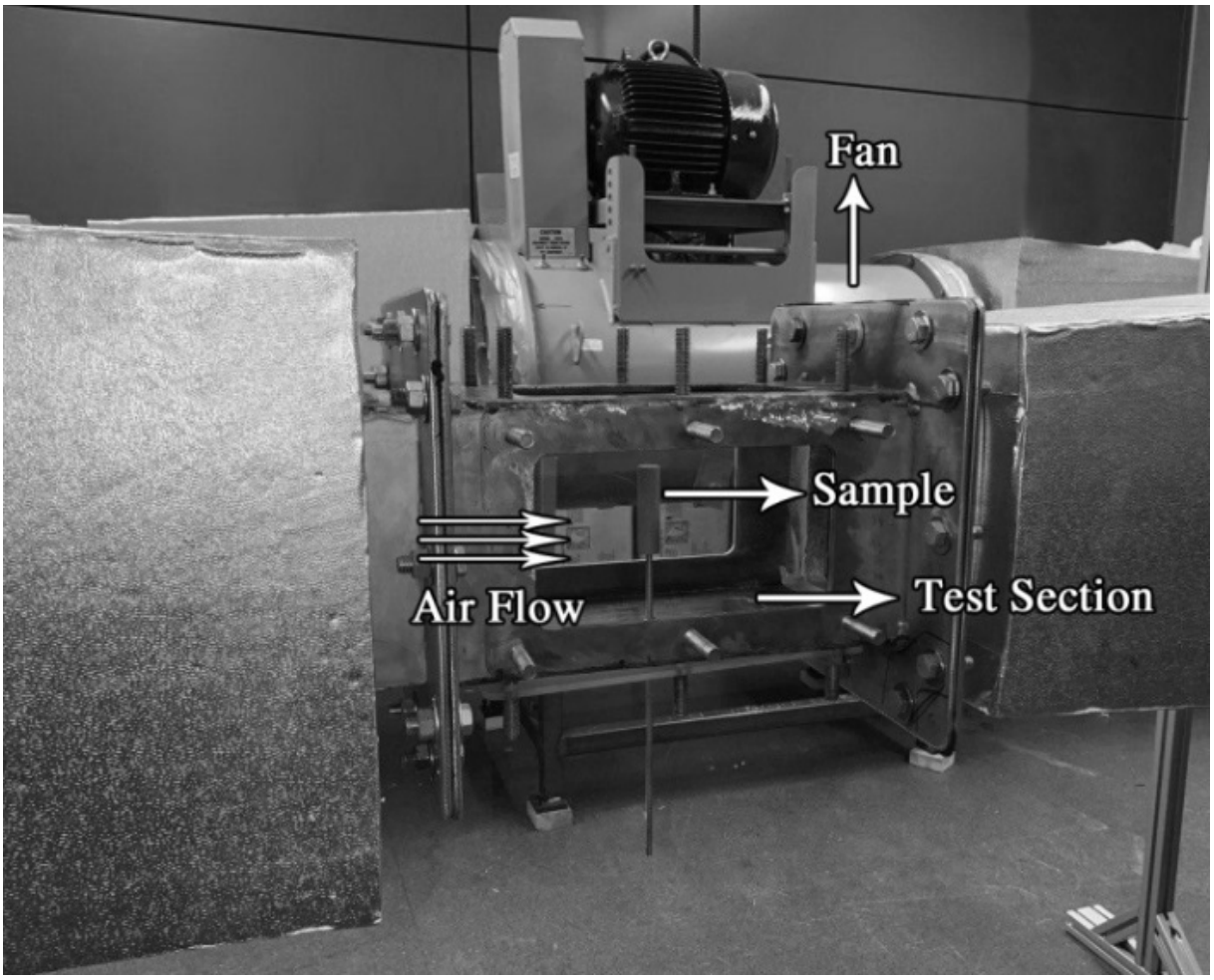

Figure 3-3 WDE testing apparatus in the high-speed wind tunnel at Concordia University.

3.1.4 Solid Particle Impact Erosion tests

In order to evaluate the dry erosion resistance of the fabricated coatings, a modified version of the ASTM G76 [59] standard test was implemented. Figure 3-4 shows the solid particle impact test assembly which is partly similar to the experimental apparatus used by Ashrafizadeh *et al.* [58]. A cold spray unit (SST Series P, CenterLine Ltd., Windsor, ON, Canada) was employed for accelerating the erodant garnet sand particles (Grade C- Super Garnet, V.V. Mineral, Tamil Nadu, India) towards the specimens. Table 3-2 lists the primary

operating parameters of the cold spray unit for the dry erosion tests. Compressed air was used as the medium for propelling the sand particles.

All the coatings were tested under controlled identical conditions and were subjected to 45 seconds of solid particle impingement. An analytical balance (Sartorius™ ENTRIS224I1SUS, Sartorius, Goettingen, Germany) was used to measure the amount of mass loss. The readability and precision of this balance had the same value of 0.1 mg. The temperature of the compressed air was set at 25 °C. A stereo microscope (Stereo Discovery.V8, Carl Zeiss Microscopy GmbH, Jena, Germany) was employed to study the extent of surface degradation in the coating.

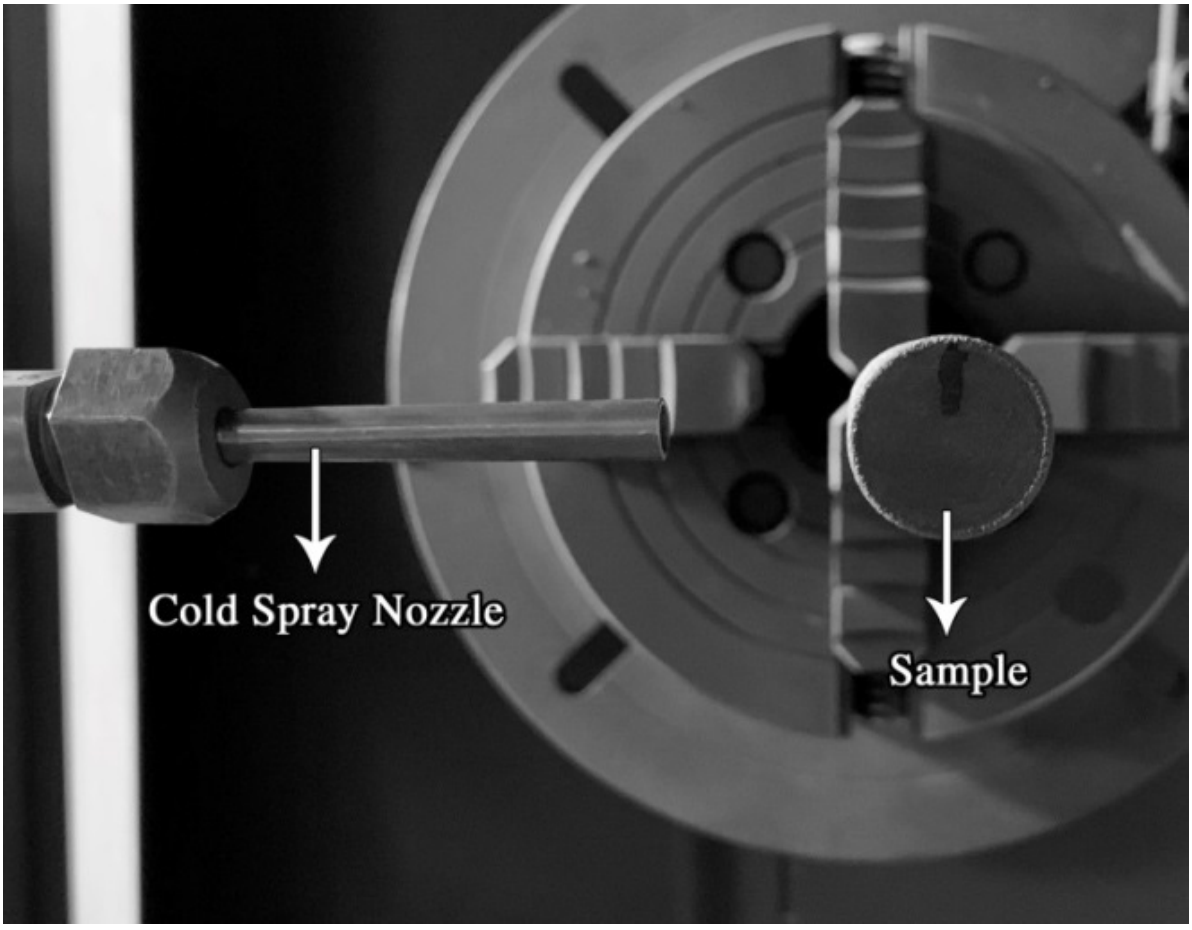

Figure 3-4 Solid particle impact test assembly.

Table 3-2 Operating parameters of the cold spray unit for the dry erosion tests

Nozzle length [mm]	70
Stand-off distance [mm]	22
Nozzle throat diameter [mm]	2.5
Nozzle output diameter [mm]	5.4
Pressure of compressed air [kPa]	435

3.1.5 Solid Particle Impact During the Heating

The erosion resistance of thermally sprayed heating elements was evaluated while operating. As shown in Fig 3-5, a cold spray nozzle were used in order to imping erodent particles upon the coating surface. The surface of the specimen was heated by applying electrical voltage through the Joule heating principle. A temperature controller and a data acquisition system were employed in order to adjust and monitor the coating surface temperature. Before the erosion tests, all the coating surfaces were heated to reach a specific setpoint temperature identical for all the samples. The heating elements were then subject to solid particle impact erosion and the experiments will continue until they reach the failure point. This failure point is defined as the moment the electrical current goes to zero and the heating element loses its functionality. During the experiments, real-time temperature (at the surface and back of the sample), voltage, and electrical current are recorded. Average mass loss per unit time were evaluated as a key measure in assessing wear rate. Through measuring the electrical current and voltage, the real-time electrical resistance can be measured. The relation between the coating surface temperature and electrical resistance is also studied. In addition, the effect of sample

wear rate on heating performance and electrical resistance is investigated. Since the time period for these experiments is short, the flowrate of the erodent particles is decreased to have better control. The temperature was monitored in order to assess the effect of gas jet impingement on the surface temperature and the convective heat transfer rate. For the protection of the cold sprayed electrical copper terminals, they are covered with thermal spray tape. Garnet sand (Grade C- Super Garnet, V.V. Mineral, Tamil Nadu, India) is used as he erodent material.

The experimental results were be used in order to conduct a comparative analysis on the wear performance of the MMC heating elements that were previously developed. The combined application of resistive heating and dry erosion could be used to predict the behavior of the MMC heating elements under real operational conditions. The testing parameters are outlined in Table 3-3, while the rest of the cold spray parameters are listed in Table 3-2.

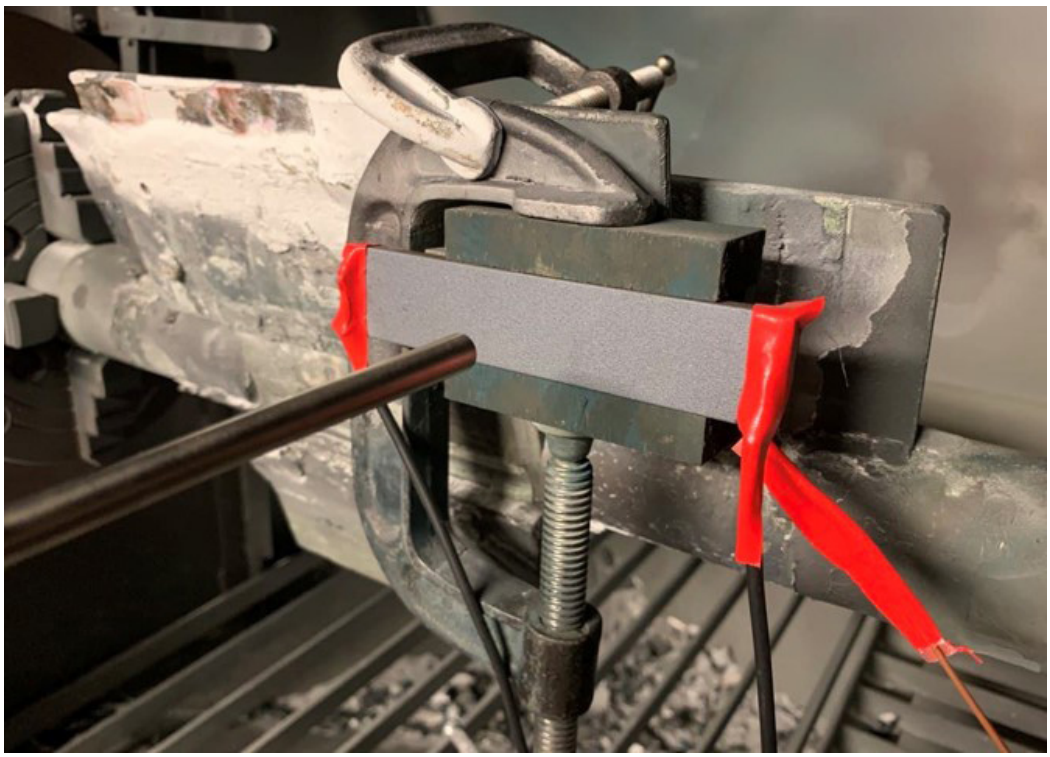

Figure 3-5 Testing apparatus of the dry erosion testing while heating

Table 3-3 Operating parameters of dry erosion tests while heating

Gravitational powder feed rate [%]	5
Air jet temperature [°C]	25
Increment [mm]	3
Torch velocity [mm/s]	300

3.2 Results and Discussion

3.2.1 Coating Characterization

Figure 3-6 shows the secondary electron image of all the coatings. It is observed that most NiCrAlY particles are fully melted. All the MMC coatings appear to have good adhesion to the carbon steel substrate as there are no visible gaps at the coating-substrate interface. Since the melting point of tungsten carbide is considerably higher than that of other powders, the spraying parameters were adjusted in order to compensate for the higher melting point. The average porosity, thickness, and weighted percentage of the different MMC phases are listed in Table 3-4. The porosity of the NiCrAlY-WC-12Co coating is slightly higher than that of the NiCrAlY-alumina coating. However, as demonstrated in Fig 3-6, more discontinuities are observed within the NiCrAlY-alumina MMC. This could be attributed to the cobalt particles which can contribute to an enhanced binding between the cermet and the metal matrix.

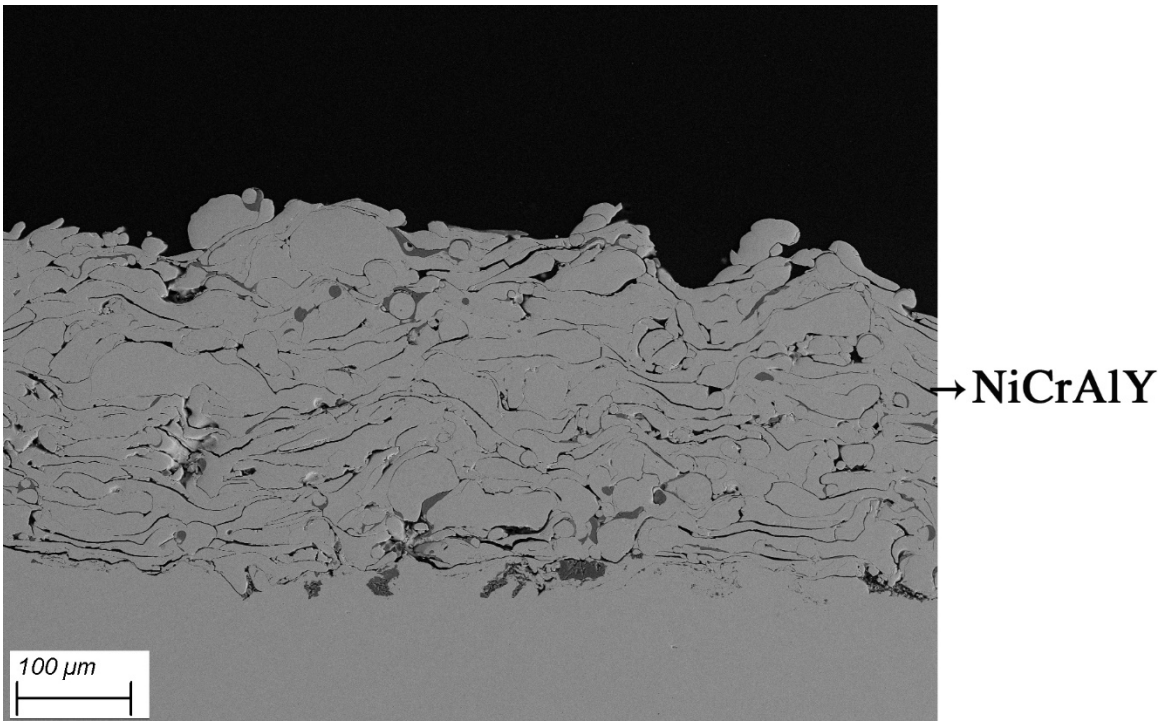

(a)

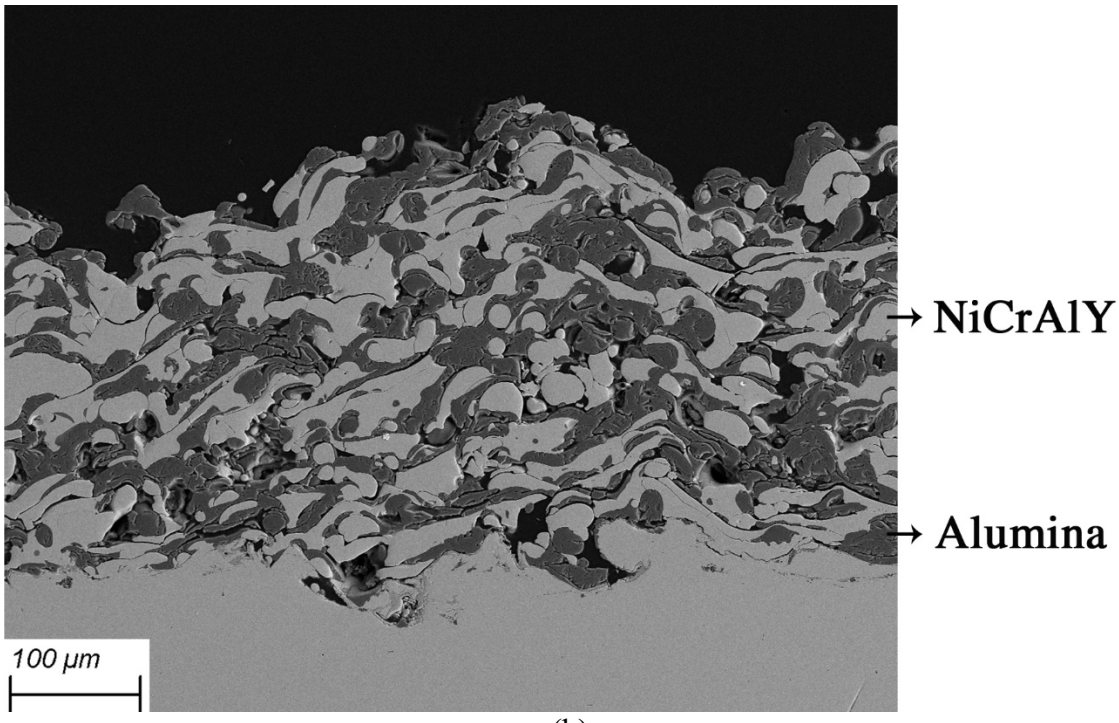

(b)

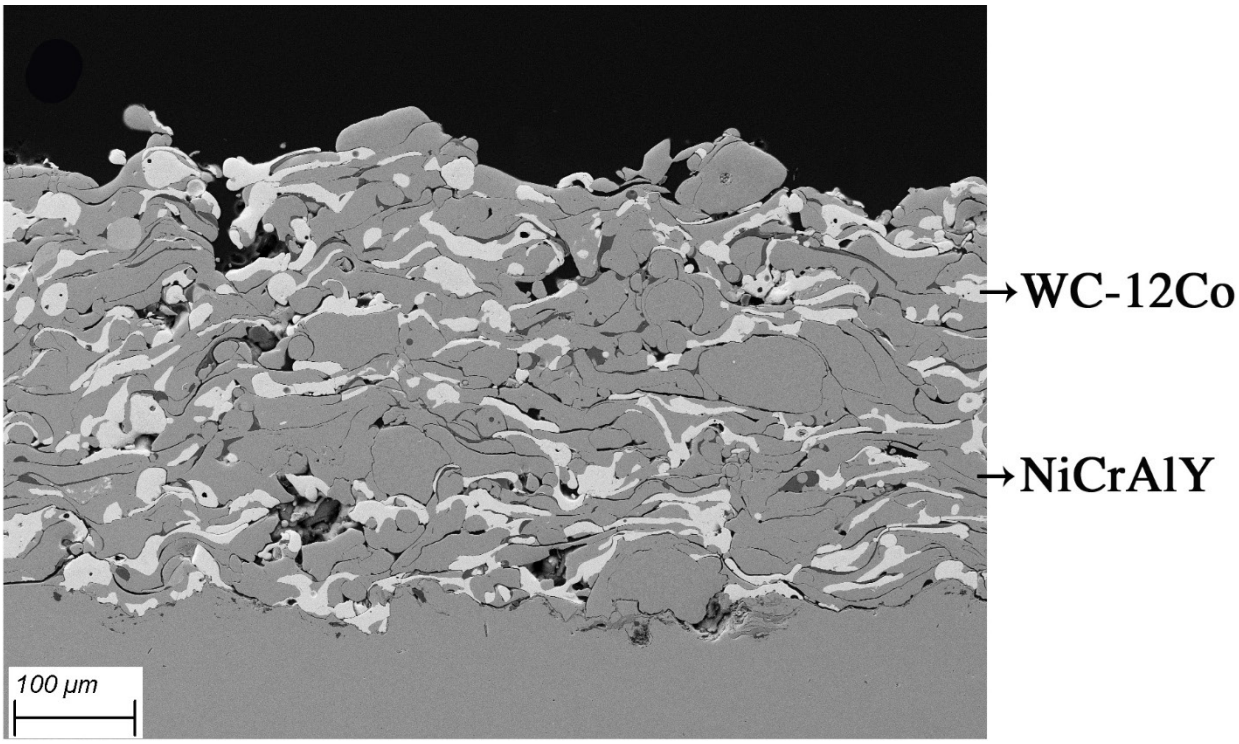

(c)

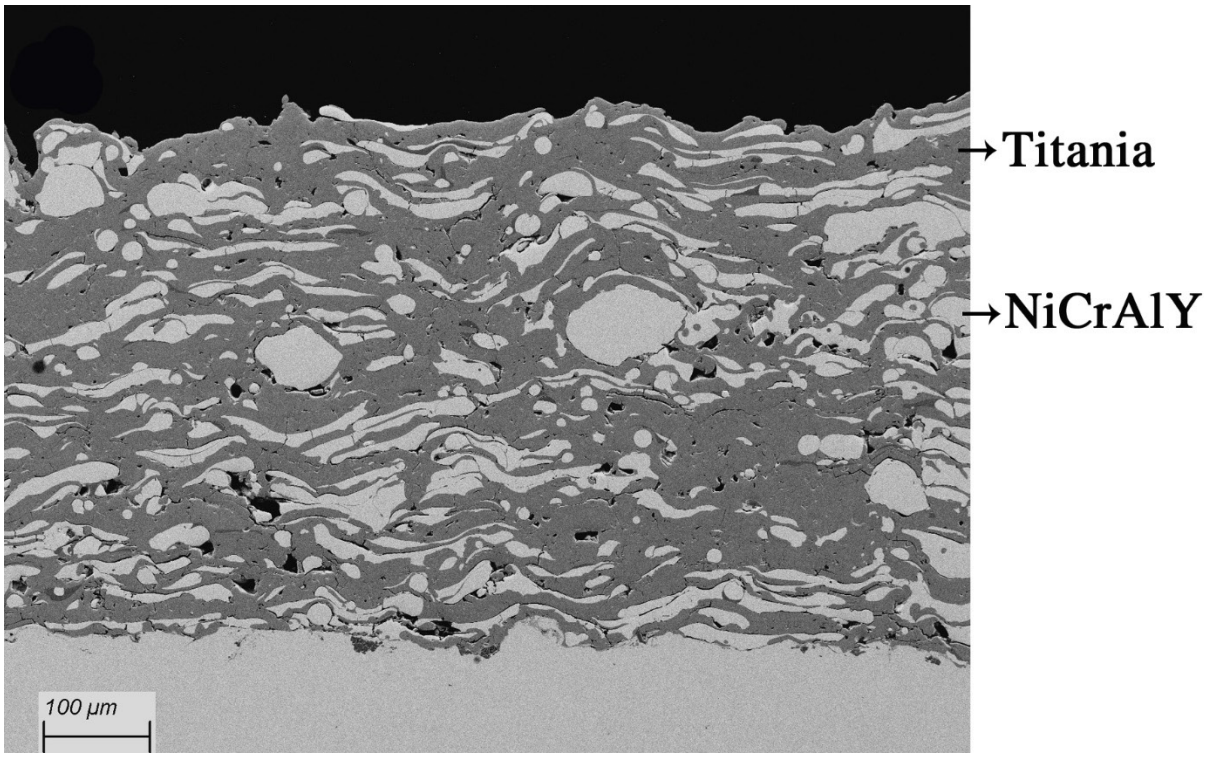

(d)

Figure 3-6 Secondary electron image of the microstructure of the coatings.

Table 3-4 Average porosity, thickness, and weighted percentage of the matrix and reinforcing phases for NiCrAlY (N1), NiCrAlY-WC-12Co (N2), NiCrAlY-Al_2O_3 (N3), NiCrAlY-TiO_2 (N4).

Coating	**N1**	**N2**	**N3**	**N4**
Porosity [%]	4.5	7.6	6.1	2.7
Thickness [μm]	294	364	287	465
Matrix phase [wt. %]	-	62.7	70.6	53.9
Reinforcing phase [wt. %]	-	37.3	29.4	46.1

As listed in Table 3-4, the lowest porosity is observed in the NiCrAlY-titania coating. TiO_2 has the lowest melting point and that could be the primary reason for its relatively lower porosity and more uniform distribution of the reinforcing phase within the matrix. Table 3-5 lists the average measured hardness for all the coatings. Since tungsten carbide has considerably higher hardness compared to other deposited ceramics, it is expected that the NiCrAlY-WC-12Co coating would exhibit the highest hardness. It should be noted that the distribution of the ceramic within the matrix is not exactly uniform. As a result, depending on the location of the indent, the reported hardness value may appreciably differ for the same surface. Given that the pure NiCrAlY coating has the most uniform surface in terms of material, standard deviation of its hardness measurements is the lowest.

Table 3-5 Average Vickers hardness (ASTM-E384) measured under 1 kgf.

Coating	Hardness (HV)
NiCrAlY	442 ± 11 (n = 12)
NiCrAlY-WC-12Co	834 ± 34 (n = 12)
NiCrAlY-Al2O_3	537 ± 27 (n = 12)
NiCrAlY-TiO_2	622 ± 31 (n = 12)

3.2.2 Water Droplet Impact Erosion

Similar to the dry erosion tests, mass loss was chosen as the proxy indicator of the degree of erosion in the fabricated coatings during WDE tests. Table 3-6 shows the amount of mass loss and the calculated standard deviations for all the coatings. It should be noted that no visible damage was detected in any of the samples. As illustrated in Table 3-6, appreciable difference was observed in the mass loss of the specimens. The impinging water droplet impact velocity of 60 m/s is close to the range of 70-150 m/s observed in wind turbine blades [53, 82]. The impact of water droplet on a solid surface occurs with a specific sequence, which includes four consecutive stages. These stages are: (1) impact moment, (2) hammer pressure, (3) stress waves, and (4) lateral jetting [83].

An important factor that contributes to the complexity of WDE tests is the varying erosion rate during the tests. The mass removal process does not occur instantly after the droplet impingement begins. Usually, the erosion process goes through an incubation period at the beginning, with negligible mass removal. However, surface parameters such as roughness vary

considerably during the incubation period. After this period, the surface usually goes through successive periods of increasing, constant, and then decreasing erosion rates [84].

Judging based on the mass loss reported in Table 3-6, all the coatings have passed the incubation period and entered into the mass removal stage. The NiCrAlY-WC-12Co coating has the lowest erosion rate. This could be attributed to the desirable mechanical properties of tungsten carbide and its well-stablished performance in wear resistance [36]. Among the MMC coatings, the NiCrAlY-alumina coating has the highest amount of mass loss. This is likely because of the discontinuities observed in Fig 3-6b. It is very crucial to note that all the MMC coatings have demonstrated a lower amount of mass loss caused by the WDE tests, compared to the pure NiCrAlY coating. The low porosity of NiCrAlY-titania coating could be a cause of low water droplet penetration, and satisfactory erosion performance. In addition, the NiCrAlY-titania coating is relatively more homogeneous than the other MMC coatings and exhibits little discontinuity. Microstructural discontinuities can interact with stress waves caused by droplet impact, which results in stress concentration and consequently formation of high tensile stress [85, 86]. Accordingly, in the NiCrAlY-titania coating, tensile stress concentration due to droplet impact is expected to be relatively low.

Table 3-6 The average amount of mass loss after 45 minutes of WDE testing.

Coating	**Mass loss (g)**
NiCrAlY	0.009 ± 0.001 ($n = 3$)
NiCrAlY-WC-12Co	0.001 ± 0.001 ($n = 3$)
NiCrAlY-alumina	0.008 ± 0.001 ($n = 3$)
NiCrAlY-titania	0.004 ± 0.001 ($n = 3$)

A confocal microscope was used to compare the effects of WDE on the surface topography of the coatings. This type of analysis is focused on the amount of variation in certain surface parameters. Table 3-7 lists the values of two different surface parameters before the WDE tests. R_a is the arithmetic average height parameter, i.e., the average roughness of the surface. This parameter, also known as center line average (CLA), is the most utilized roughness parameter in surface analysis, and is not very sensitive to small changes in the surface profile [87]. Kurtosis (R_{ku}) is the fourth central moment of surface amplitude probability density function and represents the sharpness of the surface height profile across the assessment length [87]. Table 3-8 shows the variation percentage of R_{ku} before and after the WDE experiments. Figure 3-7 shows the height profiles of the surfaces before and after the WDE tests.

R_{ku} represents the degree of bluntness or pointedness of the surface asperities [88, 89]. Values of kurtosis less than 3 means that the height distribution curve of the surface has relatively few low valleys and high peaks, i.e., it is platykurtoic. If the kurtosis is larger than 3, the surface would be leptokurtoic, meaning that it has relatively large number of high peaks and low valleys. The results of confocal microscopy clearly demonstrate that all the coatings under study are leptokurtoic. Furthermore, it is evident that all of the coatings have maintained their leptokurtoic profiles during the WDE tests. The NiCrAlY-titania and NiCrAlY-WC-12Co MMC coatings had the lowest amount of variation in kurtosis. For the NiCrAlY-titania coating, this can be attributed to the relatively low degree of initial surface height unevenness as shown in the micrographs. In addition, the NiCrAlY-titania coating has a more homogeneous microstructure and the lowest porosity. In contrast, the NiCrAlY and NiCrAlY-alumina coatings exhibit relatively higher kurtosis variation, which could be partly due to the initial non-uniformity of the surface profile and higher porosity.

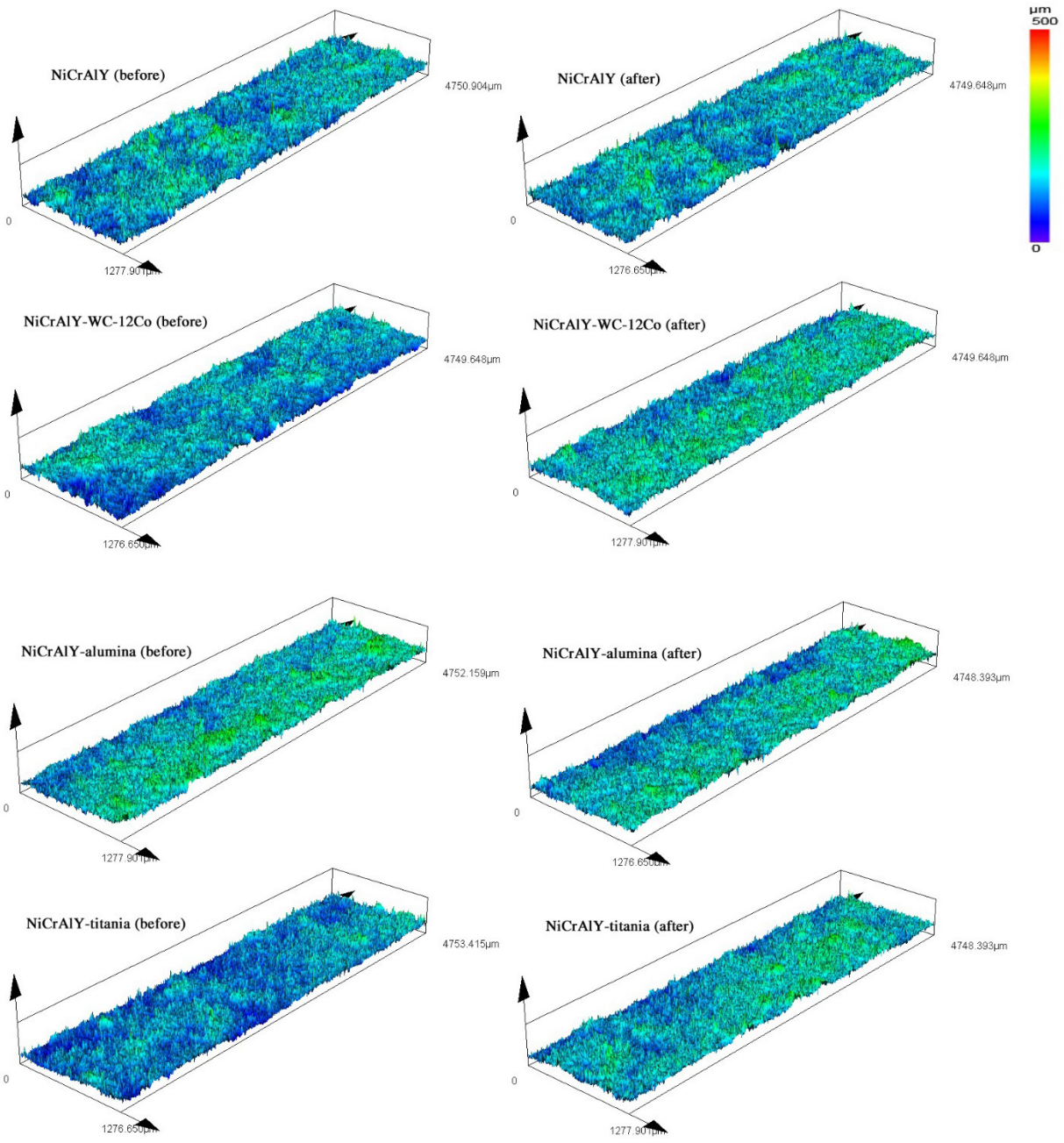

Figure 3-7 Height profiles of the surfaces before and after the WDE tests

It can be seen that the MMC coatings with a lower amount of mass loss exhibit a lower kurtosis variation. This correlation contributes to the claim that the NiCrAlY-WC-12Co and NiCrAlY-titania coatings have relatively higher wear resistance. As the kurtosis value becomes

larger, the surface develops a rougher profile with a relatively higher degree of pointedness [88, 90]. Based on the variations of the kurtosis values, the NiCrAlY and NiCrAlY-alumina MMC coatings have transitioned towards rougher surface profiles with a relatively higher rate during the WDE tests.

Table 3-7 Values of average roughness (R_a), and kurtosis (R_{ku}) before the WDE tests.

Coating	$\boldsymbol{R_a}$ **(μm)**	$\boldsymbol{R_{ku}}$
NiCrAlY	24.3	3.84
NiCrAlY-WC-12Co	26.5	4.11
NiCrAlY-alumina	28.7	4.45
NiCrAlY-titania	19.6	2.87

Table 3-8 Variation percentage of kurtosis before and after the WDE experiments.

Coating	$\boldsymbol{\Delta R_{ku}}$ **(%)**
NiCrAlY	16.3
NiCrAlY-WC-12Co	7.5
NiCrAlY-alumina	14.9
NiCrAlY-titania	8.4

3.2.3 Solid Particle Impact Erosion

Mass loss was considered as the key criteria in determining the erosive wear resistant of the coatings. The amounts of mass loss and the calculated standard deviations are listed in Table 3-9. These amounts are averaged across four experimentally obtained values for each coating. Significant difference was observed in wear resistance of the coatings under study. It is evident that the NiCrAlY-WC-12Co and NiCrAlY-titania coatings have the highest wear resistance in terms of mass loss. In MMC coatings, the particles of the reinforcing phase could serve as obstacles against the erosive sand particles, provided that they have sufficient hardness values [38]. These reinforcing ceramic particles could potentially deflect the erodant particles and mitigate surface degradation [38, 56].

Table 3-9 The average amount of mass loss after 45 seconds of solid particle impact.

Coating	Mass loss (g)
NiCrAlY	0.1258 ± 0.0131 ($n = 4$)
NiCrAlY-WC-12Co	0.0605 ± 0.0047 ($n = 4$)
NiCrAlY-alumina	0.1148 ± 0.0087 ($n = 4$)
NiCrAlY-titania	0.0754 ± 0.0066 ($n = 4$)

Hardness has a substantive impact on the wear performance of thermally sprayed coatings [57]. Accordingly, the higher wear resistance of the NiCrAlY-WC-12Co coating could be attributed to its relatively higher hardness. Porosity can also affect the wear performance of materials under solid particle impingement [91]. The relatively low amount of mass loss in the NiCrAlY-titania coating could be likely due to its relatively lower porosity and consequently less

surface penetration. Figure 3-8 shows the surface topography of different coatings after the dry erosion experiments.

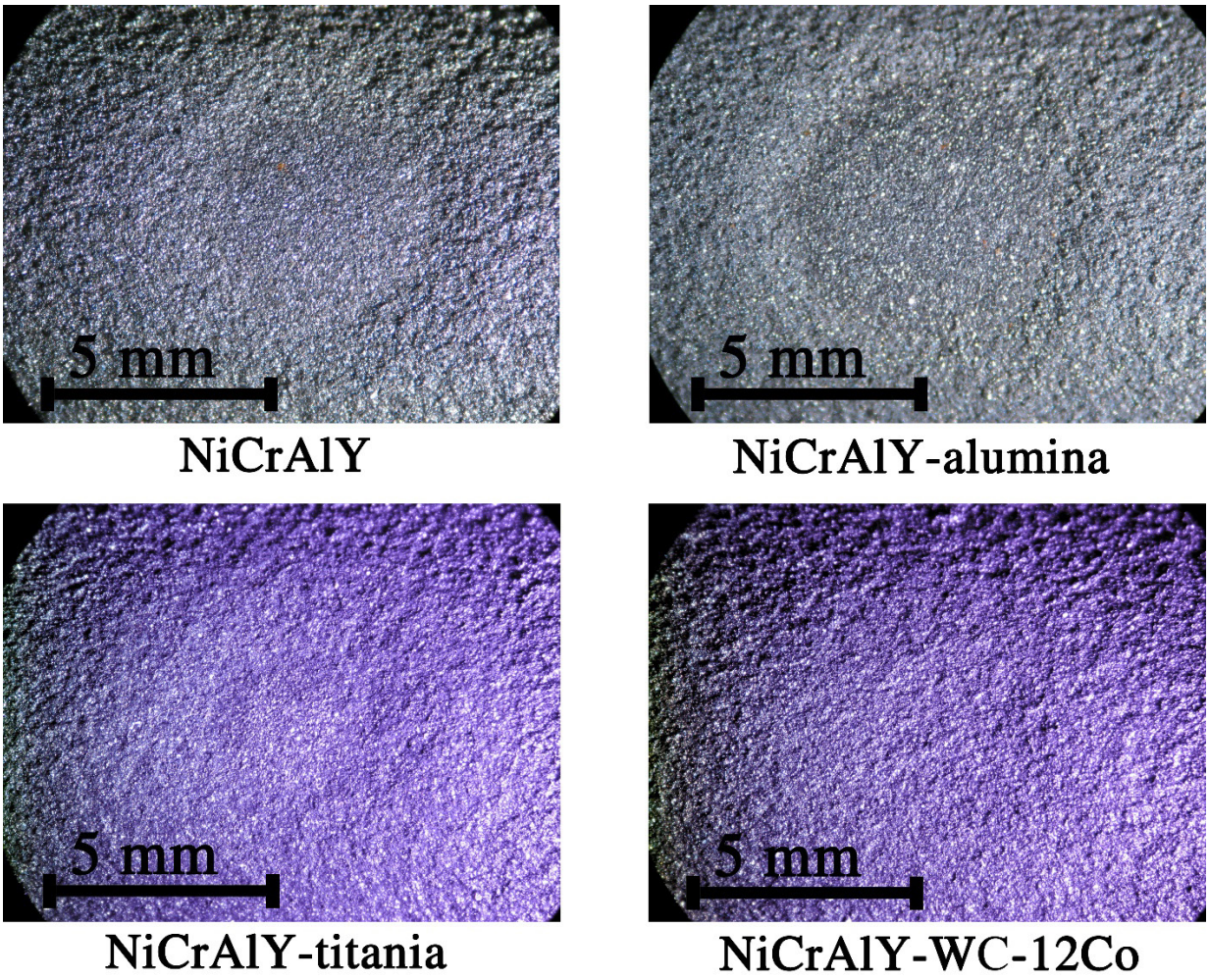

Figure 3-8 Topographical images of the eroded coating surfaces captured by a stereo microscope.

It can be observed that the eroded areas in the NiCrAlY and NiCrAlY-alumina coatings have a highly visible circular geometry, with the NiCrAlY-alumina coating having slightly larger radius. However, the eroded areas of the NiCrAlY-WC-12Co and NiCrAlY-titania coatings have

undergone considerably less surface degradation. The significantly better wear performance of the NiCrAlY-WC-12Co coating could be due to the well-established effect of tungsten carbide particles in improving the mechanical properties of thermally sprayed coatings [34].

3.2.4 Solid Particle Impact During the Heating

In order to examine the functionality of the coating-based resistive coatings, they should be tested under more realistic operational conditions. During the impingement of erodent garnet sand particles, the thickness of the coating decreases simultaneously. This would result in a significant increase in electrical resistance and might even lead to electrical failure. The testing parameters were chosen so that all the materials go through material removal and thickness reduction. In the case of electrical failure, the heating element loses its capability as an electrically conductive material. This type of failure either occurs due to localized generated cracks and asperities, or it occurs when the thickness drops to a point that results in a very high electrical resistance.

During these tests, the initially applied power is identical for all the heating elements. For this reason, the applied voltage is calculated based on the initial electrical resistance. In order to evaluate the extent to which these MMC coatings could maintain their functionality. Moreover, it is also interesting to observe the degree to which the performance and functionality deviates from heating without simultaneous material removal. By maintaining the voltage constant for each element during the tests, the real-time variation in the electrical current could be observed. Thus, the real-time variation in electrical resistance could be monitored. Figure 3-9 demonstrates the variation of the electrical current over time. Three samples were tested for each material.

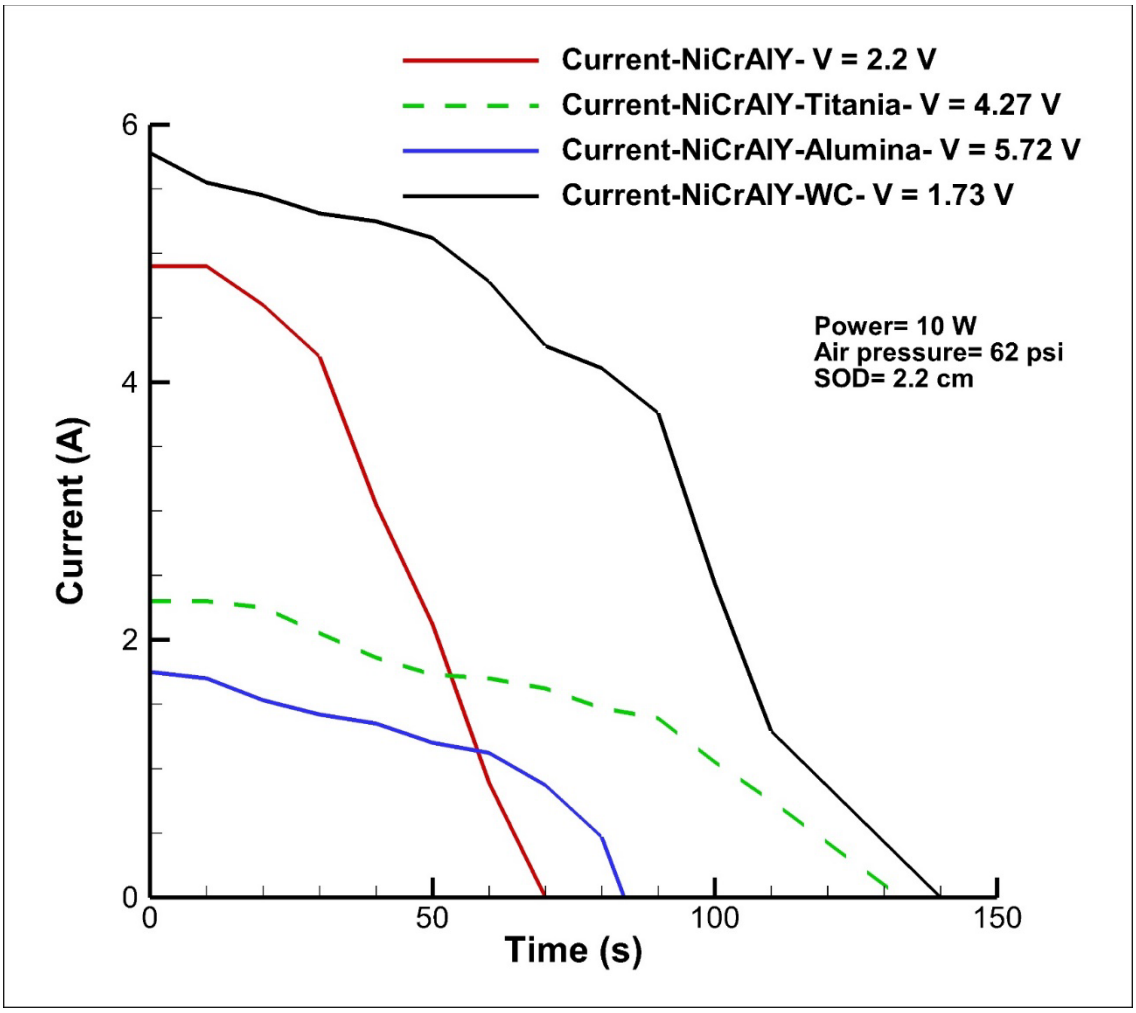

Figure 3-9 Variation of the electrical current over time

It is observed that upon the start of the test, the electrical current begins to drop due to the continuous reduction of electrical resistance. As observed in Fig 3-9, all the experiments were allowed to continue until the point of failure, in which the electrical current becomes zero and the heating capability would be lost. There are a number of observations to be made here. The most significant observation is that the materials with higher erosive wear resistance (as discussed in Secs 3.2.2 and 3.2.3) could function for appreciably larger periods of time. It could also be observed that all the MMCs performed better than the pure NiCrAlY coating.

It could be seen that the slope of electrical current curves differs for different materials. The current for NiCrAlY-titania and NiCrAl-alumina is reduced with a lower rate than NiCrAlY- and NiCrAlY-WC-12Co. It is generally expected that the rate of current reduction would be lower for materials with higher wear resistance. In this particular case, owing to the appreciably lower electrical resistance of NiCrAlY and NiCrAlY-WC-12Co, the initial value of electrical current for these materials is evidently higher. Considering the fact that all the currents drop to zero, the average slope would be higher. Figure 3-10 shows the plot of real-time electrical resistance versus real-time temperature. In order to better observe the performance of the NiCrAlY-WC-12Co, it is plotted with high magnification and is shown in Fig 3-11.

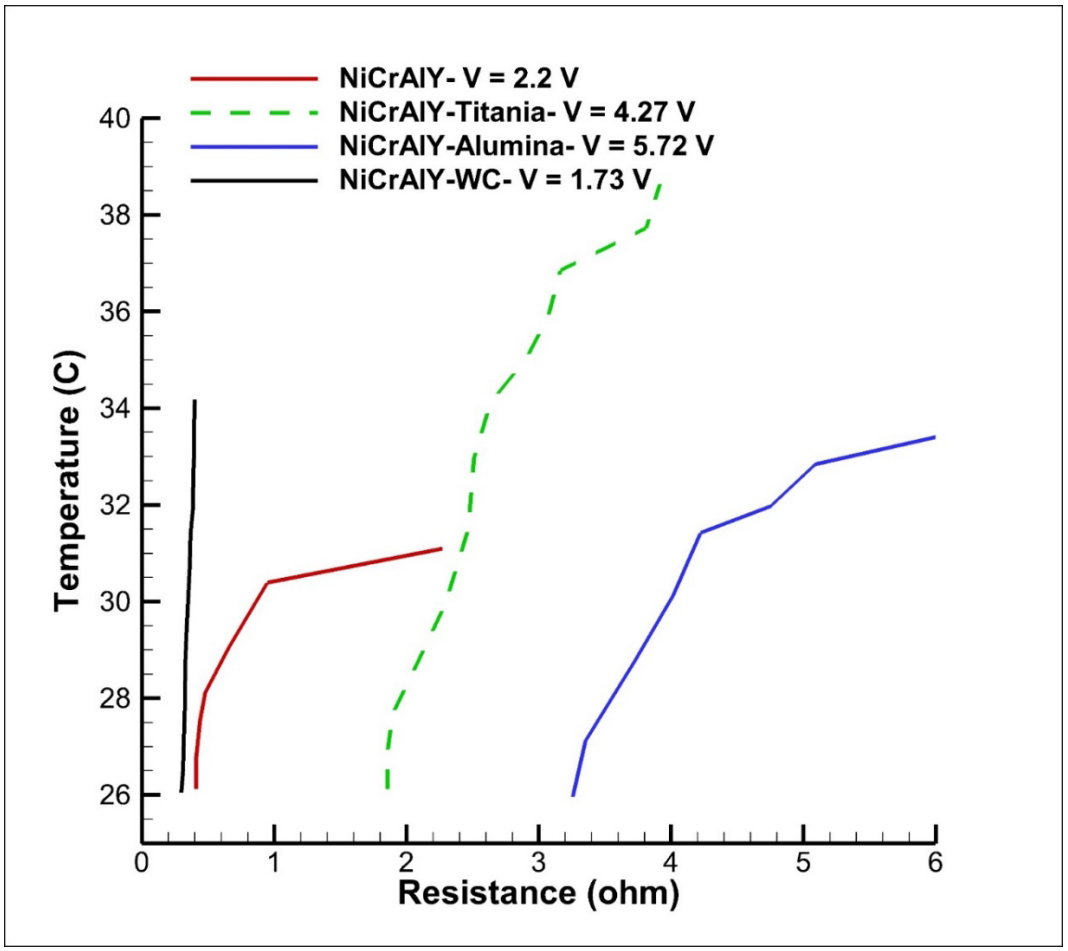

Figure 3-10 Real-time electrical resistance versus real-time temperature

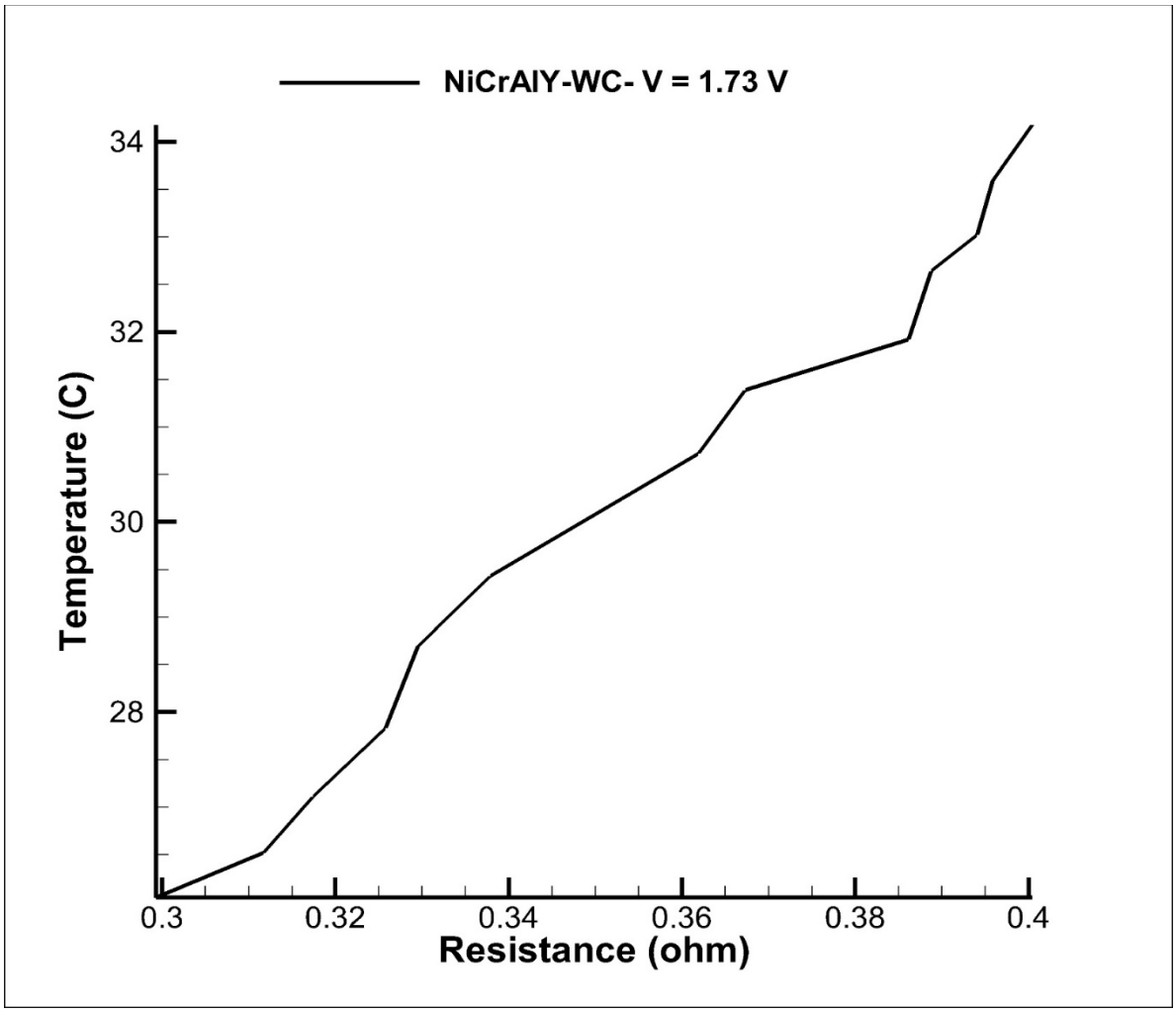

Figure 3-11 Real-time electrical resistance versus real-time temperature- NiCrAlY-WC-12Co

As observed in Fig 3-10, contrary to the electrical current the electrical resistance increases for all materials. It is evident that the tungsten carbide coating exhibits the lowest variation in electrical resistance. The same trend as Fig 3-9 with regards to the curve slopes is observed in Fig 3-10 and could be partly attributed to the considerable differences in initial electrical resistance. In the case of NiCrAY-alumina, it could be seen that it was able to reach a higher temperature compared to that of pure NiCrAlY. The established promising heating performance of NiCrAlY-alumina results in achieving higher temperatures. It is noteworthy that

NiCrAlY-titania could reach relatively high temperatures while being under erosion. This could be attributed to the fact that NiCrAlY-titania exhibited relatively high wear resistance and promising heating performance, second only to NiCrAlY-alumina. Table 3-10 lists the time averaged mass loss of the coating-based heating elements. As expected, coatings with higher resistance to erosive wear lose relatively lower mass.

Table 3-10 The time average amount of mass loss during the erosion tests with heating

Coating	**Mass loss (g/s)**
NiCrAlY	0.0546 ± 0.0046 (n = 3)
NiCrAlY-alumina	0.0538 ± 0.0039 (n = 3)
NiCrAlY-titania	0.0495 ± 0.0042 (n = 3)
NiCrAlY-WC-12Co	0.0473 ± 0.0037 (n = 3)

3.3 Conclusions

In the present study, several WDE and solid particle impact erosion tests were conducted in order to investigate the effect of certain ceramic reinforcing particles on the erosive wear rate of coated heating elements. With NiCrAlY as the matrix phase, three different MMC coatings were fabricated using tungsten carbide, alumina, and titania as the reinforcing phases. The experimentally obtained data clearly demonstrated that the NiCrAlY-WC-12Co MMC coating had an appreciably lower erosive wear rate (measured by mass loss) compared with other deposited coatings. Moreover, the NiCrAlY-titania coating exhibited considerably better erosion resistance compared with the NiCrAlY and NiCrAlY-alumina coatings. It is noteworthy that the

results of the WDE and solid particle impact tests were in agreement in distinguishing the coatings with the best erosion resistance.

Confocal microscopy was conducted on the samples before and after the WDE experiments. All the coatings moved towards rougher surface profiles caused by the increase in kurtosis. Based on the observed kurtosis variation, coatings with the higher amounts of mass loss demonstrated higher variation in surface profile. The same trend was also observed in the topographical images of surfaces after dry erosion tests captured by stereo microscopy. The results of the present study show that implementing MMC coatings has a positive effect on erosive wear resistance of resistive heating elements. This indicates that MMC coating-based de-icing systems could be employed not only because of their effective heating, but also due to their improved mechanical properties and durability.

In order to examine the performance of heating elements under harsher and more realistic conditions, the heating elements were exposed to solid particle impingement while the Joule heating occurs. As the erosion continues, material removal from the surfaces of the material results in increase of the electrical resistance and subsequent reduction of the electric current. Coatings with higher wear resistance, performed better in terms of mass reduction and durability. Thus, the heating performance under solid particle impact is not only affected by electrical resistance and heating capability, but also wear resistance.

Chapter 4

Application of Thermally Sprayed Coatings as De-icing Systems

The ultimate goal of developing novel MMC thermally sprayed heating elements was to implement them for de-icing or anti-icing purposes. Therefore, various de-icing experiments were performed inside a closed-loop icing wind tunnel. In the first stage of the tests, coatings were deposited on cylindrical coupons and were placed inside the wind tunnel. Through applying identical wind tunnel parameters, the amount of ice accretion was measured for different coatings under the same duration. These measurements were performed to assess whether there is a significant variation among the coatings in terms of mass of accreted ice.

During the second stage of the experiments, rectangular low carbon steel substrates were chosen as the substrate for coating deposition. These samples were then placed inside the closed-loop icing wind tunnel to evaluate its anti-icing performance. While monitoring the surface temperature with a pyrometer, electrical current is applied when the ice accumulation is completed. The duration of icing and the pertaining wind tunnel parameters were constant for all the coatings for consistency. It was observed that the de-icing performance is higher for coatings with relatively better heating performance, such as NiCrAlY-alumina.

In the last stage, droplets of water with equal mass were placed on top of the coating surfaces at -10 ℃. Due to varying surface energies of the applied coatings, the geometry of the solidified droplets and were significantly different. The sample is then immediately placed in

front of the high-speed camera and the electrical current is applied. These observations would provide a better understanding of the de-icing process at lower scales.

4.1 Experimental Method

4.1.1 Feedstock Material and Coating Deposition

The feedstock powders used for the coatings is identical to the ones mentioned in Sec 3.1.1 (for cylindrical samples), and Sec 2.1.4 (for flat samples). All the substrates were low-carbon steel 44W (ASTM A36) and grit blasting was performed to roughen the surfaces and improve the adhesion. They erodent material was #24 alumina grit (Manus Abrasive Systems Inc., Edmonton, AB, Canada). The spraying parameters for round bars were identical to that of Sec 3.1.1 and parameters for rectangular samples were identical to that of Sec 2.14. The electrical copper terminals were covered with water resistance tapes to prevent electrical disruptions. However, the surfaces of the coatings were not covered by a sealing because it would modify the surface and adds another layer complexity to the measurements and observations.

4.1.2 Ice Accretion Experiments

Figure 4-1 shows the schematic of the icing wind tunnel used for icing-de-icing experiments. The test section of this wind tunnel has a rectangular shape and its width is 10 cm. This wind tunnel is capable of reaching temperatures as low as -20 °C provided that the air velocity is set on 10 m/s [92]. When the air velocity is increased inside the wind tunnel, the minimum achievable temperature will increase due to shorter residence time at the evaporator of the chiller.

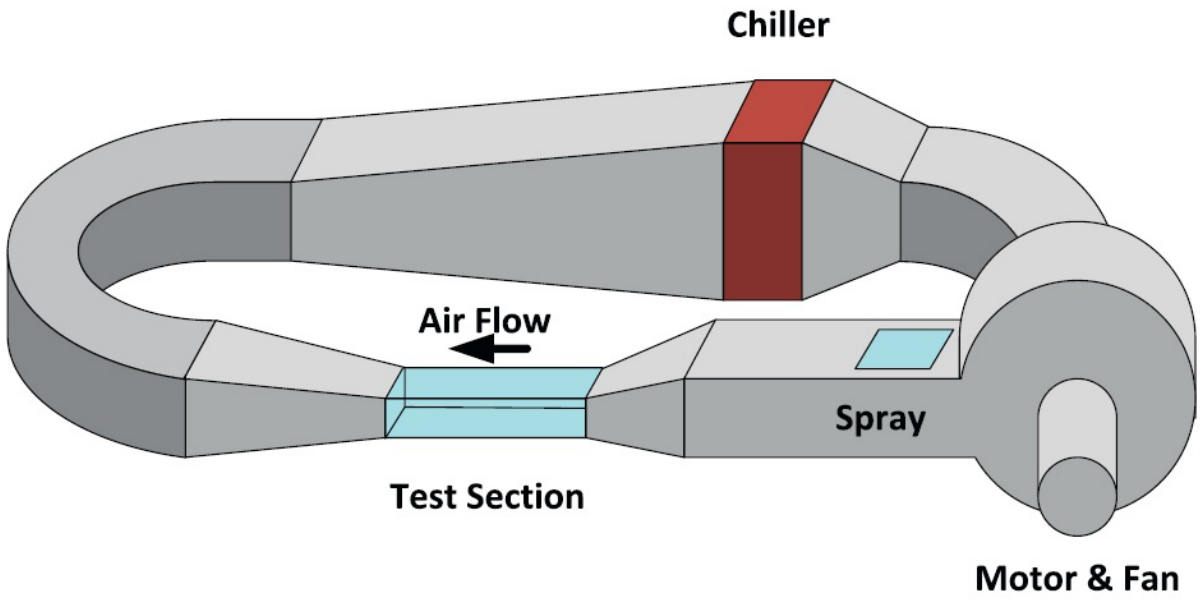

Figure 4-1 Schematic of the icing wind tunnel at the Concordia University [92]

Using an air atomizing nozzle, the supercooled water droplets were injected to the air stream to simulate in-cloud icing. The liquid water content of the air stream could be measured by using a standard substrate at the center of the test section and exposing it to ice accumulation. By measuring the ice thickness after a specific period of time, the liquid water content could then be calculated [92]. The water used for these experiments should be distilled and preferably cold (near-zero) for the droplet to be supercooled in a timely manner.

Three cylindrical coupons were tested for each material in order to compare the mass and profile of icing over an equal amount of time. The samples were mounted in the middle of the section of the wind tunnel which is shown in Fig 4-2. The operating parameters of the wind tunnel is listed in Table 4-1.

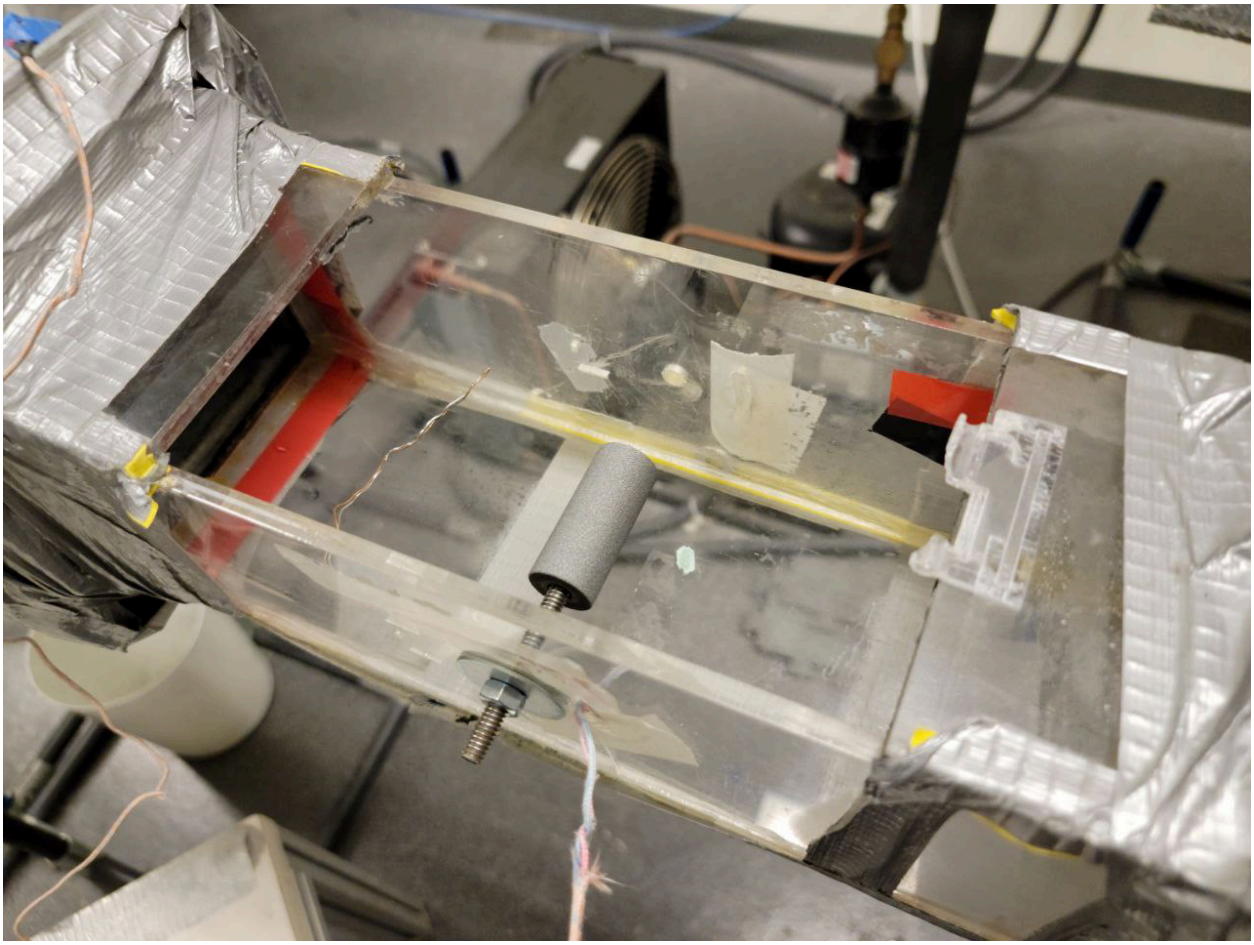

Figure 4-2 Cylindrical coupon placed at the center of the icing wind tunnel

By measuring the mass of accreted ice, a comparison could be made regarding the initial ice mass of the heating elements prior to heating. Note that during the heating tests, this cannot be done since the removal of the sample from the wind tunnel for mass measurements would compromise the ice and introduces significant experimental errors. Rectangular samples were also placed inside the test section at an angle to observe and study the process of icing before activating the heating system. For these samples, two types of ice were formed at -3 °C and -10 °C in order to observe the difference between the morphology and structure of the ice formed at different temperatures. A pitot tube was used to measure the air velocity in the test section which

had less than 5% difference with the water droplet velocity [92]. The standard deviation for air velocity and liquid water content were ± 2 m/s and ± 0.1 g/m^3, respectively [23]. De Pauw and Dolatabadi [17] characterized the water droplet spray by implementing a phase Doppler particle analyzer. The liquid water content of the spray was 0.5 g/m^3 and the median volume diameter was around 30 μm.

Table 4-1 Operating parameters of the wind tunnel for icing tests

Fan frequency [Hz]	50
Air velocity [m/s]	45
Air jet pressure [psi]	40
Pressure inside the pressurized water container [psi]	40
Ice accretion time [min]	2
Liquid water content [g/m^3]	0.5
Icing temperature [°C]	-10
Coupon length [in]	2.5

Figure 4-3 demonstrates the rectangular samples placed at the middle of the test section with an angle of 35 degrees. The overall amount of icing for these samples was set on 90 seconds. By fixing the chiller-controlled temperature on the relevant setpoint, the test section would reach that temperature in a few minutes. The air temperature of the test section is measured by a K-type thermocouple. When this thermocouple reports the target temperature, the water jet must be turned on for a specific amount of time. Using this method, ice could be

formed at different temperatures. However, after formation of the ice at the setpoint temperature, the temperature of the test section could be further reduced, if needed.

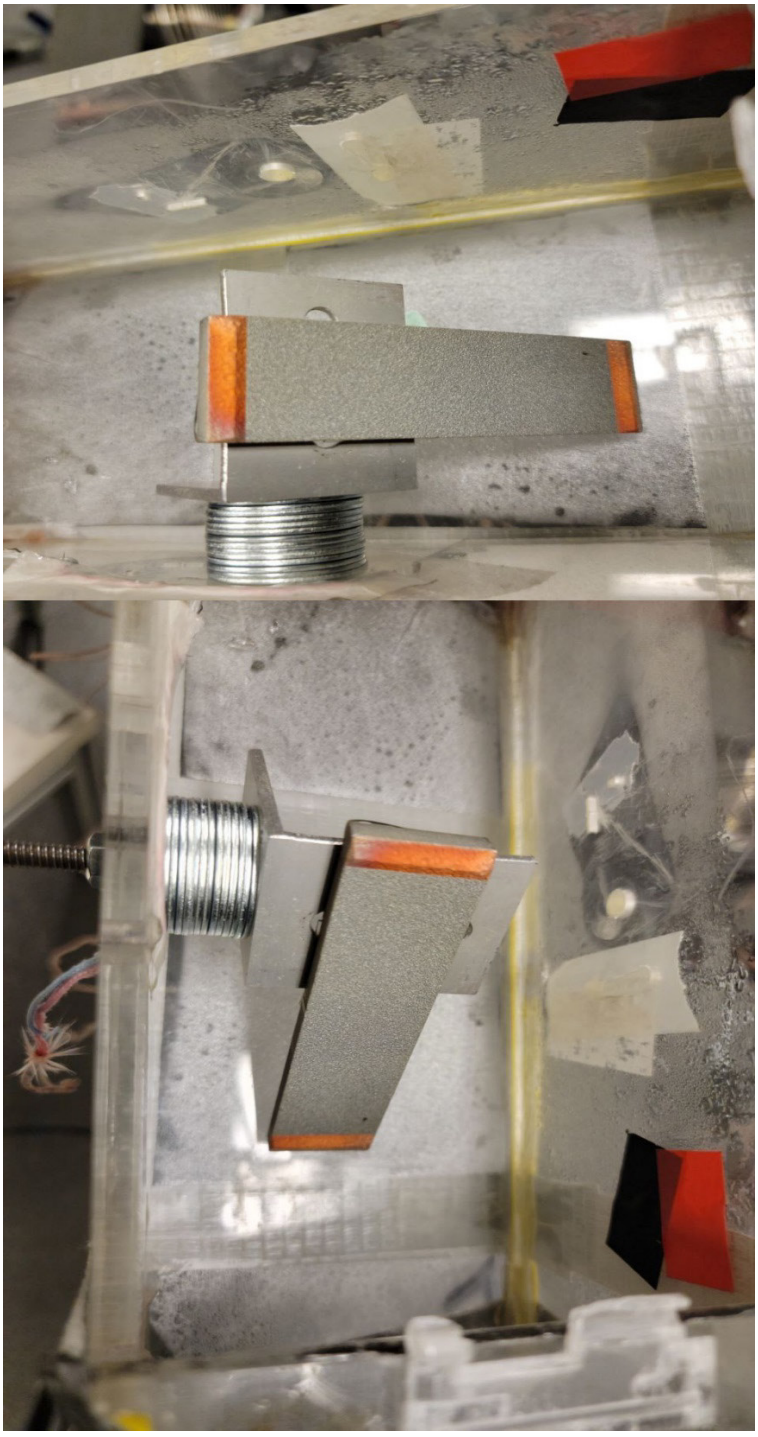

Figure 4-3 Rectangular samples placed inside the icing wind tunnel

4.1.3 De-icing Tests

For the de-icing tests, fully developed heating elements were placed at the center of wind tunnel with a 35 degree angle. The initial electrical resistance of the elements is measured and based on that the applied voltage is calculated so that all the heating elements have the same power. Figure 4-4 shows fully developed heating elements placed inside the wind tunnel test section. The temperature of the surface of the coatings is monitored using a pyrometer. The wind tunnel parameters for these experiments are listed in Table 4-2. The rest of the parameters are identical to that of Table 4-1.

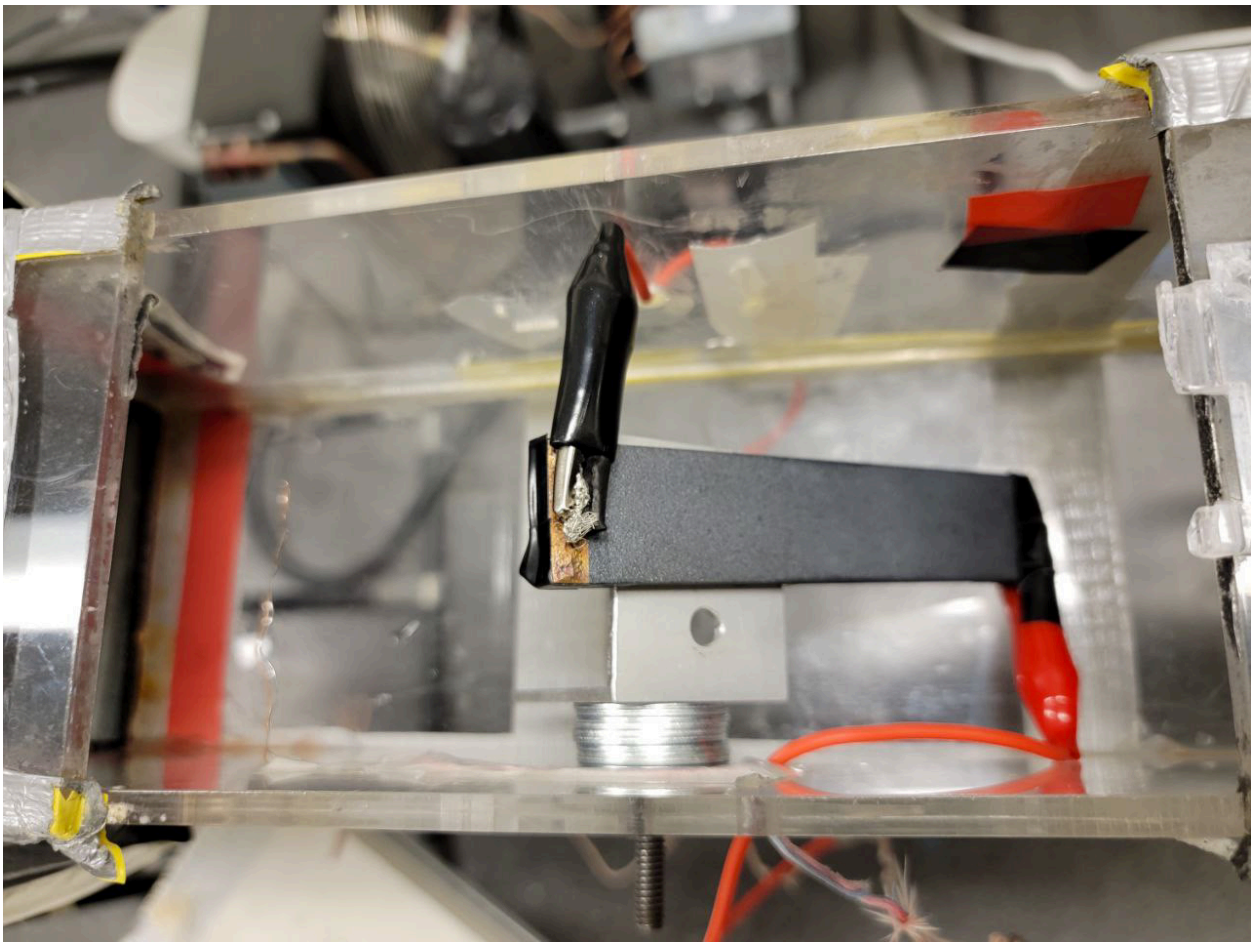

Figure 4-4 Fully developed heating elements installed at the test section

Table 4-2 Operating parameters of the wind tunnel for deicing

Ice accretion time [s]	90
Liquid water content [g/m^3]	0.5
Icing temperature [℃]	-3
Coupon length [in]	5
Final steady state temperature before heating [℃]	-10

4.1.4 High-Speed Imaging of The Melting Ice

For these experiments, samples were first placed inside a freezer to reach the temperature of -10 c. Then, identical powder droplets (one for each sample) maintained at 1 ℃ were deposited on the samples with a water droplet dispenser. When the sample and the droplet reach the steady-state condition at -10 ℃, there are immediately placed in front of a high-speed camera and electrical current is applied simultaneously. Similar to the de-icing tests, the voltage is calculated so that all the elements receive equal electrical power. The high-speed camera is activated upon starting the experiments. However, due to the high frame rate, only a few seconds of the process could be recorded.

4.2 Results and Discussion

4.2.1 Ice Accretion Experiments

Figure 4-5 shows the ice accumulation on the surface of cylindrical coupons. It was observed that for all the coatings the mass of accumulated ice is within the same value. In addition, the shape and geometry of the ice were very much similar. Generally, the air velocity on the aircraft surfaces is much higher than 45 m/s. However, at speeds considerably higher than 100 m/s there is low risk for in-cloud icing [92]. Thus, in terms of ice formation, the presented experimental setting would not cause a critical issue as there is considerable in-flight icing at the air velocity of 45 m/s. Table 4-3 lists the mass of ice accumulation which was immediately measured on an accurate balance scale. As observed in Fig 4-5, for all the coatings the ice has a very uniform geometry, and the thickness of the ice is virtually the same. However, more ice is usually accumulated around the edges.

Table 4-3 The average amount of ice accumulation in 2 minutes under 45 m/s

Coating	Mass of accumulated ice (g)
NiCrAlY	1.364 ± 0.094 (n = 3)
NiCrAlY-WC-12Co	1.586 ± 0.116 (n = 3)
NiCrAlY-alumina	1.507 ± 0.089 (n = 3)
NiCrAlY-titania	1.439 ± 0.108 (n = 3)

According to the values listed in Table 4-3, the average amount of ice accumulation are within the same degree. However, they are not identical due to the different surface properties. The water atomizing nozzle is placed at the upstream of the flow in order to provide adequate

time for the droplet to equilibrate with the air flow and reach the required temperature. Also, spraying the water droplet in the upstream would provide a more uniform distribution of micron-sized water droplets in the test section.

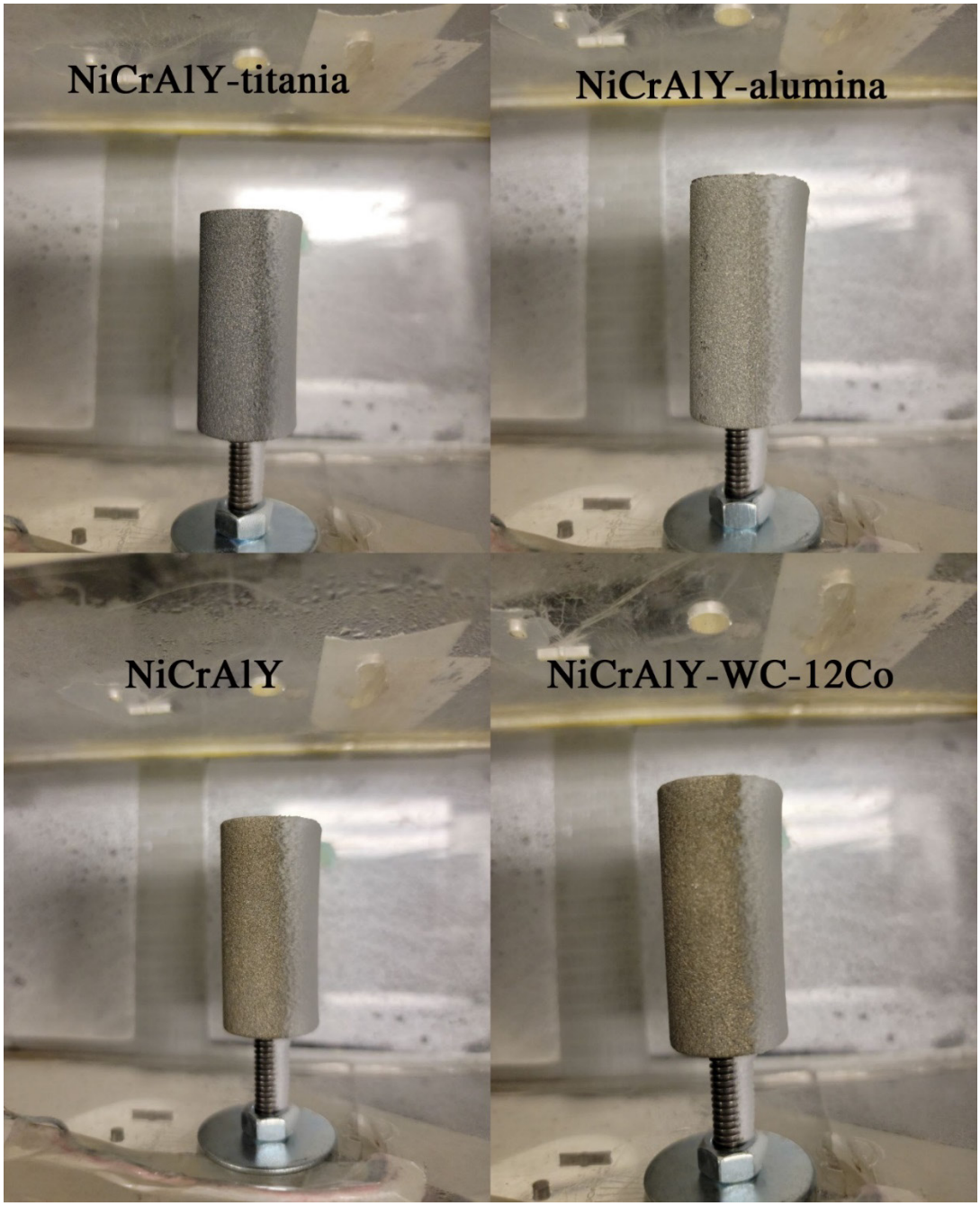

Figure 4-5 Ice accretion on the surface of cylindrical coupons

Due to placement of the rectangular heating elements at angle of 35 degrees in the de-icing tests, the sampled were mounted with the same angle for consistency. For these specimens, the objective was to observe the uniformity, morphology, and shape of the ice. Also, from these tests a comparison could be made among the different coating materials. Figure 4-6 shows the icing on NiCrAlY-titania with ice formation at -10 ℃. As the icing in this case was very much similar for the different materials, only one would be presented here.

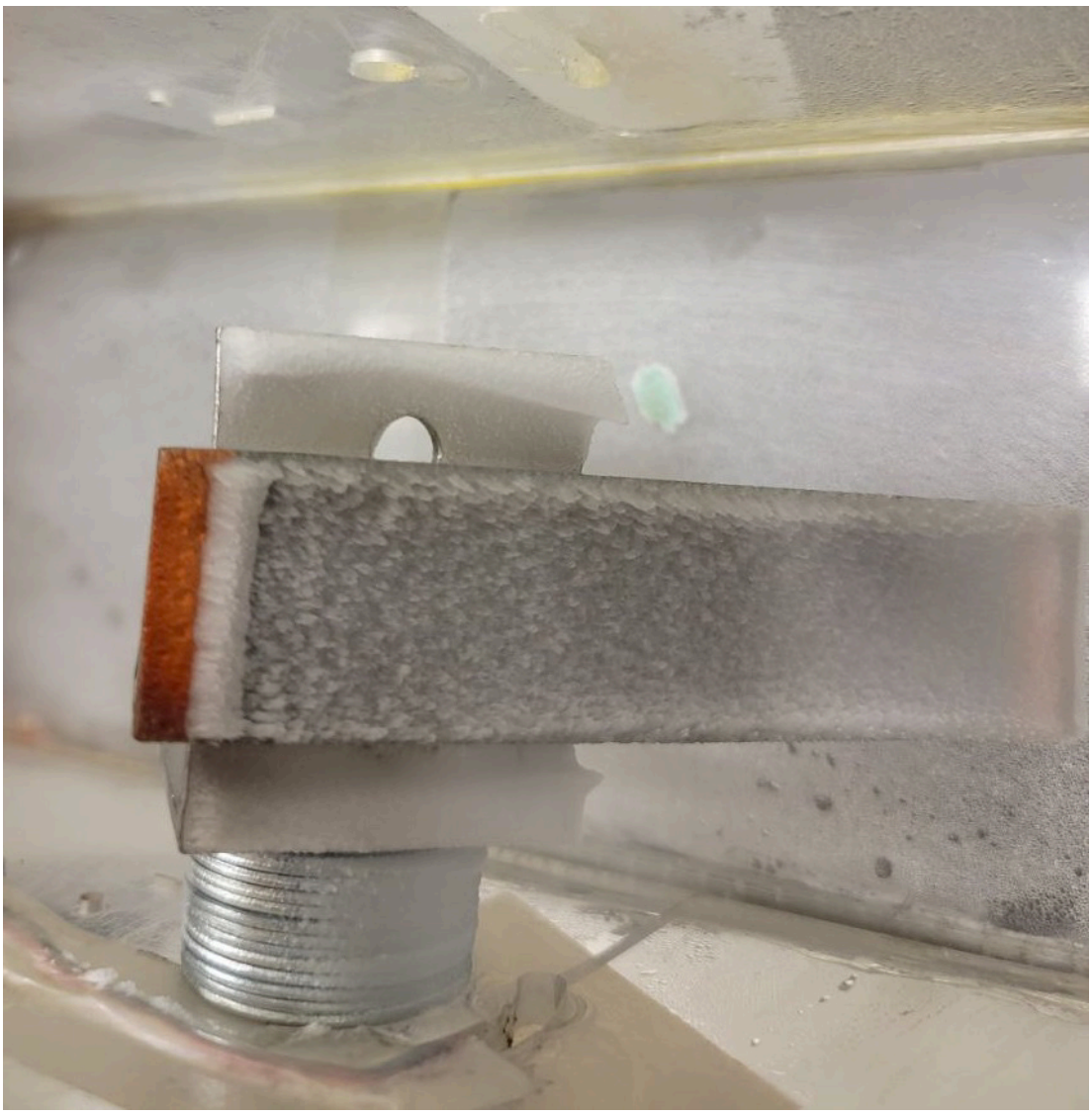

Figure 4-6 Ice accretion on NiCrAlY-titania with ice formation at -10 ℃

The in-cloud ice which is formed within a temperature range of -4 ℃ to -1 ℃, has significantly higher adhesion to the surface as it has higher contact with the surface. This type of ice is more transparent and has lower porosity compared to the ice formed at -10 ℃ which is not transparent. Figure 4-7 shows the ice formed at -3 ℃ for NiCrAlY-titania during 90 seconds of ice accumulation. As expected, it is evidently observed that this type of ice is significantly more transparent (glass-like) and has a less porous structure. This observation is important as the ice adhesion of ice formed at -10 ℃ is significantly less than that of -3 ℃.

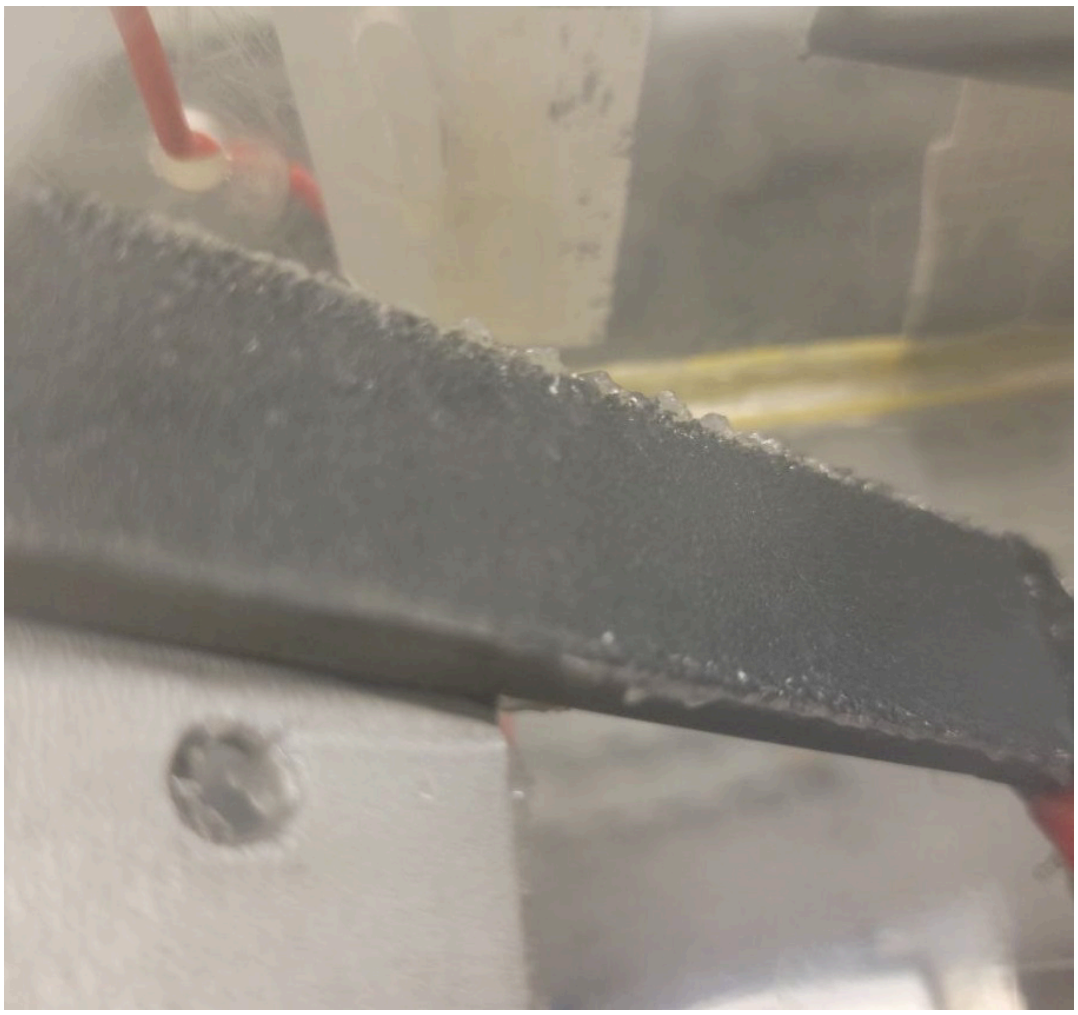

Figure 4-7 Ice accretion on NiCrAlY-titania with ice formation at -3 ℃

The rate of ice accretion and its amount on a non-heated surface depends on the droplet size, surface finish, air velocity and temperature, and the liquid water content. The rate to which the water droplets are intercepted by the surface differs from the rate to which the water droplets freeze on the surface to form the ice [68]. The rate of interception is dependent on the liquid water content and the air velocity. In the case of an airplane, the speed of the aircraft must be considered and its relative velocity with respect to the airflow must be also taken into account.

The rate of the ice formation is mainly governed by the heat transfer between the droplet and the surface. For ice nucleation, the water droplets must dissipate the latent heat of solidification must be dissipated into the surface. The two prominent processes of heat loss for the water droplet are evaporative cooling and convection. While the convection is dependent on air velocity, geometry, roughness, and the air temperature, the evaporative cooling is mainly dependent on the vapor pressure of the water which is itself governed by pressure and temperature [68].

Formation of ice at lower temperatures causes the droplet to freeze completely upon impact. This results in an opaque white ice with a roughness significantly higher than ice formed at relatively high temperatures. With higher airflow temperatures (near zero) and at relatively high velocities, part of the water droplets will not be frozen upon impact. This remaining water which runs through the surface is called runback. This could produce localized high thickness spots as the runback water begins to freeze on the surface [68]. This type of translucent ice (see Fig 4-6) is referred to as glaze and has considerably better adhesion to the surface.

4.2.2 De-icing Experiments

For all the heating elements, after formation of ice at -3 ℃, the water atomizing nozzle will be deactivated to stop further ice accretion. The airflow temperature and consequently that of the ice and the substrate would then be set on -10 ℃, then the electric current would be applied. It should be noted that the fan should not work at high-speed when the de-icing process is going on. When the melting begins, the shards of ice could be detached from the surface during the heating process; this would damage the wind tunnel system. For this reason, the air velocity was set as low as 5 m/s during the de-icing process. Figure 4-8 shows the images of the NiCrAlY-alumina de-icing element after 2 minutes of heating. NiCrAlY-alumina exhibited the same behavior as NiCrAlY-WC-12Co and NiCrAlY, in terms of the detachment process.

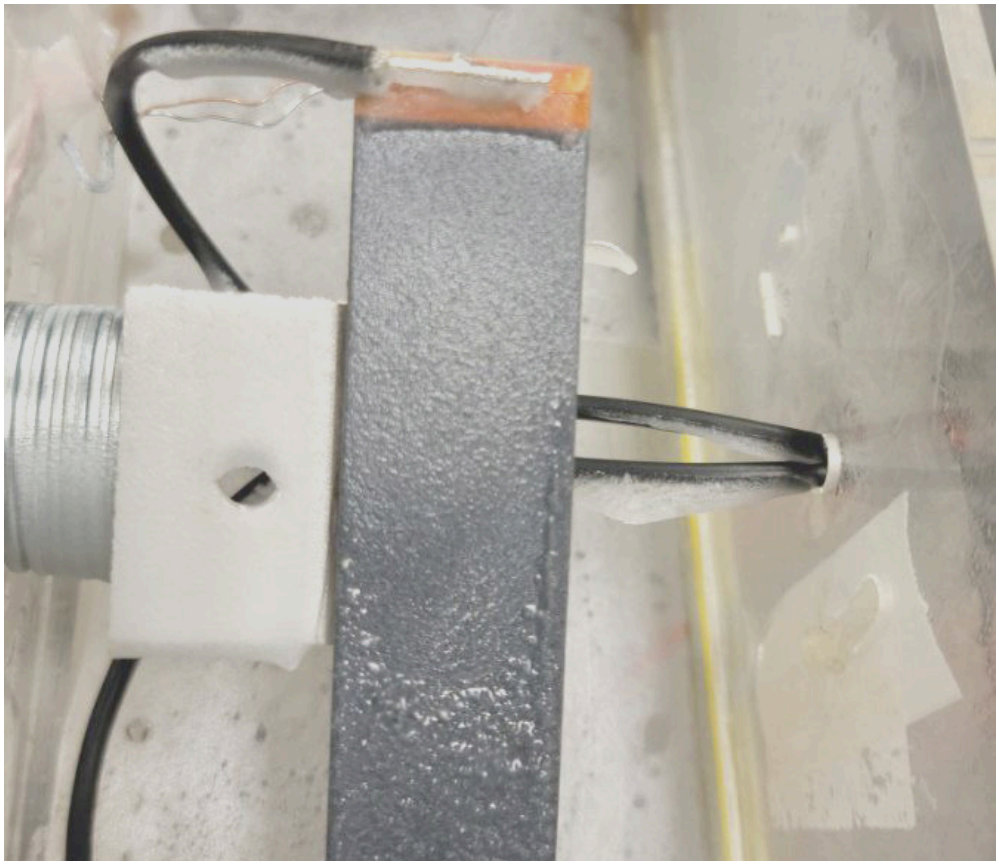

Figure 4-8 NiCrAlY-alumina coating after 2 minutes of de-icing

For all the coatings, gradual localized melting was observed and droplets of liquid water drop from the sample or is vaporized. However, in the case of NiCrAlY-titania the ice was detached in form of a flat layer of ice. The growth of the water film beneath the layer of the ice and type of ice detachment is very much dependent of the surface properties of the coatings and the surface energy. Figure 4-9 demonstrates the detached layer from the NiCrAlY-titania coating. As reported by Sharifi et al. [92], TiO_2 coatings can perform as promising hydrophobic surfaces with appropriate surface treatment due to their relatively low surface energy.

Figure 4-9 NiCrAlY-titania coating after 2 minutes of de-icing

In terms of energy consumption, power is not the only parameter that must be considered. The cumulative consumed energy is also dependent on the whole duration of de-icing which includes the time for sensible temperature increase up to the melting point, and the latent heat transfer for melting. Figure 4-10 shows the total consumed power versus the total de-icing time for the thermally sprayed heating elements.

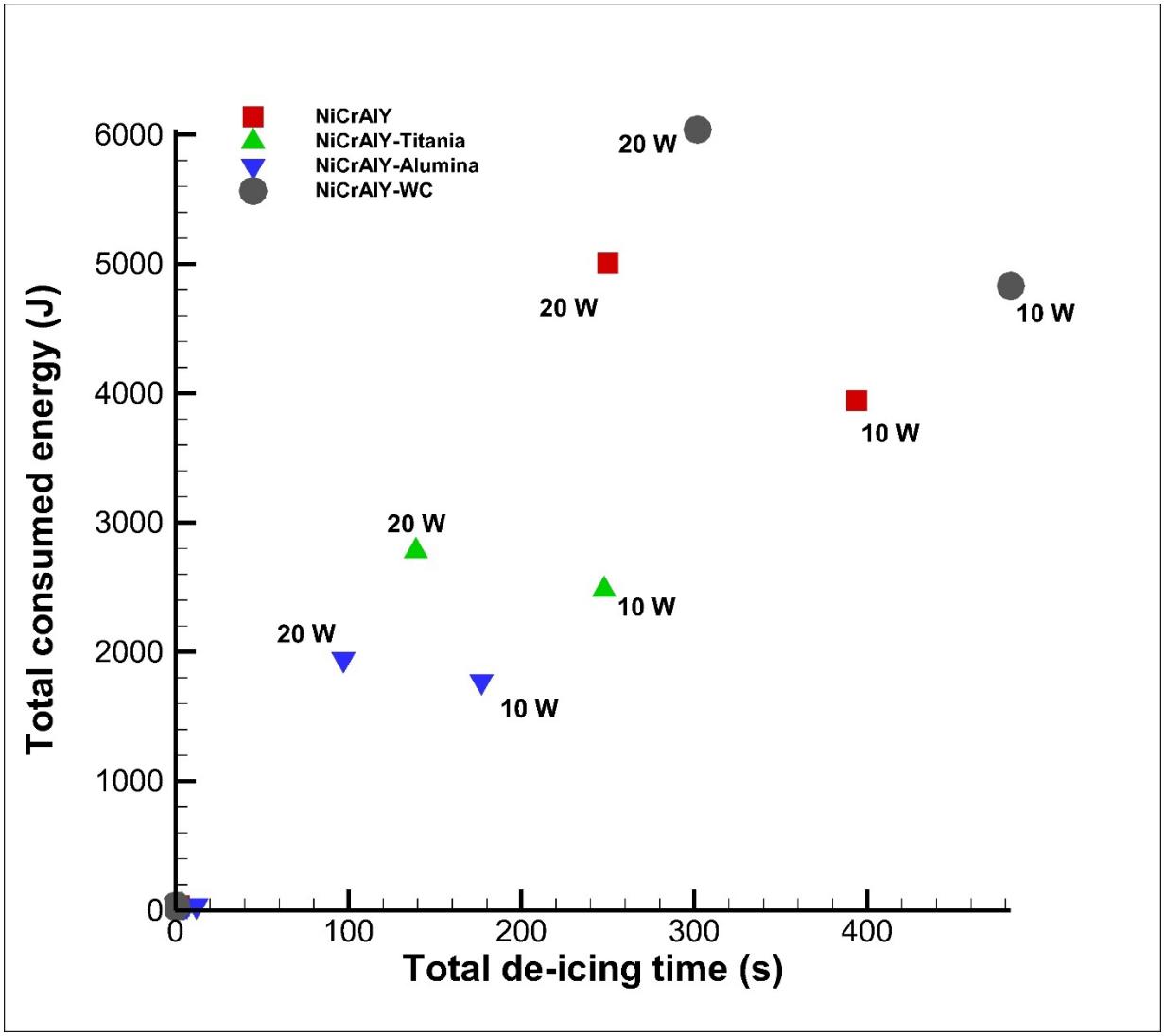

Figure 4-10 Total consumed energy versus the total de-icing time for the thermally sprayed heating elements

A number of observations could be made based on Fig 4-10. The materials with relatively higher electrical resistance, perform considerably better in terms of both time and consumed energy. In addition, increasing the applied power to the elements does not necessarily result in better outcome. An increase in power will definitely reduce the total de-icing time but might lead to higher overall energy consumption. In industry, it is preferred to work with lower voltages in order to avoid heat loss and electric shocks. Note that the de-icing is considered complete when all the ice is detached from the surface.

In order to estimate the rate of melting, three samples for each material were chosen and weighed. These samples were then installed in the test section for ice deposition at -3°C. After the temperature dropped to -10°C, the samples were quickly removed from the test section and were weighed using an accurate balance. By dividing this amount by the total time of de-icing for each element (sensible heating and melting), the rate of de-icing is calculated in terms of mass. However, this is not the melting rate as the time for sensible heat transfer (to increase the ice temperature from -10°C to the melting point of 0°C) is also considered. Table 4-4 lists the average de-icing rate for all the heating elements.

Table 4-4 The average calculated de-icing rate of the heating elements (10 W)

Coating	**De-icing rate (g/s)**
NiCrAlY	0.0024
NiCrAlY-WC-12Co	0.0027
NiCrAlY-alumina	0.0066
NiCrAlY-titania	0.0049

The significant point here is the agreement of the de-icing performance with the heating performance presented in Section 2.3.4. Coatings with higher electrical resistance performed significantly better in terms of the required time and energy.

4.2.3 High-speed Imaging of the Droplet Melting Process

Figure 4-11 illustrates the melting process of a frozen water droplet at -10 ℃ on the NiCrAlY-WC-12Co coating. Due to the limitations of the recording system, the recording began immediately after the first signs of melting are observed, then it would continue for 5 seconds. Besides studying the shape and geometry of the droplets which are highly dependent on the surface energy, the response to de-icing is also studied. Three images are selected for each material to examine the initial instances of melting. The applied power for all the elements was 10 W.

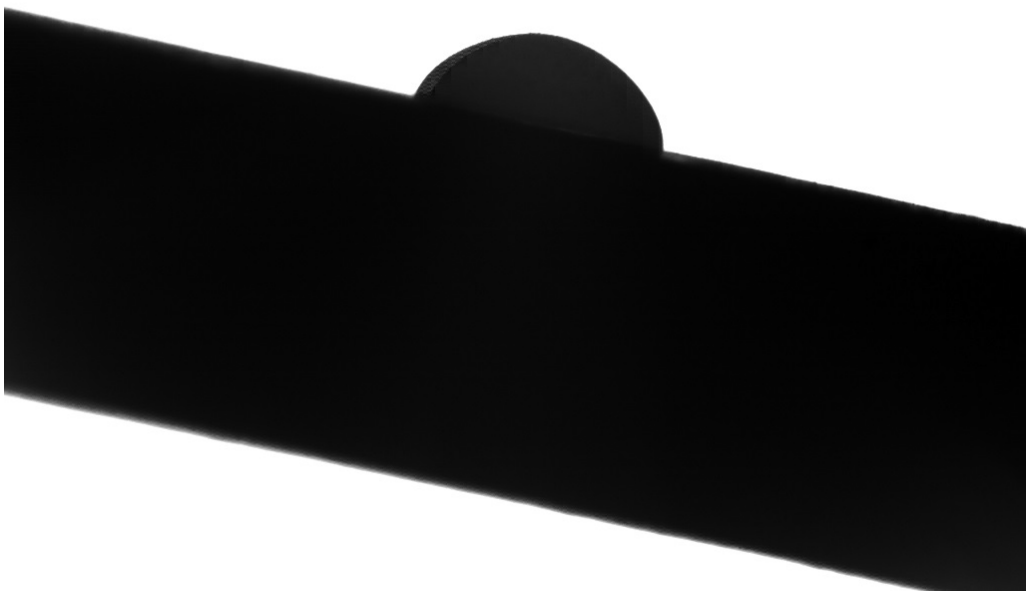

(a)

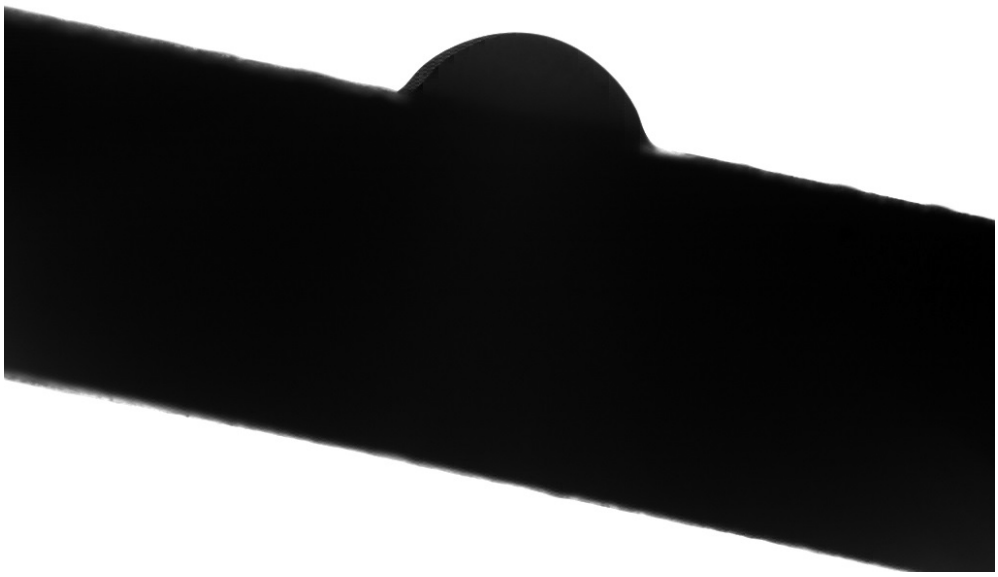

(b)

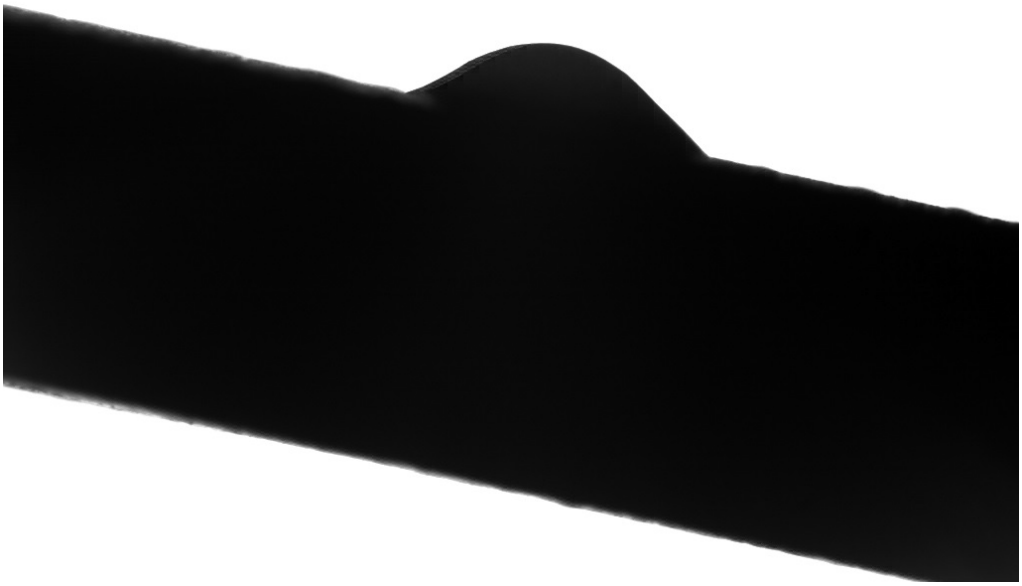

(c)

Figure 4-11 Water droplet response to heating for NiCrAlY-WC-12Co coating

As evident in Fig 4-11, the growth of the water film starts from the surface itself and then it grows to the whole droplet. For this reason, the part of the droplet which is near the surface may run over the surface when melted so that the droplet becomes relatively more elongated. As shown in Figure 4-12, the equilibrium equation for liquid water droplet on a solid surface is the Young equation. With γ as surface energies, based on the Young equation ($\gamma_{w,s} + \gamma_w cos\theta = \gamma_s$) the contact angle plays an important role in determining the solid surface energy [93]. The surface with higher contact angle of the droplet has relatively lower surface energy.

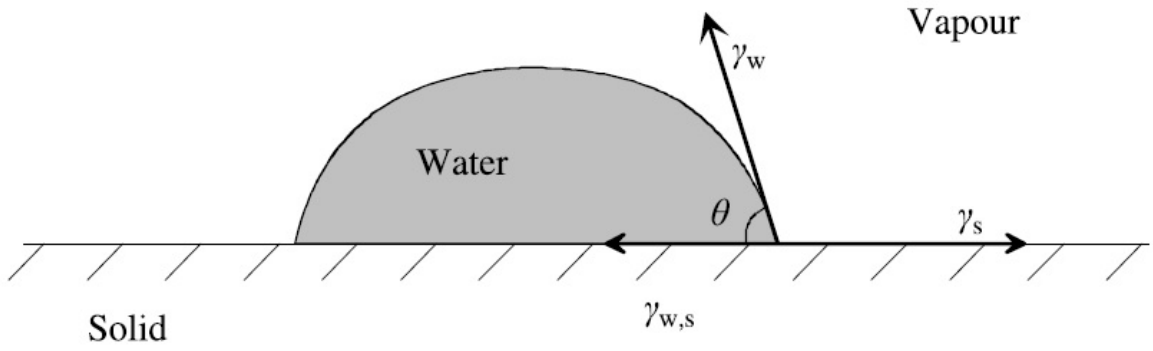

Figure 4-12 Schematic of water droplet on a surface with θ as the contact angle [93]

In the case of a solidified droplet on a solid surface, the thermodynamic work of adhesion is the required work to detach the ice from the surface and break the bonds. It is defined as the sum of the surface energies of the solid and the ice subtracted by ice-solid bond energy. Given that the surface energies of water and ice are approximately equal, the thermodynamic work of adhesion can be estimated by knowing the surface tension of water and contact angle. However, the important assumption made here is that the interfacial energies of water-solid and ice-solid

are almost the same. Figures 4-13, 4-14, and 4-15 show the melting process of a droplet for the NiCrAlY, NiCrAlY-alumina, and NiCrAlY-titania coatings, respectively.

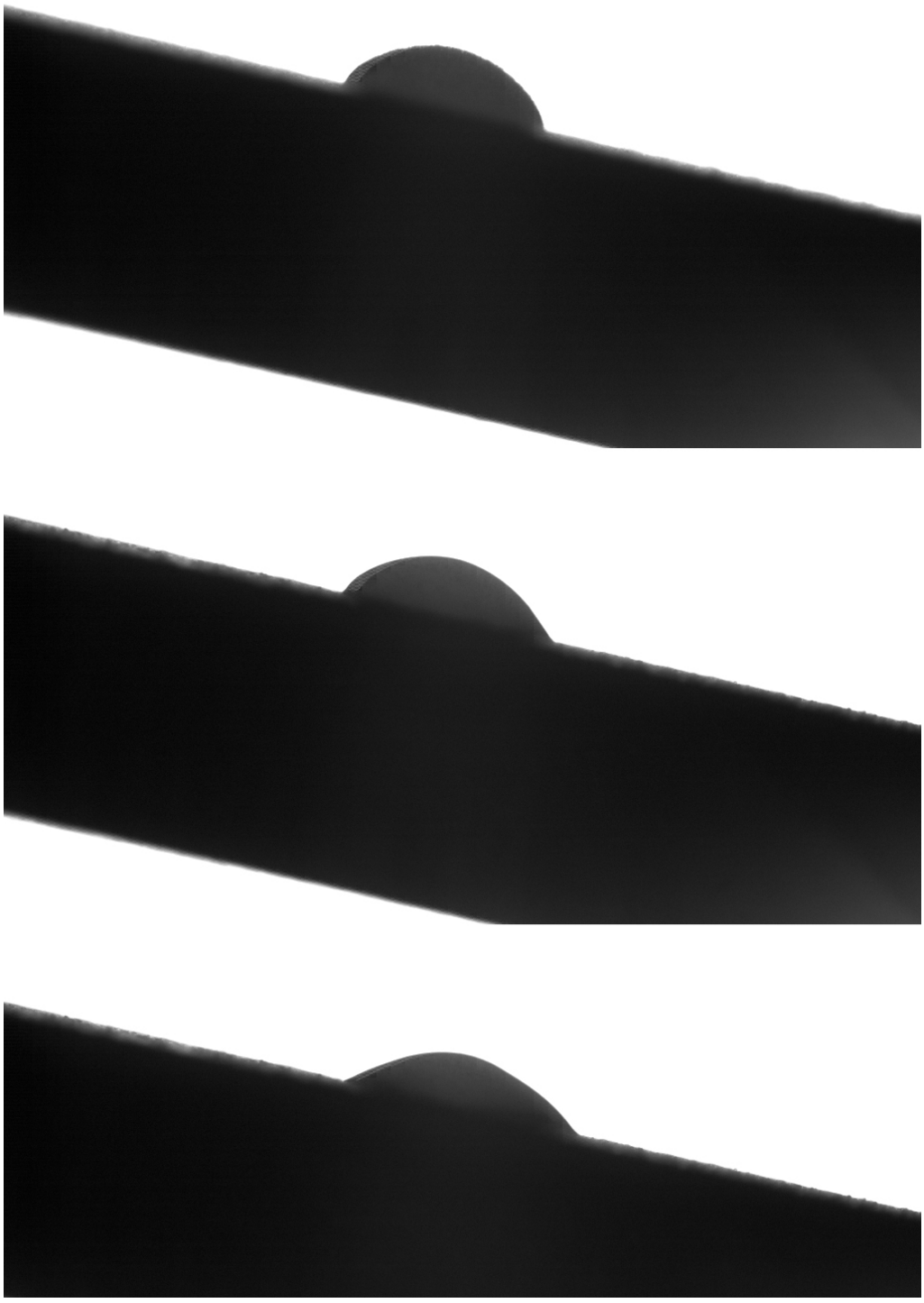

Figure 4-13 Water droplet response to heating for NiCrAlY coating

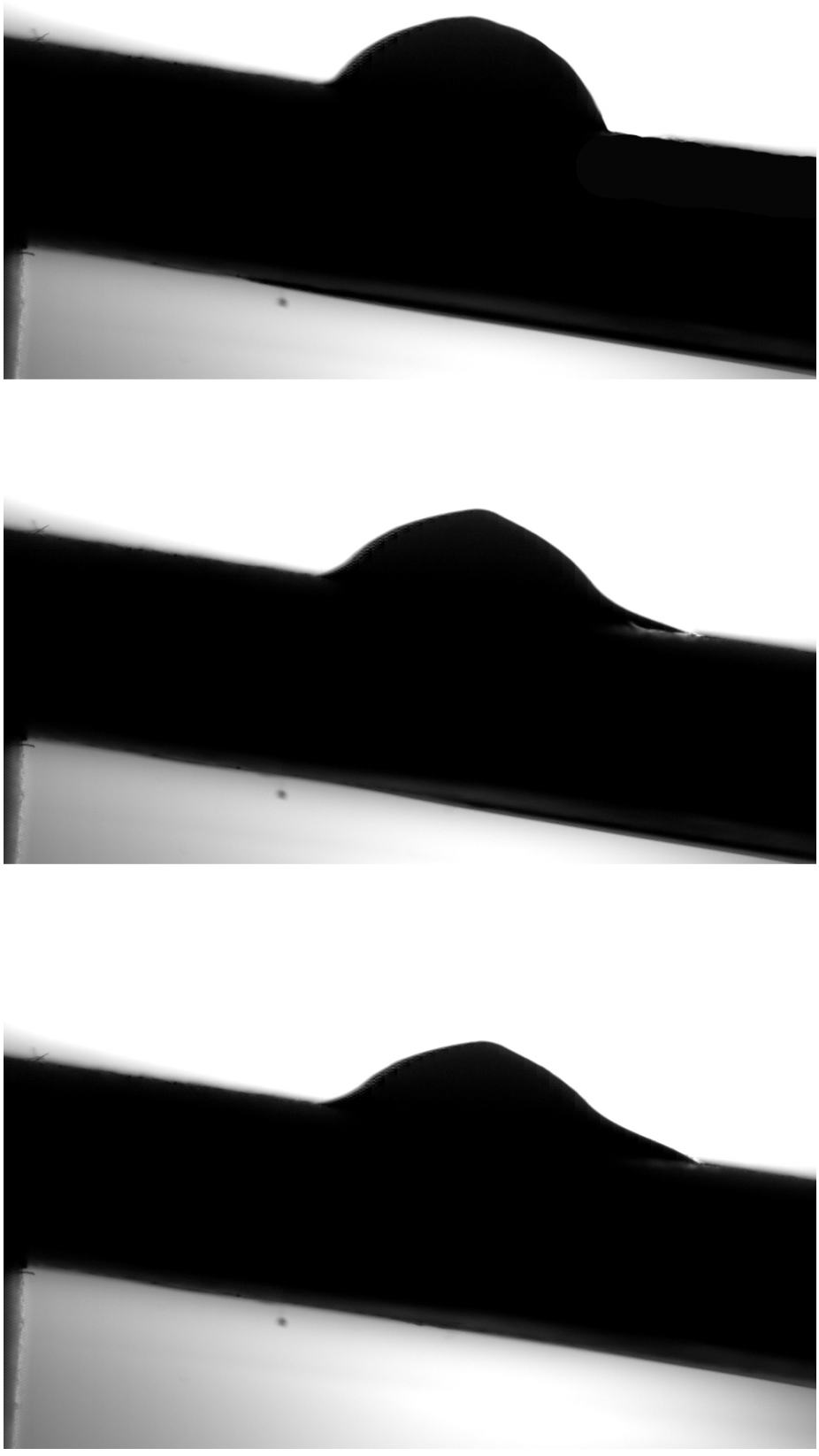

Figure 4-14 Water droplet response to heating for NiCrAlY-alumina coating

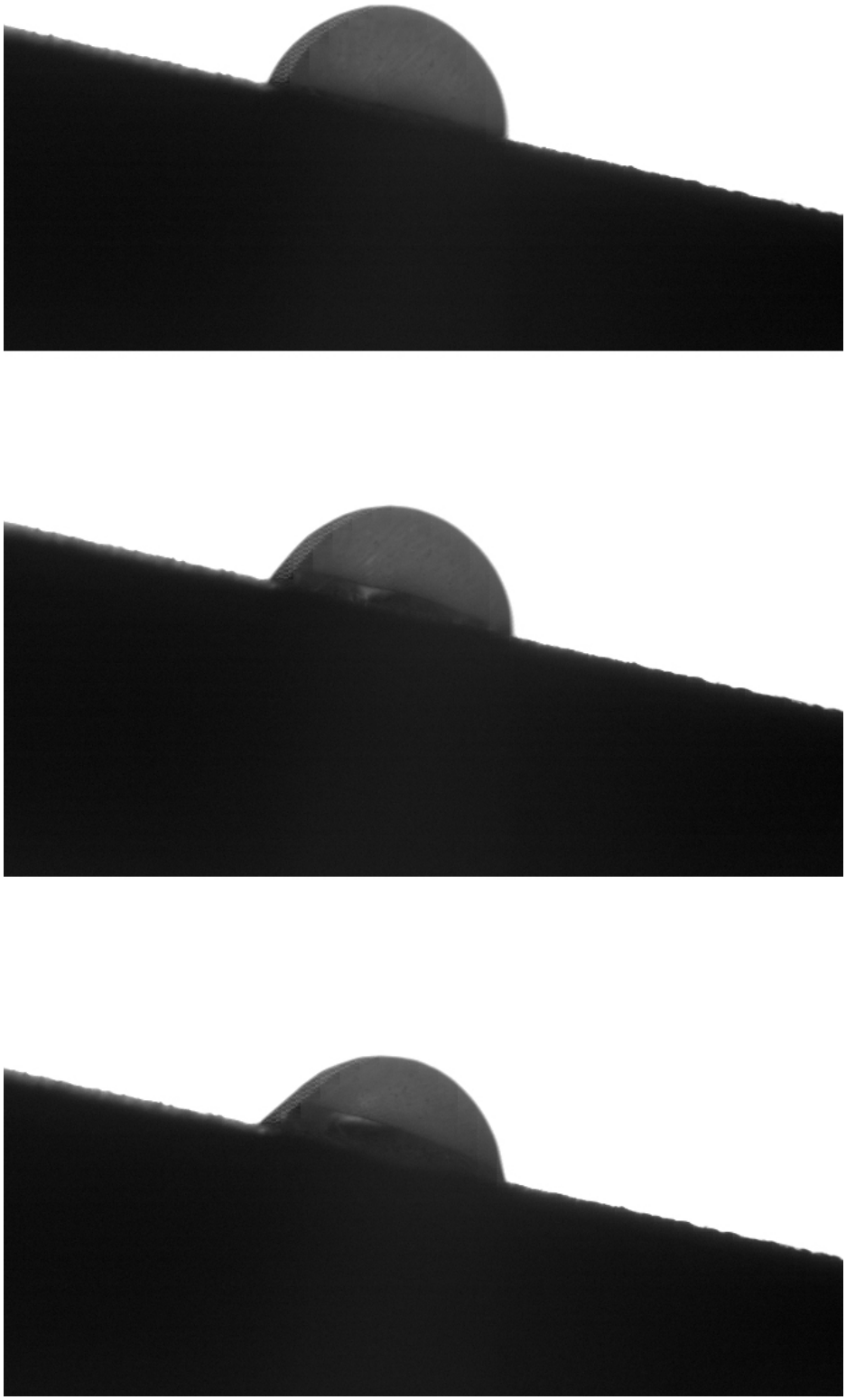

Figure 4-15 Water droplet response to heating for NiCrAlY-titania coating

A comparison between the high-speed camera images of the coating would demonstrate that the contact angle of the NiCrAlY-titania is the highest. Therefore, NiCrAlY-titania coatings must have the lowest amount of surface energy. This is in fact in agreement with the established hydrophobicity of the TiO_2 coatings due to their low surface energies [23]. Figure 4-15 clearly illustrates the growth of the water-ice interface during the melting. Unlike other materials, the melted ice at the lower part of the droplet would not run down the surface; even though the samples were placed with a 20 degree angle to also observe the effect of gravitational forces. Again, this shows that the NiCrAlY-titania coatings are considerably more hydrophobic than the rest. This could also explain the type of detachment that was shown in Fig 4-9 for the de-icing tests of NiCrAlY-titania.

According to Figs 4-11 and 4-13, NiCrAlY and NiCrAlY-WC-12Co have about the same surface energy. The important observation here is that both these coating demonstrated relatively lower heating performance as mentioned in Chapter 2. Thus, it could be seen that their melting process is very mush similar. Based on Fig 4-14, it could be seen that the rate of melting is considerably higher compared to the other coatings. This is again in agreement with the results stated in Chapter 2 which established NiCrAlY-alumina as the coating with the best heating performance.

4.3 Conclusions

After evaluating the heating performance and erosive wear resistance of the developed MMC heating elements, they were tested to evaluate their de-icing performance. Heating elements were place in-side a close-loop wind tunnel and were exposed to icing. The results

showed that the amount of ice accretion on the surfaces is within the same order for different materials, provided that all the wind-tunnel parameters are fixed.

The materials which had better heating performance exhibited also a significantly better capability in de-icing. The time of the de-icing (both sensible and latent heat transfer) and the total amount of energy are two key factors here. As expected, NiCrAlY-alumina not only consumed less energy, but also had the fastest de-icing rate. It was also concluded that increasing the voltage for higher power results in faster de-icing rate but may increase the cumulative consumed energy. The high-speed camera imaging showed that the NiCrAlY-titania coating has the lowest surface energy due to its relatively higher contact angle. It was also observed that the melted water on the surface of NiCrAlY-titania does not run down the element, unlike the other coatings. In addition, the NiCrAlY-alumina coating exhibited the fastest de-icing rate owing to its superior heating performance.

Chapter 5

Conclusions

MMC thermally sprayed heating elements were fabricated in order to combat ice accretion on airfoil surfaces. These heating elements were then tested to examine their heating performance, wear resistance, and de-icing capabilities. It was observed that adding ceramic or cermet reinforcing phases to the metal matrix makes significant changes to its microstructure, physical and electrical properties. Regarding the electrical properties such as resistivity, depending on the electrical properties of the reinforcing phase, the electrical resistivity of the metal coatings is modified. Various Joule heating experiments were conducted under forced and free convection at very low temperatures in a cold room. The results clearly demonstrated that the coatings with higher electrical resistance exhibit better heating performance. It was also established that for the same material, the coating with the least thickness would perform better as its electrical resistance would be relatively higher.

A novel two-dimensional transient heat transfer model was developed and analytically solved in order to predict the temperature distribution within the multi-layered composite coatings. Numerical simulations were also conducted to estimate the very same temperature distribution. Both solutions were in good agreement with the experimentally obtained data.

These coating-based heating elements were then tested for evaluating their wear resistance and study the impact of the MMC approach on improving specific mechanical properties and erosive wear resistance. The results demonstrated that the MMC coatings which have reinforcing phases with higher hardness such as tungsten carbide, would perform

appreciably better in terms of wear resistance. With erosion testing conducted on the materials with simultaneous activation of the heating system, the overall performance of the coatings were examined. Coatings with harder reinforcing phase, exhibited more resistance to wear. As a result the rate to which their electrical resistance changed was considerably lower.

Various de-icing tests in an icing wind tunnel showed that coatings with higher electrical resistance have considerably better de-icing capability, both in terms of the required time and total consumed energy. The results of the high-speed imaging showed that the NiCrAlY-titania coating has the lowest surface energy among the coatings, due to its relatively higher contact angle. It was also observed that the coating material and its heating performance has a significant effect on the behavior of the molten ice on the solid surface.

Chapter 6

Recommendations for Future Work

Several recommendations for conducting further research in these areas can be provided as follows:

- Deposition of the MMC coatings on surfaces of FRPC substrates with a temperature-controlled thermal spray process. Due to the extensive application of FRPCs in airfoil manufacturing, this would contribute to the field.
- An extensive turbulence analysis could be made to study the effects of the surface characteristics of the coatings on their aerodynamic performance and whether it would make any changes in the boundary layer.
- Developing a novel method for classification of MMC coatings in terms of their electrical resistivity. By depositing the feedstock materials with different percentages of the reinforcing phase and measuring their electrical resistivity and wear resistance, a correlation could be made for a wide set of materials. This would make it possible to accurately manipulate the electrical and physical properties, and microstructure. Machine learning could also be used provided that large sets of accurate data are collected.
- These MMC coatings could be further improved in terms of multi-functionality. In specific to make an MMC resistive heating element which is also highly hydrophobic. The NiCrAlY-titania presented in this study could be a good starting point.
- By implementing a Computational approach, the more complex experiments could be simulated, especially when we have different heat transfer mechanisms.

References

[1] O. Parent, A. Ilinca, Anti-icing and de-icing techniques for wind turbines: Critical review, Cold Reg. Sci. Technol. 65 (2011) 88–96. https://doi.org/10.1016/j.coldregions.2010.01.005.

[2] S.K. Thomas, R.P. Cassoni, C.D. MacArthur, Aircraft anti-icing and de-icing techniques and modeling, J. Aircr. 33 (1996) 841–854. https://doi.org/10.2514/3.47027.

[3] F.T. Lynch, A. Khodadoust, Effects of ice accretions on aircraft aerodynamics, Prog. Aerosp. Sci. 37 (2001) 669–767. https://doi.org/10.1016/S0376-0421(01)00018-5.

[4] J.W. Melody, T. Başar, W.R. Perkins, P.G. Voulgaris, Parameter identification for inflight detection and characterization of aircraft icing, Control Eng. Pract. 8 (2000) 985–1001. https://doi.org/10.1016/S0967-0661(00)00046-0.

[5] L. Battisti, Optimising wind turbine design for operation in cold climates, in: Wind Energy Syst., Elsevier, 2011: pp. 388–460. https://doi.org/10.1533/9780857090638.3.388.

[6] W.J. Jasinski, S.C. Noe, M.S. Selig, M.B. Bragg, Wind Turbine Performance Under Icing Conditions, J. Sol. Energy Eng. 120 (1998) 60–65. https://doi.org/10.1115/1.2888048.

[7] Y. Cao, W. Tan, Z. Wu, Aircraft icing: An ongoing threat to aviation safety, Aerosp. Sci. Technol. 75 (2018) 353–385. https://doi.org/10.1016/j.ast.2017.12.028.

[8] F. Lamraoui, G. Fortin, R. Benoit, J. Perron, C. Masson, Atmospheric icing impact on wind turbine production, Cold Reg. Sci. Technol. 100 (2014) 36–49. https://doi.org/10.1016/j.coldregions.2013.12.008.

[9] J. Shin, B. Berkowitz, H.H. Chen, T. Cebeci, Prediction of ice shapes and their effect on airfoil drag, J. Aircr. 31 (1994) 263–270. https://doi.org/10.2514/3.46483.

[10] J. Shin, T.H. Bond, Experimental and computational ice shapes and resulting drag increase for a NACA 0012 airfoil, 5th Symp. Numer. Phys. Asp. Aerodyn. Flows. (1992).

[11] R.W. Gent, N.P. Dart, J.T. Cansdale, Aircraft icing, Philos. Trans. R. Soc. London. Ser. A Math. Phys. Eng. Sci. 358 (2000) 2873–2911. https://doi.org/10.1098/rsta.2000.0689.

[12] D. Anderson, A. Reich, Tests of the performance of coatings for low ice adhesion. In 35th Aerospace Sciences Meeting and Exhibit p-303, (1997).

[13] M. Mohseni, A. Amirfazli, A novel electro-thermal anti-icing system for fiber-reinforced polymer composite airfoils, Cold Reg. Sci. Technol. 87 (2013) 47–58. https://doi.org/10.1016/j.coldregions.2012.12.003.

[14] C. Antonini, M. Innocenti, T. Horn, M. Marengo, A. Amirfazli, Understanding the effect of superhydrophobic coatings on energy reduction in anti-icing systems, Cold Reg. Sci. Technol. 67 (2011) 58–67. https://doi.org/10.1016/j.coldregions.2011.02.006.

[15] S. Farhadi, M. Farzaneh, S.A. Kulinich, Anti-icing performance of superhydrophobic surfaces, Appl. Surf. Sci. 257 (2011) 6264–6269. https://doi.org/10.1016/j.apsusc.2011.02.057.

[16] A. Lazauskas, A. Guobienė, I. Prosyčevas, V. Baltrušaitis, V. Grigaliūnas, P. Narmontas, J. Baltrusaitis, Water droplet behavior on superhydrophobic SiO2 nanocomposite films during icing/deicing cycles, Mater. Charact. 82 (2013) 9–16. https://doi.org/10.1016/j.matchar.2013.04.017.

[17] D. De Pauw, A. Dolatabadi, Effect of Superhydrophobic Coating on the Anti-Icing and Deicing of an Airfoil, J. Aircr. 54 (2017) 490–499. https://doi.org/10.2514/1.C033828.

[18] H. Gomaa, M. Tembely, N. Esmail, A. Dolatabadi, Bouncing of cloud-sized microdroplets on superhydrophobic surfaces, Phys. Fluids. 32 (2020) 122118. https://doi.org/10.1063/5.0030188.

[19] V.F. Petrenko, C.R. Sullivan, V. Kozlyuk, F. V. Petsrenko, V. Veerasamy, Pulse electro-thermal de-icer (PETD), Cold Reg. Sci. Technol. 65 (2011) 70–78. https://doi.org/10.1016/j.coldregions.2010.06.002.

[20] H. Seifert, Technical Requirements for Rotor Blades Operating in Cold Climate, Proc. Boreas VI. (2003).

[21] R. Horbaty, Wind energy in cold climates – The swiss experience, Proc BOREAS VII, seventh ed., Levi, Finland, Mar 7–8, 2005,1–10.

[22] I. Baring-Gould, R. Cattin, M. Durstewitz, A. Krenn, T. Laakso, A. Lacroix, E. Peltola, G. Ronsten, L. Tallhaug, T. Wallenius, Recommendations for wind energy projects in cold climates, VTT Technical Research Centre, Finland, 2010.

[23] S. Brown, J. Lengaigne, N. Sharifi, M. Pugh, C. Moreau, A. Dolatabadi, L. Martinu, J.E. Klemberg-Sapieha, "Durability of Superhydrophobic Duplex Coating Systems for Aerospace Applications," *Surf. Coatings Technol.*, Vol. 401 (2020), p 126249. Doi:10.1016/j.surfcoat.2020.126249.

[24] H. Yan, H. Wu, Joule Heating and Chip Materials. In: Li D. (eds) Encyclopedia of Microfluidics and Nanofluidics. Springer, Boston, MA, (2014). https://doi.org/10.1007/978-3-642-27758-0_758-2

[25] N.J. Petersen, R.P.H. Nikolajsen, K.B. Mogensen, J.P. Kutter, Effect of Joule heating on efficiency and performance for microchip-based and capillary-based electrophoretic

separation systems: A closer look, Electrophoresis. 25 (2004) 253–269. https://doi.org/10.1002/elps.200305747.

[26] M. Prudenziati, Development and the Implementation of High-Temperature Reliable Heaters in Plasma Spray Technology, J. Therm. Spray Technol. 17 (2008) 234–243. https://doi.org/10.1007/s11666-008-9164-6.

[27] J.-M. Lamarre, P. Marcoux, M. Perrault, R.C. Abbott, J.-G. Legoux, Performance Analysis and Modeling of Thermally Sprayed Resistive Heaters, J. Therm. Spray Technol. 22 (2013) 947–953. https://doi.org/10.1007/s11666-013-9946-3.

[28] A. Lopera-Valle, A. McDonald, Application of Flame-Sprayed Coatings as Heating Elements for Polymer-Based Composite Structures, J. Therm. Spray Technol. 24 (2015) 1289–1301. https://doi.org/10.1007/s11666-015-0302-7.

[29] A. Lopera-Valle, A. McDonald, Flame-sprayed coatings as de-icing elements for fiber-reinforced polymer composite structures: Modeling and experimentation, Int. J. Heat Mass Transf. 97 (2016) 56–65. https://doi.org/10.1016/j.ijheatmasstransfer.2016.01.079.

[30] T.W. Clyne, Thermal and electrical conduction in MMCs, Comprehensive Composite Materials, third ed., Elsevier Science, (2000) 447–468.

[31] X. Qu, L. Zhang, M. Wu, S. Ren, Review of metal matrix composites with high thermal conductivity for thermal management applications, Prog. Nat. Sci. Mater. Int. 21 (2011) 189–197. https://doi.org/10.1016/S1002-0071(12)60029-X.

[32] J.M.M. Jordá, Metal matrix composites for thermal management: in Metal Matrix Composites: Materials, Manufacturing and Engineering, Walter de Gruyter GmbH & Co KG, 3 (2014).

[33] J.W. Kaczmar, K. Pietrzak, W. Włosiński, The production and application of metal matrix composite materials, J. Mater. Process. Technol. 106 (2000) 58–67. https://doi.org/10.1016/S0924-0136(00)00639-7.

[34] N.M. Melendez, A.G. McDonald, Development of WC-based metal matrix composite coatings using low-pressure cold gas dynamic spraying, Surf. Coatings Technol. 214 (2013) 101–109. https://doi.org/10.1016/j.surfcoat.2012.11.010.

[35] K.J. Hodder, J.A. Nychka, A.G. McDonald, Comparison of 10 μm and 20 nm Al-Al2O3 Metal Matrix Composite Coatings Fabricated by Low-Pressure Cold Gas Dynamic Spraying, J. Therm. Spray Technol. 23 (2014) 839–848. https://doi.org/10.1007/s11666-014-0094-1.

[36] N.M. Melendez, V.V. Narulkar, G.A. Fisher, A.G. McDonald, Effect of reinforcing particles on the wear rate of low-pressure cold-sprayed WC-based MMC coatings, Wear. 306 (2013) 185–195. https://doi.org/10.1016/j.wear.2013.08.006.

[37] G. Munday, J. Hogan, A. McDonald, On the microstructure-dependency of mechanical properties and failure of low-pressure cold-sprayed tungsten carbide-nickel metal matrix composite coatings, Surf. Coatings Technol. 396 (2020) 125947. https://doi.org/10.1016/j.surfcoat.2020.125947.

[38] Y.T.R. Lee, H. Ashrafizadeh, G. Fisher, A. McDonald, Effect of type of reinforcing particles on the deposition efficiency and wear resistance of low-pressure cold-sprayed metal matrix composite coatings, Surf. Coatings Technol. 324 (2017) 190–200. https://doi.org/10.1016/j.surfcoat.2017.05.057.

[39] D.W. Hahn, M.N. Özişik, Heat Conduction, John Wiley & Sons, Inc., Hoboken, NJ, USA, 2012. https://doi.org/10.1002/9781118411285.

[40] F. de Monte, Transient heat conduction in one-dimensional composite slab. A 'natural' analytic approach, Int. J. Heat Mass Transf. 43 (2000) 3607–3619. https://doi.org/10.1016/S0017-9310(00)00008-9.

[41] K.A. Antonopoulos, C. Tzivanidis, Analytical solution of boundary value problems of heat conduction in composite regions with arbitrary convection boundary conditions, Acta Mech. 118 (1996) 65–78. https://doi.org/10.1007/BF01410508.

[42] A. McDonald, C. Moreau, S. Chandra, Thermal contact resistance between plasma-sprayed particles and flat surfaces, Int. J. Heat Mass Transf. 50 (2007) 1737–1749. https://doi.org/10.1016/j.ijheatmasstransfer.2006.10.022.

[43] M. Prudenziati, "Development and the Implementation of High-Temperature Reliable Heaters in Plasma Spray Technology," J. Therm. Spray Technol., vol. 17, (2), pp. 234-243, 2008.

[44] M. Prudenziati and M. L. Gualtieri, "Electrical Properties of Thermally Sprayed Ni- and Ni20Cr-Based Resistors," J. Therm. Spray Technol., vol. 17, (3), pp. 385-394, 2008.

[45] An introduction to thermal spray, Oerlikon Metco, Issue 6, 2016.

[46] S.J. Penn, N.M. Alford, A. Templeton, X. Wang, M. Xu, M. Reece, K. Schrapel, Effect of Porosity and Grain Size on the Microwave Dielectric Properties of Sintered Alumina, J. Am. Ceram. Soc. 80 (2005) 1885–1888. https://doi.org/10.1111/j.1151-2916.1997.tb03066.x.

[47] D. Di Marco, K. Drissi, N. Delhote, O. Tantot, P.-M. Geffroy, S. Verdeyme, T. Chartier, Dielectric properties of pure alumina from 8 GHz to 73 GHz, J. Eur. Ceram. Soc. 36 (2016) 3355–3361. https://doi.org/10.1016/j.jeurceramsoc.2016.05.047.

[48] M. Rezvani Rad, M. Mohammadian Bajgiran, C. Moreau, A. McDonald, Fabrication of thermally sprayed coating systems for mitigation of ice accumulation in carbon steel pipes

and prevention of pipe bursting, Surf. Coatings Technol. 397 (2020) 126013. https://doi.org/10.1016/j.surfcoat.2020.126013.

[49] L. Pawłowski, The relationship between structure and dielectric properties in plasma-sprayed alumina coatings, Surf. Coatings Technol. 35 (1988) 285–298. https://doi.org/10.1016/0257-8972(88)90042-4.

[50] Rezvani-Rad, M., and McDonald, A., "Development of a Thermal-Sprayed Coating System to Mitigate Ice Accumulation and Freezing Damage in Carbon Steel Pipes," Thermal spray 2018: Proceedings of the International Thermal Spray Conference, Orlando, FL, USA, May 2018, pp. 1-8.

[51] H.M. Slot, E.R.M. Gelinck, C. Rentrop, E. van der Heide, "Leading Edge Erosion of Coated Wind Turbine Blades: Review of Coating Life Models," *Renew. Energy.*, Vol. 80 (2015), p 837–848. Doi:10.1016/j.renene.2015.02.036.

[52] R. Herring, K. Dyer, F. Martin, C. Ward, "The Increasing Importance of Leading Edge Erosion and a Review of Existing Protection Solutions," *Renew. Sustain. Energy Rev.*, Vol. 115 (2019), p 109382. Doi:10.1016/j.rser.2019.109382.

[53] M.H. Keegan, D.H. Nash, M.M. Stack, "On Erosion Issues Associated with the Leading Edge of Wind Turbine Blades," *J. Phys. D. Appl. Phys.*, Vol. 46, No. 38 (2013), p 383001. Doi:10.1088/0022-3727/46/38/383001.

[54] S. Zhang, K. Dam-Johansen, S. Nørkjær, P.L. Bernad, S. Kiil, "Erosion of Wind Turbine Blade Coatings – Design and Analysis of Jet-based Laboratory Equipment for Performance Evaluation," *Prog. Org. Coatings.*, Vol. 78 (2015), p 103–115. Doi:10.1016/j.porgcoat.2014.09.016.

[55] N. Dalili, A. Edrisy, R. Carriveau, "A Review of Surface Engineering Issues Critical to Wind Turbine Performance," *Renew. Sustain. Energy Rev.*, Vol. 13 (2009), p 428–438. Doi:10.1016/j.rser.2007.11.009

[56] P.H. Shipway, I.M. Hutchings, "Measurement of Coating Durability by Solid Particle Erosion," *Surf. Coatings Technol.*, Vol. 71 (1995), p 1–8. Doi:10.1016/0257-8972(94)02314-G.

[57] P. Kulu, I. Hussainova, R. Veinthal, "Solid Particle Erosion of Thermal Sprayed Coatings," *Wear.*, Vol. 258 (2005), p 488–496.

[58] H. Ashrafizadeh, P. Mertiny, A. McDonald, "Evaluation of the Effect of Temperature on Mechanical Properties and Wear Resistance of Polyurethane Elastomers," *Wear.*, Vol. 368–369 (2016), p 26–38. Doi:10.1016/j.wear.2016.08.008.

[59] ASTM G76, Standard Test Method for Conducting Erosion Tests by Solid Particle Impingement using Gas Jets, West Conshohocken, PA, USA, 2013.

[60] Heymann, F. J. "Liquid impingement erosion." *ASM handbook* 18 (1992): 221.

[61] Ahmad, M., M. Casey, and N. Sürken. "Experimental assessment of droplet impact erosion resistance of steam turbine blade materials." *Wear* 267, no. 9-10 (2009): 1605-1618.

[62] Mann, B. S., Vivek Arya, and Pankaj Joshi. "Advanced high-velocity oxygen-fuel coating and candidate materials for protecting LP steam turbine blades against droplet erosion." *Journal of materials engineering and performance* 14, no. 4 (2005): 487-494.

[63] Oka, Y. I., and H. Miyata. "Erosion behaviour of ceramic bulk and coating materials caused by water droplet impingement." *Wear* 267, no. 11 (2009): 1804-1810.

[64] Lima, M. M., C. Godoy, P. J. Modenesi, J. C. Avelar-Batista, A. Davison, and A. Matthews. "Coating fracture toughness determined by Vickers indentation: an important parameter in cavitation erosion resistance of WC–Co thermally sprayed coatings." *Surface and Coatings Technology* 177 (2004): 489-496.

[65] Shipway, P. H., and K. Gupta. "The potential of WC-Co hardmetals and HVOF sprayed coatings to combat water-droplet erosion." *Wear* 271, no. 9-10 (2011): 1418-1425.

[66] Springer, G. S. "Liquid droplet erosion." (1976).

[67] Mahdipoor, M. S., F. Tarasi, C. Moreau, A. Dolatabadi, and M. Medraj. "HVOF sprayed coatings of nano-agglomerated tungsten-carbide/cobalt powders for water droplet erosion application." *Wear* 330 (2015): 338-347.

[68] Gent, Roger W., Nicholas P. Dart, and James T. Cansdale. "Aircraft icing." *Philosophical Transactions of the Royal Society of London. Series A: Mathematical, Physical and Engineering Sciences* 358, no. 1776 (2000): 2873-2911.

[69] L.M. Jiji, Heat Conduction, Springer Berlin Heidelberg, Berlin, Heidelberg, 2009. https://doi.org/10.1007/978-3-642-01267-9.

[70] L.M. Jiji, Heat Convection, Springer Berlin Heidelberg, Berlin, Heidelberg, 2006. https://doi.org/10.1007/978-3-540-30694-8.

[71] A. Bejan, Convection Heat Transfer, John Wiley & Sons, Inc., Hoboken, NJ, USA, 2013. https://doi.org/10.1002/9781118671627.

[72] F.M. White, A New Integral Method for Analyzing the Turbulent Boundary Layer With Arbitrary Pressure Gradient, J. Basic Eng. 91 (1969) 371–376. https://doi.org/10.1115/1.3571122.

[73] J.R. Lloyd, W.R. Moran, Natural Convection Adjacent to Horizontal Surface of Various Planforms, J. Heat Transfer. 96 (1974) 443–447. https://doi.org/10.1115/1.3450224.

[74] A.A. Al-Aql, Electrical resistivity measurements in Ni–Cr alloys, Mater. Des. 24 (2003) 547–550. https://doi.org/10.1016/S0261-3069(03)00093-1.

[75] M. Mohammadian Bajgiran, M. Rezvani Rad, A. McDonald, C. Moreau, Microstructure, phase and dielectric strength of thermally sprayed alumina layers in coating-based heating systems, Int J Appl Ceram Technol. (2021). https://doi.org/10.1111/ijac.13731

[76] L. Zhou, S. Cui, Y. Zhai, F. Luo, Y. Dong, Dielectric and microwave absorption properties of plasma sprayed Cr/Al2O3 composite coatings, Ceram. Int. 41 (2015) 14908–14914. https://doi.org/10.1016/j.ceramint.2015.08.024.

[77] K. Bobzin, M. Öte, M.A. Knoch, I. Alkhasli, Temperature distribution on thermally sprayed heating conductor coatings, IOP Conf. Ser. Mater. Sci. Eng. 480 (2019) 012002. https://doi.org/10.1088/1757-899X/480/1/012002.

[78] H. Ashrafizadeh, A. McDonald, P. Mertiny, Deposition of Electrically Conductive Coatings on Castable Polyurethane Elastomers by the Flame Spraying Process, J. Therm. Spray Technol. 25 (2016) 419–430. https://doi.org/10.1007/s11666-015-0376-2.

[79] E. Enríquez, J.F. Fernández, J. De Frutos, M.A. De la Rubia, Tailoring of the electrical properties of carbon black–silica coatings for de-icing applications, Ceram. Int. 41 (2015) 2735–2743. https://doi.org/10.1016/j.ceramint.2014.10.088.

[80] K.N. Tu, Y. Liu, M. Li, Effect of Joule heating and current crowding on electromigration in mobile technology, Appl. Phys. Rev. 4 (2017) 011101. https://doi.org/10.1063/1.4974168.

[81] R.C. Progelhof, J.L. Throne, R.R. Ruetsch, Methods for predicting the thermal conductivity of composite systems: A review, Polym. Eng. Sci. 16 (1976) 615–625. https://doi.org/10.1002/pen.760160905.

[82] L. Bartolomé, J. Teuwen, "Prospective Challenges in the Experimentation of the Rain Erosion on the Leading Edge of Wind Turbine Blades," *Wind Energy.*, Vol. 22 (2019), p 140–151.

[83] H. Ashrafizadeh, *et al.*, "Deposition of Electrically Conductive Coatings on Castable Polyurethane Elastomers by the Flame Spraying Process," J. Therm. Spray Technol., Vol. 25, No. 3 (2016), pp. 419-430.

[84] D.W.C Baker, K.H. Jolliffe, D. Pearson, "The Resistance of Materials to Impact Erosion Damage," *Philosophical Transactions of the Royal Society of London. Series A, Mathematical and Physical Sciences*, Vol. 260, No. 1110 (1966), p 193–203.

[85] M. Elhadi Ibrahim, M. Medraj, "Water Droplet Erosion of Wind Turbine Blades: Mechanics, Testing, Modeling and Future Perspectives," *Materials.*, Vol. 13 (2019), p 157.

[86] J.H. Brunton, “High Speed Liquid Impact,” *Philosophical Transactions of the Royal Society of London. Series A, Mathematical and Physical Sciences*, Vol. 260, No. 1110 (1966), p 79–85.

[87] E.S. Gadelmawla, M.M. Koura, T.M.A. Maksoud, I.M. Elewa, H.H. Soliman, “Roughness Parameters,”, *J. Mater. Process. Technol.*, Vol. 123 (2002), p 133–145.

[88] A. McDonald, M. Lamontagne, S. Chandra, C. Moreau, “Photographing Impact of Plasma-Sprayed Particles on Metal Substrates,” *J. Therm. Spray Technol.*, Vol. 15 (2006), p 708–716. Doi:10.1361/105996306X147027.

[89] P.F. Chauvy, C. Madore, D. Landolt, “Variable Length Scale Analysis of Surface Topography: Characterization of Titanium Surfaces for Biomedical Applications,” *Surf. Coatings Technol.*, Vol. 110 (1998), p 48–56. Doi:10.1016/S0257-8972(98)00608-2.

[90] N. Tayebi, A.A. Polycarpou, “Modeling the Effect of Skewness and Kurtosis on the Static Friction Coefficient of Rough Surfaces,” *Tribol. Int.*, Vol. 37 (2004), p 491–505.

[91] A. V. Levy, W. Buqian, “Erosion of Hard Material Coating Systems,” *Wear.*, Vol. 121 (1988), p 325–346.

[92] Sharifi, Navid, Ali Dolatabadi, Martin Pugh, and Christian Moreau. "Anti-icing performance and durability of suspension plasma sprayed TiO2 coatings." *Cold Regions Science and Technology* 159 (2019): 1-12.

[93] Makkonen, L., 2012. Ice adhesion—theory, measurements and countermeasures. *Journal of Adhesion Science and Technology*, *26*(4-5), pp.413-445.